A MECHANISM FOR CURRENT SHEET THINNING IN THE GROWTH PHASE OF MAGNETOSPHERIC SUBSTORMS

A

THESIS

Presented to the Faculty
of the University of Alaska Fairbanks

in Partial Fulfillment of the Requirements
for the Degree of

DOCTOR OF PHILOSOPHY

By

Fred Hall IV, B.S., M.S.

Fairbanks, Alaska

May 2006

UMI Number: 3229735

Copyright 2006 by
Hall, Fred, IV

All rights reserved.

INFORMATION TO USERS

The quality of this reproduction is dependent upon the quality of the copy submitted. Broken or indistinct print, colored or poor quality illustrations and photographs, print bleed-through, substandard margins, and improper alignment can adversely affect reproduction.

In the unlikely event that the author did not send a complete manuscript and there are missing pages, these will be noted. Also, if unauthorized copyright material had to be removed, a note will indicate the deletion.

UMI®

UMI Microform 3229735
Copyright 2006 by ProQuest Information and Learning Company.
All rights reserved. This microform edition is protected against
unauthorized copying under Title 17, United States Code.

ProQuest Information and Learning Company
300 North Zeeb Road
P.O. Box 1346
Ann Arbor, MI 48106-1346

A MECHANISM FOR CURRENT SHEET THINNING IN THE GROWTH PHASE OF MAGNETOSPHERIC SUBSTORMS

By

Fred Hall IV

RECOMMENDED:

Advisory Committee Chair

John D Craven

Chair, Department of Physics

APPROVED:

Dean, College of Natural Science and Mathematics

Susan M. Henrichs

Dean of the Graduate School

April 17, 2006

Date

Abstract

The thinning of the near-Earth current sheet during the growth phase of magnetospheric substorms is a fundamental problem of space physics. It is a characteristic of the slow, steady evolution of the magnetosphere during the growth phase, during which the bulk kinetic energy of the solar wind is transformed into and stored as magnetic field energy in the magnetotail lobes. The thin near-Earth current sheet at the end of the growth phase provides the conditions for the onset of the expansion phase, and is fundamentally important to understand the physical mechanism for the onset of the rapid evolution during which the stored energy is released.

I propose that current sheet thinning occurs because of the evacuation of a 'magnetic flux reservoir' in the near-Earth magnetotail by convection to replace magnetic flux that is eroded on the dayside by magnetic reconnection. My hypothesis is able to predict basic properties of current sheet thinning, such as the location, temporal evolution, and dynamics of this process.

I examined this new mechanism both conceptually and quantitatively. My conceptual considerations enabled the prediction of the location and duration of current sheet thinning. This location is largely independent of the detailed state of the magnetosphere. I examined this mechanism quantitatively through the use of a three-dimensional ideal MHD simulation. I was able to predict the duration of the growth phase by considering the time needed to deplete our proposed 'magnetic flux reservoir.' The simulation demonstrates the global increase of the current density in this reservoir, despite the removal of magnetic flux—which one would otherwise expect to lead to a decrease of current—as well as even greater local amplifications of the current density. The simulation results are even more significant because the model does not include other effects of the real magnetosphere that contribute to a further increase of the tail current. The increase in current density and thinning are found to be consistent with the amount of flux removed from the system. In addition, I have found a new explanation for the very thin bifurcated current sheets that have been reported in recent publications.

Table of Contents

Signature Page i

Title Page ii

Abstract iii

Table of Contents iv

List of Figures vii

List of Tables x

List of Appendices xi

Acknowledgements xii

1 Introduction **1**

1.1 Fundamental Concepts 1

1.2 Basic Equations and Properties 4

1.3 Observed Current Sheet Properties 9

1.4 Review of Prior Work 11

1.5 Mechanism 13

1.6 Model Assumptions and Limitations 16

1.7 Scope of the Dissertation 16

2 Three-Dimensional Magnetic Field and Plasma Constraints for Adiabatic Convection **17**

2.1 Semi-Empirical Magnetic Field Models 17

2.2 The Tsyganenko-96 Semi-Empirical Magnetic Field Model 18

2.3 Pressure and Specific Entropy Model 19

2.4 Specific Entropy Model Output 22

2.4.1 Mapping from the Dayside Magnetopause to the Near-Earth Magnetotail Using the Specific Entropy 22

2.4.2 Contour Plots of the Flux Tube Volume per Unit Magnetic Flux, Pressure, and Specific Entropy in the Equatorial Plane 22

2.5 Parameter Study 27

2.5.1 Variation of the dynamic solar pressure $\mathbf{P}_{\mathbf{dyn}}$ 28

2.5.2 Variation of IMF $\mathbf{B}_{\mathbf{y}}$ 38

2.5.3 Variation of IMF $\mathbf{B}_{\mathbf{z}}$ 38

2.5.4 Variation of $\mathbf{D_{st}}$ 39

2.6 Calculation of the Ionospheric Energy Flux Resulting from Steady Convection of Magnetic Flux Tubes 40

2.6.1 Motivation 40

2.6.2 Results from Derivation 41

2.6.3 Results of Calculations 42

2.7 Discussion and Summary 47

3 3D MHD Model—Properties 49

3.1 Introduction 49

3.2 Governing Equations, Normalizations, and Grid 50

3.3 Numerical Solution of the Governing Equations 52

3.4 Boundary Conditions 56

3.4.1 Boundary Conditions Applicable to All Boundaries 57

3.4.2 The Equatorial Plane ($z = z_{min} = 0$) 58

3.4.3 The Earthward Boundary at $x = x_{max}$ 59

3.4.4 The Boundaries at $x = x_{min}$, $y = y_{min}$, $y = y_{max}$, and $z = z_{max}$ . . . 61

3.5 Relaxation of the Initial Configuration to an Equilibrium State 61

3.6 Description of the Initial Equilibrium State 66

3.7 Discussion and Summary 78

4 3D MHD Model—Outflow Boundary Condition and Results 81

4.1 Specification of the Outflow Boundary Condition 81

4.1.1 Specification of Azimuthal Velocity Profile in the Equatorial Plane . 81

4.1.2 Mapping of the Equatorial Velocity Profile to the Earthward Boundary 85

4.2 Evolution of the System under the Influence of the Outflow Boundary Condition 87

4.2.1 Outflow and Magnetic Flux Transport 87

4.2.2 Development of Current Density and Velocity Features 90

4.3 Estimate of Current Sheet Thinning Time Scale 99

4.4 Discussion and Summary 102

5 Summary and Conclusions 108

5.1 Proposed Model for Current Sheet Thinning During the Growth Phase of Magnetospheric Substorms 108

5.2 Three-Dimensional Magnetic Field and Plasma Constraints for Adiabatic Convection 108
5.3 3D MHD Model—Properties 109
5.4 3D MHD Model—Outflow Boundary Condition and Results 110
5.5 Discussion of Main Results 111
Bibliography **139**

List of Figures

1.1 Schematic view of the terrestrial magnetosphere 2
1.2 The Erickson-Wolf problem 7
1.3 The Harris sheet 8
1.4 Current sheet thinning mechanism 14

2.1 **B**, P, V, and S in the midnight meridian 23
2.2 Flux tube volume contour map 24
2.3 Thermal pressure contour map 25
2.4 Specific entropy contour map 26
2.5 Dependence of specific entropy on P_{dyn} 30
2.6 Dependence of B_z, V, P, and S on P_{dyn} 31
2.7 Dependence of specific entropy on IMF B_y 32
2.8 Dependence of B_z, V, P, and S on IMF B_y 33
2.9 Dependence of specific entropy on IMF B_z 34
2.10 Dependence of B_z, V, P, and S on IMF B_z 35
2.11 Dependence of specific entropy on D_{st} 36
2.12 Dependence of B_z, V, P, and S on D_{st} 37
2.13 Ionospheric energy flux as a function of downtail distance 44
2.14 Ionospheric energy flux as a function of latitude 45
2.15 Factors in the ionospheric flux 46

3.1 Domain of the simulation 51
3.2 Uniform grid in one spatial dimension and time 53
3.3 Leapfrog scheme in one spatial dimension 55
3.4 Physical and mathematical boundaries of the grid 57
3.5 Illustrations of symmetries and anti-symmetries across the equatorial plane 60
3.6 Force norm 65
3.7 Maximum velocity magnitude 66
3.8 Non-equilibrium magnetic field at the Earthward boundary 67
3.9 Equilibrium magnetic field at the Earthward boundary 67

3.10 Non-equilibrium magnetic field near the noon-midnight meridian 68
3.11 Equilibrium magnetic field near the noon-midnight meridian 68
3.12 Non-equilibrium density and pressure in the noon-midnight meridian 70
3.13 Equilibrium density and pressure in the noon-midnight meridian 71
3.14 Non-equilibrium current density in the noon-midnight meridian 72
3.15 Equilibrium current density in the noon-midnight meridian 72
3.16 Non-equilibrium current density at the Earthward boundary 73
3.17 Equilibrium current density at the Earthward boundary 73
3.18 Downtail current density 74
3.19 Equilibrium current density in the equatorial plane 74
3.20 Non-equilibrium field-aligned currents at the Earthward boundary 75
3.21 Equilibrium field-aligned currents at the Earthward boundary 75
3.22 Total acceleration at the beginning of the relaxation 77
3.23 Total acceleration at the end of the relaxation 77
3.24 Specific entropy at the end of the relaxation 79

4.1 Specification of the plasma outflow 83
4.2 Velocity profile immediately above the equatorial plane 88
4.3 Velocity profile at the Earthward boundary 89
4.4 Evolution of the magnetic field at the Earthward boundary 91
4.5 Evolution of the magnetic field in the equatorial plane 92
4.6 Magnetic flux reduction in the central equatorial plane 93
4.7 Evolution of the specific entropy in the equatorial plane 94
4.8 Current density and velocity in the vicinity of the noon-midnight meridian . 95
4.9 Current density and velocity away from the noon-midnight meridian 96
4.10 Current density along the noon-midnight meridian 98
4.11 Current density in the equatorial plane 100
4.12 Velocity in planes above the equatorial plane 101
4.13 Minimum v_z versus z 103
4.14 Magnetic field at the Earthward boundary for an especially long-running case 105

4.15 Velocity profile immediately above equatorial plane for an especially long-running case 106
4.16 Comparison of the current density in the noon-midnight meridian 107

B.1 Magnetotail flux tube 119

C.1 The frozen-in flux condition 124

E.1 Magnetic flux reservoir 135

List of Tables

2.1 Range of input parameters for T96 19

2.2 Input parameters for reference run 21

2.3 Input Parameters for the reference case used in the parameter study. IOPT is a program parameter with no physical significance that has been included here for the sake of completeness. Note that these values represent a relatively quiet magnetosphere. 29

2.4 Parameter values used in the parameter study 29

3.1 Normalized values of simulation quantities 52

3.2 Summary of boundary conditions on the velocity and magnetic field used in the simulation. Magnetic field components identified with the entry $\nabla \cdot \mathbf{b} = 0$ are determined through use of the divergence-free condition on the magnetic field on that boundary. Variables denoted by the designation "Symm." are symmetric across the boundary in question, whereas those denoted by the designation "Anti-symm." are anti-symmetric across the boundary in question. The entries "Special" pertain to the velocity boundary conditions at x_{max}. During the ballistic relaxation, $v_x = v_y = v_z = 0$. Once the initial equilibrium configuration has been established, these velocity components are specified in the manner discussed in Section 4.1. 62

3.3 Relaxation parameters for a sample 'equilibrium run.' The time step during this run was $\Delta t = 0.01\ t_A$. Ballistic relaxation was discontinued at $t = 120\ t_A$. 64

4.1 Typical Outflow Parameters 82

List of Appendices

A Local Conservation of Entropy **113**

- A.1 Derivation utilizing the first law of thermodynamics and the ideal gas law . 113
- A.2 Derivation utilizing the continuity equation and the pressure equation . . . 115

B The differential magnetic flux tube volume **118**

C Derivation of the time rate of change of the particle number N on a magnetic flux tube **121**

D Derivation of the ionospheric energy flux **130**

E Estimate of the time required to deplete the "magnetic flux reservoir" **134**

Acknowledgements

I find it incredible that, finally, I have reached this point. Words cannot convey the sense of appreciation and relief that I am feeling at this point. At times in the past I had feared that I would never find myself doing just this ... writing the Acknowledgments of my dissertation. At other times, I thought that I would indeed find myself attending to this task ... but only much later, at another institution. Yet here I am. I am quite glad that I have finally reached this point in my journey. But I have been quite fortunate in that I have not traveled this path alone. Indeed, I would like to thank all of the people who have helped me through the years as I made my way along the path.

I would like to begin by thanking my parents. I could probably write tomes in appreciation of all that they have done for me; but time does not allow me such a treatment. For now, I will have to be content with noting the following. Mom and Dad have done so much for me even since before my birth. Although I truly can say that I was born a poor Black child (in a more valid sense than Steve Martin's character in "The Jerk,"), I do not remember ever being truly poor. My parents worked hard to ensure that my sister and I enjoyed a comfortable middle-class upbringing. My parents' story is the sort of classic American story that seems more difficult to find these days. I must thank my parents for believing in me and standing up for me, especially for those times when I either did not believe or stand up for myself. I thank my parents for trusting in me enough to let me find my own path, even when they had doubts themselves. They know, from long experience, that I am stubborn in my own quiet way. Thank you, Mom and Dad. I love you.

I would also like to thank my sister Rose, who has been a friend and confidante for most of our lives. Even though I am the elder sibling, Rose has more often been the one who has looked out for me. I hope that I can reciprocate more in the future. Mind you, Rose does not need me to look after her; she certainly does a much better job of looking after herself and her family than I do of looking after just myself. But I hope that I can do more for Rose and her family in the future than I have been able to do during these many years that I have been a student (most of my life at this point, as my father recently pointed out). In any case, I would like to thank Rose for being such a great sister ... despite having such an eccentric brother. I love you, too.

Speaking of my sister's family ... I am looking forward to the opportunity to know them

better. I have kept in touch with my family while I have been away at school, and I have visited from time to time. But that does not quite substitute for being there and seeing everybody. I already know just how great a fellow Juano is; after all, Rose would not have married him otherwise. Still, I enjoy our conversations so much that it will be good to hang out with him some more. I am looking forward to seeing Déja, Matéya, and Torré grow up into the lovely young ladies whom they will become. And I look forward to becoming better acquainted with the young men into whom Jerrell, Jeremy, and Keith have grown.

I must take a moment to thank the members of my extended family, who have supported me throughout the years. It has been quite some time since I have seen so many of you. I am looking forward to seeing you all again. Unfortunately, I cannot take the time now to thank you all individually as you deserve; but I look forward to thanking you in person when time allows. I would like to mention a few special individuals. Aunt Dot ... you have always been there, and I just want to thank you for being great. Thanks for all of those wonderful holiday meals, too! I would like to extend my thanks and love to my entire extended family.

Now I would like to thank another class of individuals: my teachers and professors. I know that education is an inherent part of your job descriptions; nevertheless, I believe that it is quite appropriate for me to thank you for teaching me so much.

I would like to begin this section by thanking Antonius Otto, my dissertation advisor, for remaining my advisor for all of these years. I am sure that he has sometimes questioned the wisdom of that course of action. I have learned so very much about magnetospheric physics and numerical simulation in my time under his wing. At least as much as anything else, I must thank you, Antonius, for your patience. I would also like to thank Isabelle Tissier, Antonius's wife, for her kindness and hospitality since the very beginning of my stay in Fairbanks.

I would also like to thank Antonius's predecessors: Ellen Gould Zweibel, my advisor during my graduate career at the University of Colorado at Boulder and David S. Onley, my undergraduate advisor at Ohio University. I thank you two for getting me started on this path. I thank you for continuing to provide me with support and advice long after your 'official' tenures as my advisor ended. And I thank you for your friendship.

I next give thanks to the remaining members of my Advisory Committee: Heinz Wiechen, Dirk Lummerzheim, Dave Sentman, Hans Nielsen, and Brenton Watkins. Thanks for sticking with me all of this time. It has been a long haul, hasn't it? Sometimes I joke that these guys were eager to sign my dissertation because they knew that it was the only way that I would finally leave them alone. But more seriously, I have learned much from these fellows ... not just in working with them directly on my research, but in seeing how they conduct themselves. I suppose that would make them role models, wouldn't it? I would also like to thank Dan Swift for his earlier service as a member of my Advisory Committee.

Of course, I can say much of the same of many of the faculty members of the three departments of which I have been a member. Although there are many who deserve honor, I single out the following (in addition to the professors already mentioned) for special recognition.

- Ohio University: Sergio Ulloa and Louis E. Wright
- University of Colorado at Boulder: Fran Bagenal, Scott Robertson, and Ted Speiser
- University of Alaska Fairbanks: Scott Bailey (and his 'significant other,' Doobie Soo), Curt Szuberla (and his wife Alice), David Newman (and his wife Uma Bhatt), and John Craven

I hope that there are none who feel too slighted. Again, longer contemplation would probably make these lists grow longer.

Of course, academic departments would grind to a halt were it not for the work of their staff. It is well known that the true power of a department lies with its staff. It is unwise for students to draw the ire of their professors. But I pity the foolish student who offends the administrative secretary or administrative assistant in the department. I would be remiss were I not to thank Barbara Day and Mary Parsons, who rule benevolently in the Department of Physics at the University of Alaska Fairbanks. I would also like to thank their predecessors, Norma Pfeiffer (as well as her husband Ian, who is a cool fellow) and Irene Downes (and her family). I would also like to acknowledge the work of John Peterson and Robert Parsons, who have tended to the labs and are interesting fellows as well. I thank another Barbara from what was the Department of Astrophysical, Planetary, and Atmospheric Sciences at the University of Colorado at Boulder, as well as Candy and the Bakers from the Department of Physics and Astronomy at Ohio University.

Even though I last graced their classes in what seems a lifetime ago, I should not forget my teachers from the years before college either. In particular, I would like to thank Mrs. Chris Allen for her teaching of chemistry and physics. I also thank Mr. Napier for ensuring that I behaved properly, and for his continued friendship.

It is said that one's friends are the family that one chooses. In that sense, I have a large family of friends. I lack the time to give them all their proper due. But I would like to pay tribute to several of my closer friends.

I will begin with those who have been so kind to me during my time here in Fairbanks. I extend special thanks to the following friends:

- Chris Whittle, who has been a close friend during much of my time here;
- Karen Remick, from whose whose keen insights into organization, practical ways of getting things done, and human nature I have greatly benefited during our friendship;
- Fernanda de São Sabbas Tavares, my great Brazilian friend whose diminutive stature belies her strength of character;
- Katariina Nykyri, my extraordinarily dynamic Finnish friend who can tire out people who just think of all she does, and her husband Mikko (who is quite impressive in his own right);
- Ken Arnoult, a truly kind fellow who was quite helpful in especially trying times during my graduate career and who is often game for a good conversation or movie, as well as his lovely wife Katrin Iken;
- Justin Yonker and Saphia Yonker, a delightful couple who are intriguing and interesting characters both singly and together, and who also helped me greatly during dark days of my graduate career;
- Laura Peticolas, a truly delightful, fun, kind, and intelligent lady who has been so very encouraging throughout the years and her personal Beastie Boy, her husband Tom Immel—a cool guy in his own right;

- Ryan Woodard, an incredibly funny guy whose sense of humor sometimes makes one forget the depth of his intelligence, and his delightfully British wife Hilary Fletcher, who is just an all-around fun and bonny lass;
- Matt Heavner, my oh-so Linux-savvy friend and his oh-so cute wife Carrie;
- Vincent Dols, the intelligent Belgian cartoonist physicist and his wife Cécile Hannay;
- Dave Covey, the local Unix/Linux demi-god, who is kind enough not to require the usual sacrifice of a Windows user when a request is made of him;
- Dana Moudra-Truffer, Martin Truffer, Peter Delamere, Jen Delamere, Veronika Besser, Matt Krynicki, and other former graduate students around both here in Fairbanks and in Boulder, as well as all current physics graduate students not already mentioned; and
- Dorothy Jones and her successor Earlina Bowden, two strong and impressive ladies who have offered me kind words and encouragement (and occasionally threats) to move me along in my graduate career here.

I would also like to mention friends from my days in Boulder. Deserving special mention are the following friends:

- Sarah Gibson and Mark Miesch, who are impressive and kind both singly and together as a married couple;
- Linda Sauter, who is simultaneously cool and spicy, not to mention simply intriguing;
- Niescja Turner, also known as Young mc^2, with whom I have continued to stay in contact through our involvement in the Geospace Environment Modeling (GEM) community—and who has a really neat name;
- Geoff Clayton, who is a generally smart, kind, and neat fellow; and
- David Theil, Kara Peterson, Travis Rector, Margaret H. Hanson, and Chris Boozer—good people all.

Of course, I cannot forget my Ohio University (OU) Posse, who taught me one of the great lessons in life: it is good to be a geek. Foremost among these good people is Morag K. Smith, who is amazingly humble for such a truly impressive lady. Bill Jameson is one of the neatest people whom I believe I have met; he is incredibly intelligent as well. Grett Etter is another blazingly smart fellow; I don't believe that I have known anybody who thinks quite so much like a computer. I would be remiss were I not to mention Julie Wiebell, who somehow manages to fit so very much into life; John Waldron, who has grown so much (as a person, not in physical size) since our undergraduate days; and Mark O'Connor, who razor-sharp wit is balanced by his good nature. Outside of my geeky Posse, I would like to mention Brenda Bhatti, who is as delightful a lady now as she was then—and, it seems, somehow even busier.

There are so many others whom I should mention, including

- my present officemates—Eric Adamson (and his lovely wife Casey), John Styers, and Sam Lazerson—as well as earlier officemates (not already mentioned) such as Hua Zhu and Lin Zhang;
- Graduate Dean Susan Henrichs and Laura Bender of the Graduate School, for providing support—both financial and emotional—that made the completion of my graduate program possible, as well as their co-workers Lillian Misel and Juan Goula and their predecessors—former Graduate Dean Joe Kan, Faith, and Crystal;
- the National Aeronautics and Space Administration (NASA) for providing financial support (through my advisor's grants) and, perhaps even more importantly, for providing inspiration since my youth;
- the National Physical Science Consortium (NPSC) and NASA Marshall Space Flight Center, which provided financial support earlier in my graduate career;
- the Alaska Space Grant Program, which provided me with financial support at times during my graduate studies here in Fairbanks;
- the many members of the Geophysical Institute/International Arctic Research Center family who have been so very supportive throughout the years, including Sue

Cave, Deborah Coccia Manning, Penelope Noecker, Dolores Baker, Robin Ural, Judie Triplehorn, Ray Ward, Brian Lu, Jan Dalrymple, Joanna Cruzan, Roger Smith, Jackie Dashiell, Roberta Greenlee, Celia Rohwer, and Jesse Atencio;

- the members of the Dateless Geeks Movie Group, including Debi-Lee Wilkinson, Helena Byard, Suzie Campbell, Ruth Freeburg, Cynthia Weatherby, and Melinda Harris;
- other friends of mine in the University of Alaska Fairbanks community, such as John Gimbel, Rebecca Bullman, Joe Hayes, Jackie Alleyne-McCants, Lynette Washington, Ana Richards, Debra Pearson, Qwynten Richards, and Don Foley;
- friends of mine in the Fairbanks community such as Tonya Brown;
- my friends in the aforementioned GEM community, including Jerry Goldstein (otherwise known as my homie Easy-G), Michelle (Chelle) Reno, Vahe Peroomian, Janet Green, Colby Lemon, and Umbe Cantu;
- my friends in the National Society of Black Physicists (NSBP), including Charles McGruder III (who first brought the organization to my attention), Beth A. Brown, Marta Dark McNeese, and Jarita C. Holbrook;
- Research Experience for Undergraduates (REU) and other Summer interns here at the Geophysical Institute throughout the years, including Rachael Shoulder, Brandon Marken, Jason McDonald, Richard J. Stevens, Theresa Turner, and Halle Morrison;
- Kool Moe Dee, Digital Underground, Ice Cube, and a variety of other rappers and hip-hop artists and groups, as well as 'Weird Al' Yankovic and the wonderful Earth, Wind, and Fire;
- Carl Sagan and Isaac Asimov for serving as inspirations and role models;
- Gene Roddenberry and all those involved in bringing Star Trek to life in all its generations and incarnations;
- J. Michael Straczynski and all those involved in bringing *Babylon 5* into existence and keeping it alive throughout its five-year run, despite the odds;

- George Lucas and all those involved in populating the Star Wars universe;
- Joss Whedon and the casts and crews of *Firefly* and *Serenity*; and
- *Analog Science Fiction and Fact*, its contributors, and other creators and suppliers of excellent science fiction.

Unfortunately, the time that I can devote to these acknowledgments is rather limited. I apologize to those deserving of recognition but who are not mentioned here. Your contributions to my success are still greatly appreciated. To all of you ... thanks.

Chapter 1
Introduction

1.1 Fundamental Concepts

This dissertation describes a model for current sheet thinning in the late growth phase of magnetospheric substorms. The development of this model is motivated by questions surrounding the identity and nature of the trigger of the substorm expansion phase. In order to allow for greater appreciation of the nature of these questions, it behooves me to first review some basic properties of the magnetosphere and its dynamics.

The terrestrial magnetosphere is a fascinating, and reasonably accessible, natural laboratory for a variety of plasma physics processes. It is formed through the interaction of Earth's intrinsic dipolar magnetic field and the interplanetary magnetic field (IMF) that is embedded in the solar wind, a stream of plasma flowing outward from the Sun. This interaction compresses Earth's magnetic field on the sunward side and draws it out into a long tail in the anti-sunward direction.

The terrestrial magnetosphere is depicted schematically in Figure 1.1. The magnetopause is a current layer that serves as the outer boundary of the magnetosphere proper; the plasmas and current systems of the magnetosphere lie within the volume defined by this boundary. The near-Earth portions of the magnetosphere, such as the plasmasphere, are dominated by Earth's largely dipolar magnetic field. The volume of the magnetosphere is dominated by the magnetotail, the roughly cylindrical low-density region stretching anti-sunward for hundreds of Earth radii. [Earth's radius (6378 km) is a convenient unit of length in terrestrial magnetospheric physics. It is denoted by the symbol R_E.] The magnetotail is divided into two lobes (north and south) with oppositely directed magnetic fields (sunward in the northern lobe, anti-sunward in the southern lobe). A current sheet, consisting of westward-directed current lying in the equatorial plane of the magnetotail, separates the oppositely directed magnetic fields in the two lobes. The charge carriers that maintain this current sheet are supplied by the plasma sheet, within which the current sheet is embedded.

Field-aligned currents link portions of the magnetosphere with the auroral ovals, the annular regions of the atmosphere surrounding the magnetic poles in which the aurora are observed. These field-aligned currents communicate changes in the state of the magnetosphere to the auroral ionosphere. Similarly, changes in the auroral ionosphere are

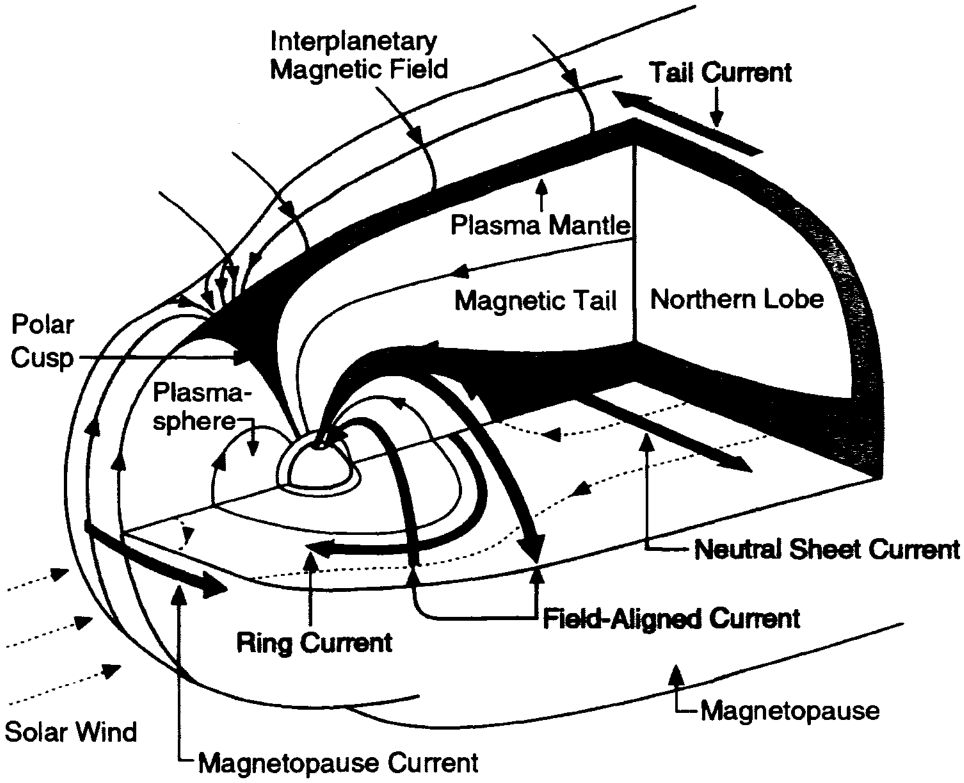
Interplanetary Magnetic Field
Tail Current
Plasma Mantle
Magnetic Tail
Northern Lobe
Polar Cusp
Plasma-sphere
Neutral Sheet Current
Field-Aligned Current
Ring Current
Magnetopause
Solar Wind
Magnetopause Current

Figure 1.1. Schematic view of the terrestrial magnetosphere. A cut-away 3D view of the magnetosphere. [*Crooker et al.*, 1999].

communicated to the remainder of the magnetosphere through these field-aligned currents.

Various authors (e.g., *McPherron* [1972], *Baker and Pulkkinen* [1991]) note the importance of the near-Earth magnetotail (extending from roughly 6 R_E to $\sim$ 15 R_E downtail) for both magnetospheric structure and dynamics. It is in this region that the magnetic field makes a transition from the largely dipolar configuration of the inner magnetosphere to the geometry of the magnetotail. This near-Earth region of the magnetotail is also the location for some of the important features of magnetospheric dynamics which will be a focus of this dissertation.

Earth's magnetosphere is continuously interacting with the solar wind, exchanging mass, momentum, and energy therewith. The resulting dynamics are extraordinarily complex; but researchers have learned much through the years (especially since the advent of the Space Age). Of particular interest for this work is the identification of a sequence of changes in the auroral ionosphere and the magnetosphere known as a magnetospheric substorm.

The magnetospheric substorm can be considered a fundamental process of magnetospheric dynamics. It consists of three phases: growth, expansion, and recovery. A 'classical' substorm begins with the southward turning of the IMF. A portion of the bulk kinetic energy of the solar wind incident on the magnetosphere is transformed into magnetic field energy through the process of magnetic reconnection at the dayside magnetopause. This energy is stored as enhanced magnetic field energy in the magnetotail lobes until this storage is disrupted with the onset of the expansion phase.

The accumulated energy stored during the growth phase is released in an explosive fashion during the expansion phase of the substorm. Some of this energy is dissipated through the auroral ionosphere, while some of it is expelled down the magnetotail (in the anti-sunward direction) in a plasmoid, a bubble of plasma with magnetic field lines detached from Earth. The configuration of the magnetosphere returns to its 'ground state' during the recovery phase of the substorm. The growth and expansion phases each last 30 to 60 minutes, while the recovery phase occurs over a period of one to two hours.

The process or processes responsible for the transition from the growth phase to the onset of the expansion phase are of great interest because they lead to the release of the energy that had been stored in the magnetosphere during the growth phase. The nature of these processes might also help to explain some of the dramatic differences between the growth and expansion phases. The magnetosphere evolves relatively slowly during the growth phase, especially when compared to its evolution during the expansion phase.

The evolution of the magnetosphere during the growth phase has been modeled as being slow, as outlined below. These characteristics render the growth phase suitable for study through the use of magnetohydrodynamics (MHD), a single-fluid description of a plasma. *Lee et al.* [1995] argue that the time scale of the growth phase is appreciably longer than the fast-mode transit time across the magnetosphere.

For this reason, the thinning of the current sheet observed in the near-Earth magnetotail during the late growth phase is of particular interest. This phenomenon has been observed from $\sim 9\,R_E$ to $\sim 15\,R_E$ downtail [e.g., *Sergeev et al.* [1988], *Sergeev et al.* [1990]]. Further insight into the nature of this central aspect of growth phase dynamics represents a major advance in our understanding of substorm dynamics. This dissertation attempts to shed light on this important question employing constraints, in particular mass and entropy conservation for magnetospheric convection.

1.2 Basic Equations and Properties

In order to more fully appreciate the arguments that follow, it will serve us well to consider the MHD equations (i.e., *Baumjohann and Treumann* [1997], *Kivelson and Russell* [1995]): the mass continuity equation,

$$\frac{\partial \rho}{\partial t} = -\nabla \cdot (\rho \mathbf{v}); \tag{1.1}$$

the momentum equation,

$$\frac{\partial (\rho \mathbf{v})}{\partial t} = -\nabla \cdot (\rho \mathbf{v}\mathbf{v}) - \nabla P + \mathbf{J} \times \mathbf{B}; \tag{1.2}$$

Faraday's law,

$$\frac{\partial \mathbf{B}}{\partial t} = \nabla \times (\mathbf{v} \times \mathbf{B} - \eta \mathbf{J}); \tag{1.3}$$

the pressure equation,

$$\frac{\partial P}{\partial t} = -\nabla \cdot (P\mathbf{v}) + (\gamma - 1)\left[\eta J^2 - P(\nabla \cdot \mathbf{v})\right]; \tag{1.4}$$

and Ampère's law,

$$\mathbf{J} = \left(\frac{1}{\mu_0}\right)(\nabla \times \mathbf{B}). \tag{1.5}$$

The variables ρ, P, $\mathbf{v}$, $\mathbf{B}$, $\mathbf{J}$, and η represent the mass density, thermal pressure, plasma velocity, magnetic field, current density, and resistivity, respectively. The permeability of free space is μ_0. The ratio of specific heats γ, sometimes called the adiabatic or polytropic index, is chosen to be $\frac{5}{3}$ (appropriate for an isotropic plasma with three degrees of freedom). In this study, I will use ideal MHD, in which the resistivity η is set identically equal to zero. This condition is satisfied almost everywhere in the highly collisionless magnetospheric plasma.

Equation 1.3 is obtained by combining the induction equation and resistive Ohm's law. Equation 1.5 is Ampère's law with the displacement current neglected. This neglect is justified if velocities and phase velocities are much smaller than the speed of light (c).

Let us now consider the concept of entropy. Combining the energy equation (Equation 1.4) (with $\eta = 0$) with the continuity equation (Equation 1.1), I obtain an equation for the entropy $s = \frac{P}{\rho^\gamma}$ (discussed further in Appendix A):

$$\frac{ds}{dt} = \frac{\partial s}{\partial t} + \mathbf{v} \cdot \nabla s = 0, \tag{1.6}$$

which implies that s is a constant during convection:

$$s = \frac{P}{n^\gamma} = s_0. \tag{1.7}$$

It would be nice to generalize this statement of the local conservation of specific entropy so that the conservation of this quantity can be applied more globally. Invoking a magnetostatic equilibrium—in which time derivatives and velocity are both zero—I find that Equation 1.2 implies

$$\mathbf{B} \cdot \nabla P = 0, \tag{1.8}$$

or in words, the pressure is constant along magnetic field lines. If I invoke the frozen-field condition of ideal MHD, I see that the different plasma parcels along a particular field line have the same pressure. Furthermore, in ideal MHD these plasma parcels will remain connected to the same magnetic field line.

Through evaluation of the quantity

$$H = \int_{\ell_1}^{\ell_2} d\ell \iint_{A_c} P^{\frac{1}{\gamma}} \, dA \tag{1.9}$$

(discussed further in Equation D.4 of Appendix D) and using the definition

$$V = \int_{\ell_1}^{\ell_2} \left(\frac{1}{B}\right) d\ell \tag{1.10}$$

(discussed further in Appendix B) for the differential magnetic flux tube volume (also called the magnetic flux tube volume per unit magnetic flux), one can define the specific entropy

$$S = PV^{\gamma} \tag{1.11}$$

for any magnetic flux tube. The specific entropy is also conserved for adiabatic convection:

$$\frac{dS}{dt} = 0. \tag{1.12}$$

I will use the equatorial plane as a reference plane and determine the distribution of the specific entropy of magnetic flux tubes crossing this plane. This provides maps for the specific entropy distribution in the equatorial plane which will be used for discussion of magnetotail convection in Chapter 2.

Let us consider the prospects of utilizing this specific entropy as a conserved quantity. It is closely related to the thermal energy of the plasma in the magnetic flux tube under consideration. One may envision this flux tube as an isolated system—somewhat akin to a long, skinny balloon (with cross-sectional area $\sim \frac{1}{B}$). As this flux tube moves within the magnetosphere, its volume (per unit magnetic flux) must change as the flux tube moves into regions with different magnetic fields. (Refer to Figure 1.2.) If the specific entropy of that magnetic flux tube is conserved, then its pressure must change as its differential volume changes. In an analogous manner, the pressure inside a closed balloon must change if that balloon is squeezed or stretched. If the distribution of specific entropy in the equatorial plane is known, then this distribution allows us to determine the path along which a particular flux tube (with a certain value of the specific entropy) is constrained to convect. We can

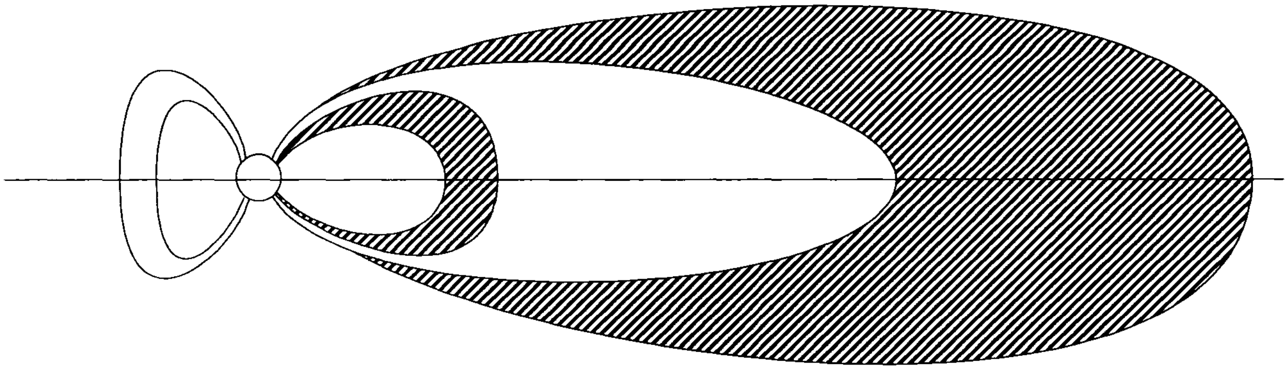

Figure 1.2. The Erickson-Wolf problem

generalize the motion of this particular flux tube to the motion of ensembles of flux tubes in Earth's magnetotail. Since the frozen-flux condition is assumed to hold in this analysis, we can trace the motion of these magnetic flux tubes by the motion of the plasma contained within them. Specifically, the concept of entropy conservation implies that steady-state convection ($\frac{\partial}{\partial t} = 0$) is only possible along contours of constant entropy. Vice versa, any convection with a velocity component perpendicular to an iso-entropy contour implies time dependence.

Before discussing observations of current sheets, I will consider a simple model that will help us to place the later discussions in context. There is an exact one-dimensional solution for a current sheet. This is so-called Harris sheet model (*Harris* [1965]). For this model, the magnetic field, current density, and pressure are given by

$$B_x = B_0 \tanh\left(\frac{z}{L}\right) \tag{1.13}$$

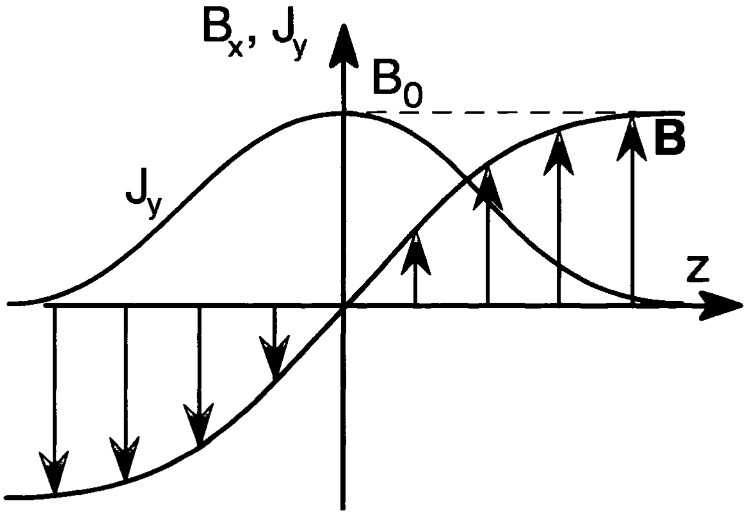

Figure 1.3. The Harris sheet. Profiles of the magnetic field (Equation 1.13) and the current density (Equation 1.14) as functions of z.

$$J_y = \left(\frac{B_0}{\mu_0 L}\right) sech^2\left(\frac{z}{L}\right) \tag{1.14}$$

$$P = \left(\frac{B_0^2}{2\mu_0}\right) sech^2\left(\frac{z}{L}\right), \tag{1.15}$$

where L is the characteristic length which I identify as the half-thickness of the current sheet. Here the magnetic field is zero in its central plane ($z = 0$), and reverses sign across this plane. It is for these reasons that the current sheet is sometimes called the neutral sheet. I remark that magnetic pressure is balanced by the thermal pressure. The magnetic field (Equation 1.13) and current density (Equation 1.14) are depicted in Figure 1.3.

While the one-dimensional Harris solution is somewhat idealized, more realistic two-dimensional current sheet models are based on it. Finally, it is worth noting that the observed current sheet thinning in the tail cannot be achieved by a simple compression of the current sheet. Even an increase of the lobe field by an unrealistic factor of 2 can only reduce the current sheet width to about half of its original value, whereas observations indicate a reduction in width by more than a factor of 10 (Section 1.3).

1.3 Observed Current Sheet Properties

The importance of the current sheet in substorm dynamics is matched by the challenges involved in the determination of some of its most important properties—in particular, its position, thickness, and structure. Many spacecraft have flown through the magnetotail current sheet since its discovery (*Ness* [1965]). However, the determination of current sheet properties is fraught with difficulties, including the ambiguity of spatial and temporal variations in the observations.

It can be quite difficult to distinguish the spatial variations in the current sheet due to its structure and the temporal variations of its properties with only one spacecraft. Not only that, but using only a single spacecraft one cannot determine, at a given time, the spatial gradients in the magnetic field that would allow the calculation of the current density.

Coordinated multi-spacecraft observations are far superior to single-spacecraft observations for the determination of current sheet properties. Coordinated multi-spacecraft measurements allow the calculation of spatial gradients in the magnetic field that are used in the computation of the current density. The joint ISEE-1 and ISEE-2 spacecraft missions in 1978 and 1979 allowed investigators many more opportunities (than the rare coincidental positioning of two or more satellites) to determine current sheet properties. Examples of such studies include *McComas et al.* [1986], *McPherron et al.* [1987], *Sanny et al.* [1994], and *Zhou et al.* [1997]. *McComas et al.* [1986] analyzed three crossings of the current sheet at $\sim 18\,R_E$. They found that a typical quiet current sheet is several ion gyroradii (ρ_i) thick, with typical values of $\rho_i \sim 3000$ km for a 5-keV ion in a 2-nT magnetic field (as described in *Thompson et al.* [2005]). Both *McPherron et al.* [1987] and *Sanny et al.* [1994] examined a current sheet crossing of ISEE-1 and 2 at a downtail distance of $\sim 13\,R_E$. *Sanny et al.* [1994] found an average thickness of $\sim 5\,R_E$ one hour before substorm onset. The current sheet thickness consequently decreased to less than $1\,R_E$ before onset. *McPherron et al.* [1987] obtained comparable results. *Sergeev et al.* [1990] used dual-spacecraft observations (GEOS-2 and ISEE-1 in one case, GEOS-2 and IMP-J in another), in conjunction with ground-based observations, to study the evolution of the current sheet during the growth phase. They determined the half-thickness of $\sim 0.1\,R_E$ at $\sim 9\,R_E$, suggesting that "the flattened current sheet at $r \approx 10\,R_E$ is embedded within a broad (a few R_E) plasma sheet. [*Sergeev et al.*, 1993, p. 3827] used observations of the ISEE-1 and 2 spacecraft at $\sim 11\,R_E$

to study the evolution of the current sheet during the growth phase and early expansion phase of a substorm. They found clear evidence of a very thin current sheet, with a half-thickness of $\sim 0.1\,R_E$, in the near-Earth magnetotail at $\sim 11\,R_E$ at the end of the growth phase. This thickness is "comparable to the gyroradius of a thermal proton outside this [very thin current] structure" [*Sergeev et al.*, 1993, P. 17363]. These authors found that the current density increased by a factor of 5 to 10 "with respect to its typical value in that region" [*Sergeev et al.*, 1993, P. 17363]. They also found that the small (approximately 1 nT) normal component of the magnetic field was dominated by a large shear (B_y) magnetic field component during the late growth phase. accounting for most of the total magnitude of the magnetic field **B** at that point. These authors also note that nature and characteristic scales (both spatial and temporal) of the changes in the plasma sheet and the magnetic configuration are different during the growth and expansion phases. During the growth phase, the current sheet structure has a global character (akin to, though not as simple as, the Harris sheet). During the expansion phase, localized current structures can be found. The later study of *Zhou et al.* [1997] found a minimum thickness of $\sim 0.5\,R_E$ for a case study substorm onset.

More recently, spacecraft constellations such as the four-spacecraft Cluster fleet have enabled the determination of spatial gradients of the magnetic field in all three spatial directions with greatly improved accuracy. *Thompson et al.* [2005] utilized observations from these spacecraft to determine the current sheet thickness using a "dynamic" (that is, time-varying) Harris sheet model. They found minimum current sheet thickness of $\sim$ 1000 km for three substorm events using data obtained when the Cluster constellation was at 17.3 and 18.7 R_E downtail. These authors also noted that "bifurcation" of the current sheet (defined as the splitting of the current sheet into "two distinct sheets of current separated by a weaker current region" [*Thompson et al.*, 2005, P. 2 of 26]) has been suggested by several studies, including those of *Nakamura et al.* [2002], *Runov et al.* [2003], and *Sergeev et al.* [2003].

I will find it useful to summarize the observations that I will find most relevant for my future considerations.

- Thin current sheets have been observed at distances from $\sim 9\,R_E$ (*Sergeev et al.* [1990]) to $\sim 18.7\,R_E$ (*Thompson et al.* [2005]).

- These current sheet have attained thicknesses as small as $\sim 0.1\,R_E$ (*Sergeev et al.* [1990]). This thickness should be compared to characteristic values of $\sim 5\,R_E$ an hour before substorm onset (*McPherron et al.* [1987], *Sanny et al.* [1994]).
- The spatial and temporal scales, as well as overall structure, differ appreciably in the growth and expansion phases of substorms (*Sergeev et al.* [1993]).
- Bifurcated current sheets have been observed (*Nakamura et al.* [2002], *Runov et al.* [2003], *Sergeev et al.* [2003]).
- There is a small (approximately 1 nT) normal component of the magnetic field in the current sheet (*Sergeev et al.* [1993]). But this normal component can be overwhelmed by the shear (B_y) component of the magnetic field (*Sergeev et al.* [1993]).
- The current density increases by a factor of 5 to 10 over the course of the growth phase (*Sergeev et al.* [1993]).

1.4 Review of Prior Work

Erickson and Wolf [1980] argue that slow, steady, lossless convection in Earth's magnetotail must be time-dependent. Under those conditions, the specific entropy of any particular magnetic flux tube is conserved as it convects. Assuming a value of $\gamma = \frac{5}{3}$ (appropriate for a plasma with three degrees of freedom), *Erickson and Wolf* [1980] consider what would happen to the pressure when flux tubes convect from $60R_E$ downtail to the inner dipole-like region of the magnetosphere (in the vicinity of 10 R_E downtail). They use a few semi-empirical magnetic field models [namely, those of *Olson and Pfitzer* [1974], *Beard* [1979] (to which Earth's dipole field was added), and *Voigt* [1981]], and assume approximate balance between the thermal pressure in the plasma sheet and the magnetic pressure in the magnetotail lobes. They find that this convection leads to very high pressures in the convecting flux tubes—much higher than observed—once the flux tubes reach the inner magnetosphere. *Erickson and Wolf* [1980] argue, on the basis of this "pressure-balance inconsistency" and other lines of evidence, that "Apparently, flux tubes do not convect, in an approximately lossless and adiabatic way, from $x_e \approx -60\,[R_E]$ to the dipole-like field region at $x_e \approx -10\,[R_E]$" [*Erickson and Wolf*, 1980, P. 898]. The authors suggest the magnetospheric substorm as the means through which the magnetosphere avoids this "pressure-balance inconsistency."

Figure 1.2 illustrates the nature of the 'Erickson-Wolf' problem in a more pictorial manner. The flux tube in the far magnetotail has a much greater volume than its counterpart in the near-Earth magnetotail. Using the semi-empirical magnetic field model of *Tsyganenko* [1996], one can determine that the adiabatic convection of a flux tube from 60 R_E in the far magnetotail to 10 R_E in the near-Earth magnetotail would require an increase in the pressure by a factor of nearly 800. A calculation of the ratio of the pressures at those distances (assuming a balance between thermal pressure and magnetic pressure in the lobes) indicates an actual increase of the pressure of less than a factor of 3 between $x = -60$ R_E and $x = -10$ R_E. This calculation (the nature of which is discussed in more detail in Chapter 2) lends credence to Erickson and Wolf's arguments.

Schindler and Birn [1982] have developed a self-consistent theory of time-dependent convection in Earth's magnetotail in two dimensions [in the x-z plane in Geocentric Solar Magnetospheric coordinates, with the x-axis pointing toward the Sun and the z-axis pointing in the direction of the north magnetic pole (Appendix 3 of *Kivelson and Russell* [1995])]. This model, constructed from the equations of ideal MHD, is appropriate for quiet times in the magnetotail. The resulting solutions are appropriate only for the tail-like region of the magnetosphere; the inner magnetosphere is excluded. Using this model, *Schindler and Birn* [1982] find that steady states are possible in the magnetotail, but only under very restrictive conditions. *Schindler and Birn* [1993] followed up on this earlier work by explicitly investigating the formation of thin current sheets in the near-Earth region through the application of perturbations to the boundary conditions of a one-dimensional sheet equilibrium.

Erickson [1984] has self-consistently modeled the convection of plasma sheet flux tubes in two dimensions. His model includes Earth's dipole field, and so it is not limited to the asymptotic tail limit of *Schindler and Birn* [1982]. *Erickson* [1984] has modeled the convection of plasma sheet flux tubes as a quasi-static sequence of equilibria preserving the specific entropy of a flux tube. His results confirm the time-dependent nature of lossless, adiabatic convection of magnetic flux tubes found by *Erickson and Wolf* [1980] and *Schindler and Birn* [1982]. He also sees the development of a minimum in equatorial magnetic field strength in the near-Earth plasma sheet, suggesting the development of an X-line there. The formation of an X-line in this region would signal a break-down of the ideal MHD conditions necessary for use of this model. This development could serve as the instability leading to the onset of the expansion phase.

Using the 'magnetofrictional method' of *Chodura and Schlüter* [1981], *Lee et al.* [1995] have constructed global MHD equilibria in the noon-midnight meridian with the entropy per flux tube specified as a constraint. They argue that the formation of very thin current sheets is favored by the presence of larger values of the entropy or higher gradients in the entropy. They also propose an "entropy anti-diffusion instability" that would accelerate the formation of such a thin current sheet.

Lee et al. [1998] have extended the work of *Lee et al.* [1995] by using the 2-D global equilibria presented in the earlier work as initial configurations that are then allowed to evolve in time under the influence of a pressure diffusion term in the governing MHD equations. *Lee et al.* [1998] were then able to further investigate the "entropy anti-diffusion instability" proposed by the earlier authors.

1.5 Mechanism

I begin my investigation into the nature of the mechanism for current sheet thinning with the following argument. Consider the situation in the magnetosphere at the beginning of the growth phase, as depicted in Figure 1.4. Once the IMF turns southward at the start of the growth phase of a 'classic' substorm, magnetic reconnection at the dayside magnetopause 'erodes' magnetic flux therefrom; as a result, the magnetopause advances Earthward by 0.5 to 1.0 R_E. This advance is halted after a period of about 15 minutes. Since magnetic reconnection continues at the dayside magnetopause, magnetic flux must be replenished on the dayside by a flow of plasma from the nightside magnetopause. (Otherwise the magnetopause would continue to advance Earthward.) I examine the implications of adiabatic convection for this flow. If the specific entropy of magnetic flux tubes is conserved, then the magnetic flux at the dayside magnetopause can be replenished by a 'flux reservoir' located at a limited range of distances in the near-Earth magnetotail. Magnetic flux tubes from this region convect approximately along contours of constant entropy to the dayside magnetopause. Since the Erickson and Wolf constraint greatly restricts the replenishment

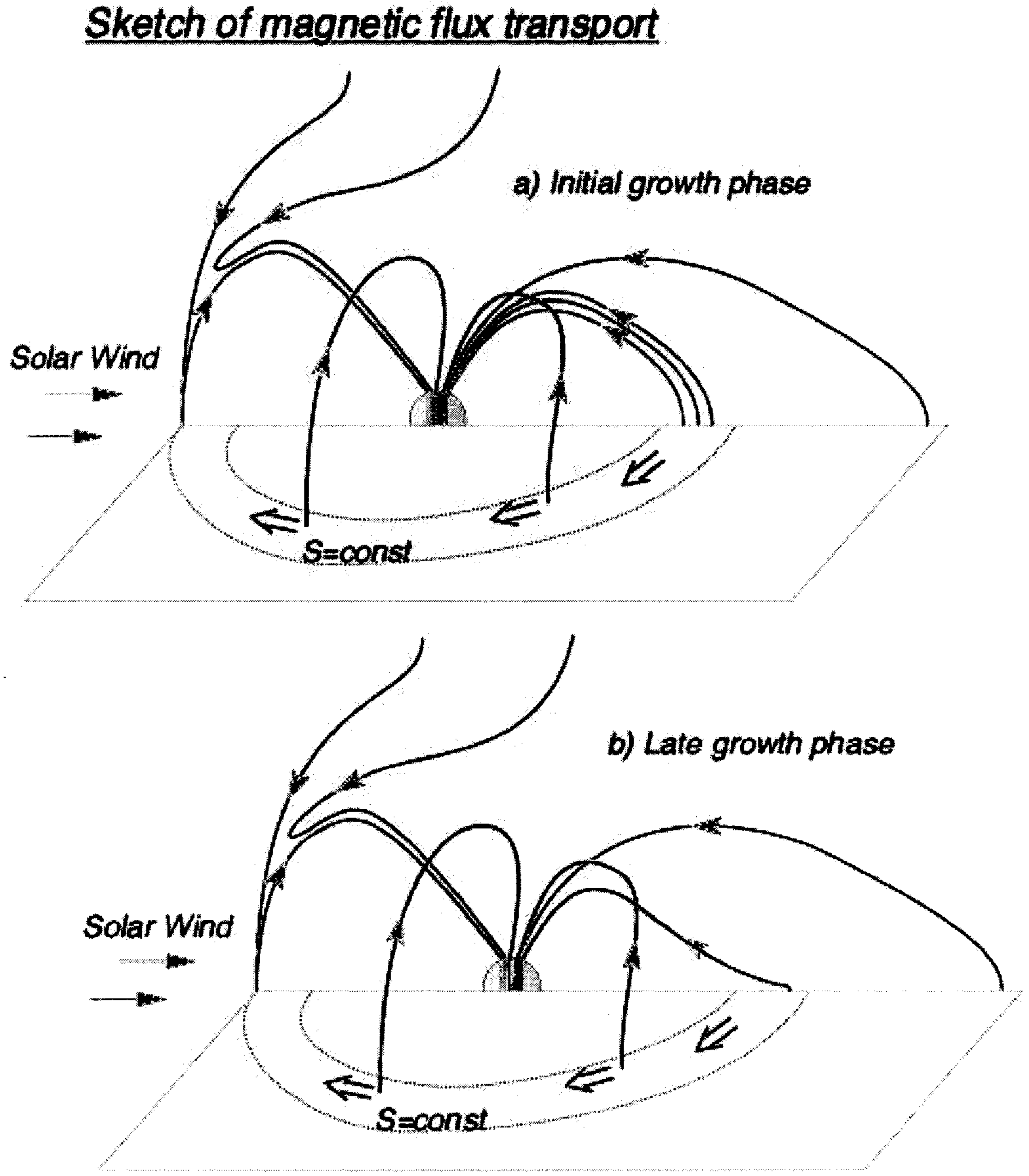
Sketch of magnetic flux transport
a) Initial growth phase
Solar Wind
S=const
b) Late growth phase
Solar Wind
S=const

Figure 1.4. Current sheet thinning mechanism. Depiction of the mechanism proposed for current sheet thinning in the late growth phase of magnetospheric substorms

of the 'flux reservoir' from regions farther tailward, I argue that the depletion of magnetic flux in this 'flux reservoir' leads to the formation and thinning of a current sheet there.

This mechanism allows me to estimate the time needed to evacuate the near-Earth 'flux reservoir.' I argue that this time is consistent with the duration of the substorm growth phase. A detailed calculation is provided in Appendix E. Let us consider the downtail extent of the magnetic flux reservoir to be 4 R_E and its cross-tail extent to be 10 R_E. The typical strength of the magnetic field in this region is 50 nT. Using a cross-polar cap electric potential Φ_E of 50 kV, which is the rate at which magnetic flux is transported from the dayside to the nightside (and vice versa)—and therefore the rate at which it must be removed from the flux reservoir—I can estimate the time in which the magnetic flux in the reservoir is depleted to be approximately 30 minutes. This is in good agreement with the duration of the substorm growth phase.

As we will soon see in Chapter 2, this mechanism allows me to predict the location of current sheet thinning. Using a profile of the specific entropy in the equatorial plane, one can estimate the region in the near-Earth magnetotail from which magnetic flux can convect adiabatically to replace magnetic flux eroded at the dayside magnetopause. This region in the near-Earth magnetotail maps to the dayside magnetopause along contours of specific entropy.

In summary, I propose that current sheet thinning occurs because of the evacuation of the near-Earth flux reservoir by convection to replace magnetic flux that is eroded on the dayside. The proposed mechanism predicts basic properties of current sheet thinning, such as

- location,
- temporal evolution, and
- dynamics.

Other mechanisms for current sheet thinning make no such predictions. This mechanism does not depend on either perturbations in boundary conditions (as suggested by *Schindler and Birn* [1993]) or on the diffusion of pressure (as proposed by *Lee et al.* [1998]).

1.6 Model Assumptions and Limitations

This model explicitly assumes that convection during the substorm growth phase can be described as slow and adiabatic. In order to utilize the assumption that specific entropy on magnetic flux tubes is conserved, I assume that

- the 'frozen-in flux' approximation holds;
- the number of particles in a magnetic flux tube is conserved; and
- no energy is transferred into or out of the flux tubes other than by adiabatic (slow) compression or decompression of the flux tubes.

I will discuss these assumptions in much more detail in Section 2.6.1.

This model does not explicitly account for non-ideal effects such as magnetic reconnection. It is assumed that the energy flux from the ionospheric footprints of flux tubes is negligible. (A relevant calculation is detailed once the necessary tools have been described in Chapter 2.)

This analysis could be extended to take into account the "demagnetization" of ions. Associated effects become important for gradients on the order of the ion inertial length $\frac{c}{\omega_{pi}}$ or the ion gyroradius. $[\omega_{pi} = \left(\frac{n_i Z^2 e^2}{m_i \epsilon_0}\right)^{\frac{1}{2}}, r_{gi} = \frac{v_{ti}}{\omega_{ci}}]$. That work is left for future research.

1.7 Scope of the Dissertation

This dissertation presents an investigation of the mechanism proposed above for current sheet thinning during the late growth phase of substorms.

Chapter 2 describes the development of a suite of computer programs that allow the calculation of the flux tube volume, pressure, and specific entropy pertaining to a magnetic configuration described by the *Tsyganenko* [1996] semi-empirical magnetic field model. These tools are used to argue further for the plausibility of the suggested mechanism. Yet this mechanism cannot be verified without the use of a 3D MHD simulation. Chapter 3 describes the development of such a model. Chapter 4 describes the results of this model. The final chapter will summarize the results of this study.

Chapter 2

Three-Dimensional Magnetic Field and Plasma Constraints for Adiabatic Convection

It is important to examine magnetospheric properties that are central to my proposed mechanism for current sheet thinning. As discussed in the introduction, the specific entropy of a magnetic flux tube can be calculated if one knows the magnetic field along that flux tube and the pressure within it. Although one can calculate the specific entropy throughout three-dimensional space at any particular time, it often suffices to calculate that quantity only in the equatorial plane ($z = 0$) through which all magnetic flux tubes of interest pass. In a sense, I have reduced a three-dimensional problem to two dimensions. Surfaces of constant specific entropy map to contour lines of specific entropy in the equatorial plane. Magnetic flux tubes are constrained to move along these contours if the specific entropy of flux tubes is conserved.

This chapter describes the development of a computer model that uses the semi-empirical magnetic field model of *Tsyganenko* [1996] to determine the specific entropy in the equatorial plane of the magnetosphere at a particular time. The model accepts the following quantities as inputs:

- P_{dyn}, the dynamic pressure of the solar wind;
- the D_{st} index;
- $(B_y)_{IMF}$ and $(B_z)_{IMF}$, the y and z components of the IMF, respectively; and
- either the dipole tilt for the time in question; or the time (year, day, and time of day) in question, for which the dipole tilt is determined.

These input quantities are discussed further in Section 2.2. Representative results of this model are provided. These results are used to demonstrate the plausibility of my proposed mechanism for current sheet thinning.

2.1 Semi-Empirical Magnetic Field Models

Fully self-consistent three-dimensional global MHD models [e.g., *Lyon et al.* [1981], *Ogino et al.* [1986], *Wu* [1983]] of Earth's magnetosphere have been available since the early

1980's. Even though such models have become increasingly sophisticated and flexible, semi-empirical models [e.g., *Mead and Fairfield* [1975], *Tsyganenko* [1989]] have continued to find use through the years in many studies [e.g., *Pulkkinen et al.* [1991], *Pulkkinen et al.* [1992], *Pulkkinen et al.* [1994a], *Pulkkinen et al.* [1994b], *Pulkkinen and Wiltberger* [2000]]. Semi-empirical models typically describe the magnetosphere by superposing the contributions to the magnetospheric magnetic field due to various large-scale current systems in the magnetosphere. Given a set of inputs (quantities such as the solar wind pressure, components of the IMF, and some sort of activity index), these semi-empirical models utilize a large set of spacecraft data to find an 'appropriate' representation of the magnetospheric magnetic field for those inputs. The convenience of semi-empirical models, coupled with the extent to which they can accommodate a large range of physical conditions (through adjustment of their input parameters), helps to explain their continued use, as does their dependence on actual spacecraft data and their proven track record.

Users of these semi-empirical models should bear in mind their limitations. The representation of the magnetic field in a particular region is dependent upon the availability of satellite data in that region. One should not expect fair representation in magnetospheric regions that have been only sparsely sampled by spacecraft. Also, these semi-empirical models only give average values of the magnetic field, determined using data from both quiet and active periods in the magnetosphere. And there are inherent limitations in the ways in which the various current systems are represented. For instance, it is assumed that each current system closes in certain regions. It is important to point out that empirical magnetic field models are only magnetic field models and do not contain a plasma pressure distribution. As noted, these fields are average fields and do not represent an equilibrium configuration. Specifically, the models do not contain the plasma pressure distribution which we will derive in Section 2.3.

2.2 The Tsyganenko-96 Semi-Empirical Magnetic Field Model

The *Tsyganenko* [1996] model is used in this study. It incorporates the contributions from the following major magnetospheric current systems:

- the magnetopause current system;

Input Parameter	Minimum Value	Maximum Value
P_{dyn}	0.5 nPa	10 nPa
D_{st}	-100 nT	+20 nT
IMF B_y	-10 nT	+10 nT
IMF B_z	-10 nT	+10 nT

Table 2.1. Range of input parameters for T96

- the ring current;
- the magnetotail current sheet;
- the Region 1 and 2 Birkeland current systems; and
- an interconnection term representing the penetration, at least in part, of the IMF into the magnetosphere (*Tsyganenko* [1996]).

This model, hereafter referred to as T96, provides the magnetic field due to the major current systems given above. The ranges of the input parameters accepted by T96 are given in Table 2.1. Note that the combination of this 'external' magnetic field (that due only to these current systems) with Earth's (largely dipolar) 'intrinsic' magnetic field yields the total magnetospheric magnetic field. A separate suite of subroutines called GEOPACK is used to calculate the 'intrinsic' magnetic field.

2.3 Pressure and Specific Entropy Model

The goal of the model described in this section is to determine the specific entropy in the equatorial plane of the magnetosphere for typical magnetic field configurations during the growth phase. It utilizes the values of the magnetospheric magnetic field given by T96 (used along with GEOPACK). The magnetic field is used to calculate the flux tube volume per unit magnetic flux for closed flux tubes that intersect the equatorial plane (in the domain of interest, discussed below). In the following, I will derive a pressure distribution that is consistent with the T96 magnetic field in the equatorial plane. The pressure combined with the flux tube volume then provides the specific entropy. Although I apply force balance in the equatorial plane to derive the pressure, the resulting configuration is not an exact equilibrium but rather represents an intelligent guess to an average magnetic field/plasma configuration.

This model uses a cylindrical coordinate grid (ρ, φ) in the equatorial plane of the magnetosphere. There are n_ρ points in the radial direction and n_φ points in the azimuthal direction. The radial coordinate ρ extends from $\rho = \rho_{min}$ to $\rho = \rho_{max}$; the azimuthal coordinate φ assumes the full range of values (from 0 to 2π radians). The grid is uniform in φ, but non-uniform in ρ. This choice allows for greater resolution in the near-Earth magnetosphere, where magnetic field gradients are large. As a function of its corresponding grid coordinate i, the radial coordinate is given as

$$\rho\,(i) = \rho_{min}\,\exp\,(\kappa i)\,. \tag{2.1}$$

The quantity κ is specified in terms of ρ_{min}, ρ_{max}, and n_ρ:

$$\kappa = \left(\frac{1}{n_\rho}\right)\ln\left(\frac{\rho_{max}}{\rho_{min}}\right). \tag{2.2}$$

This formulation ensures that the radial resolution $\Delta\rho$ is proportional to ρ; specifically, it yields the relation

$$\Delta\rho = \kappa\rho. \tag{2.3}$$

The user specifies ρ_{min}, ρ_{max}, n_ρ, and n_φ, as well as P_{dyn}, D_{st}, $(B_y)_{IMF}$, and $(B_z)_{IMF}$. For a typical high-resolution run of this code, we used the values given in Table 2.2. For these values, the maximum radial resolution at $\rho_{min} = 5\,R_E$ is $\Delta\rho = 0.17\,R_E$. The angular resolution of this grid is 0.038 radians, or 2.2 degrees; that angular distance corresponds to $0.2\,R_E$ at $\rho_{min} = 5\,R_E$.

I calculate the pressure under the assumption that the (thermal) pressure gradient force balances magnetic forces since inertial forces are small during the growth phase (Section 1.1). Thereby neglecting terms in the ideal MHD equation (Equation 1.2) involving the momentum density $\rho\mathbf{v}$, I find that I am left with

$$\nabla P = \mathbf{J} \times \mathbf{B}. \tag{2.4}$$

Input parameter	Value
ρ_{min}	5 R_E
ρ_{max}	80 R_E
n_ρ	80
n_φ	164
P_{dyn}	1.0 nPa
D_{st}	-15 nT
$(B_y)_{IMF}$	+1.0 nT
$(B_z)_{IMF}$	+1.0 nT

Table 2.2. Input parameters for reference run

Utilizing Ampère's law in the form of Equation 1.5

$$\mathbf{J} = \left(\frac{1}{\mu_0}\right)(\nabla \times \mathbf{B}), \tag{2.5}$$

I can write

$$\nabla P = \left(\frac{1}{\mu_0}\right)[(\nabla \times \mathbf{B}) \times \mathbf{B}]. \tag{2.6}$$

The gradient in pressure is related to the differential dP of the pressure through the expression

$$dP = \nabla P \cdot d\mathbf{s}. \tag{2.7}$$

Here $d\mathbf{s}$ denotes an element of length. Integrating, I obtain

$$P = \int (\nabla P \cdot d\mathbf{s}) \tag{2.8}$$

$$P = \left(\frac{1}{\mu_0}\right)\int [(\nabla \times \mathbf{B}) \times \mathbf{B}] \cdot ds. \tag{2.9}$$

With the knowledge of **B** from the T96 model, this integral is evaluated throughout the equatorial plane.

I modified the magnetic field line tracing subroutine supplied with GEOPACK to compute the distribution of the magnetic flux tube volume per unit magnetic flux $V = \int \left(\frac{1}{B}\right) d\ell$ in the equatorial plane of the magnetosphere for any configuration that can be modeled by T96. The pressure combined with the specific flux tube volume then provides the specific entropy $S = PV^{\gamma}$.

2.4 Specific Entropy Model Output

This model provides quantitative insight into the distribution of the specific entropy as a constraint for magnetospheric convection. I will also discuss properties such as pressure and magnetic field magnitude in the equatorial plane. I will discuss these properties for typical magnetic field configurations and examine how they depend on IMF parameters.

2.4.1 Mapping from the Dayside Magnetopause to the Near-Earth Magnetotail Using the Specific Entropy

Figure 2.1 shows the pressure, magnetic flux tube volume (per unit magnetic flux), and specific entropy along the midnight meridian ($y_{GSM} = z_{GSM} = 0$) for the typical quiet-time magnetic field configuration displayed in the top panel of the figure. The magnetic field configuration was determined through the use of T96. Dotted vertical lines on the dayside depict the region of magnetopause erosion typical for the substorm growth phase. The corresponding values of the specific entropy are mapped back into the magnetotail. That region in the dayside corresponds to $-15\,R_E \leq x_{GSM} \leq -9\,R_E$ in the near-Earth magnetotail. If the specific entropy on magnetic flux tubes is conserved, then it is only from this near-Earth magnetotail region that magnetic flux tubes can convect to replace magnetic flux eroded from the dayside region depicted in Figure 2.1.

2.4.2 Contour Plots of the Flux Tube Volume per Unit Magnetic Flux, Pressure, and Specific Entropy in the Equatorial Plane

Figure 2.2, Figure 2.3, and Figure 2.4 show contour lines of, respectively, the magnetic flux tube volume per unit magnetic flux, the thermal pressure, and the specific entropy in the equatorial plane for a quiet T96 magnetosphere. The parameters pertaining to these

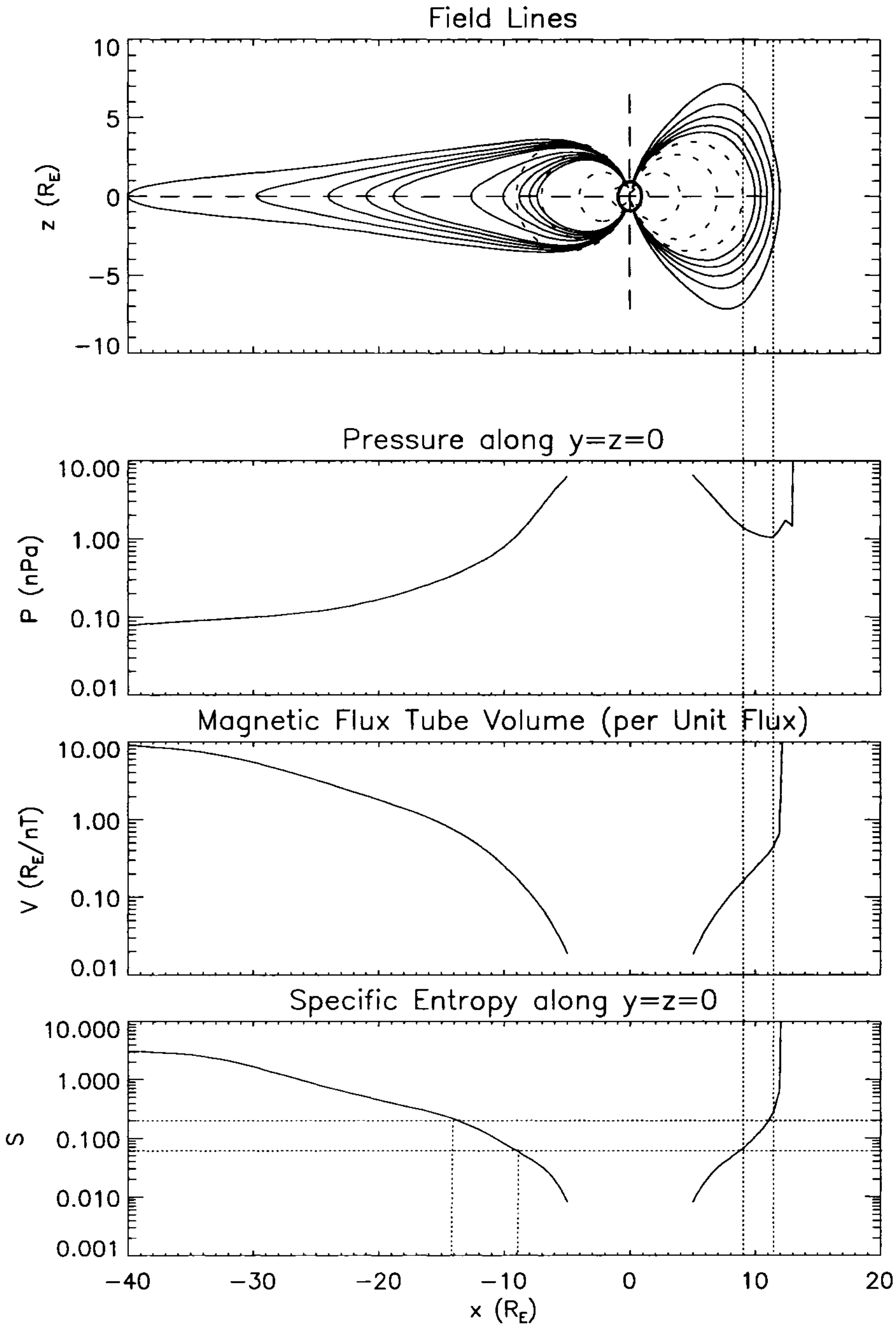

Figure 2.1. **B**, P, V, and S in the midnight meridian. The pressure, magnetic flux tube volume per unit magnetic flux, and specific entropy along y = z = 0 for the magnetic field configuration shown at top.

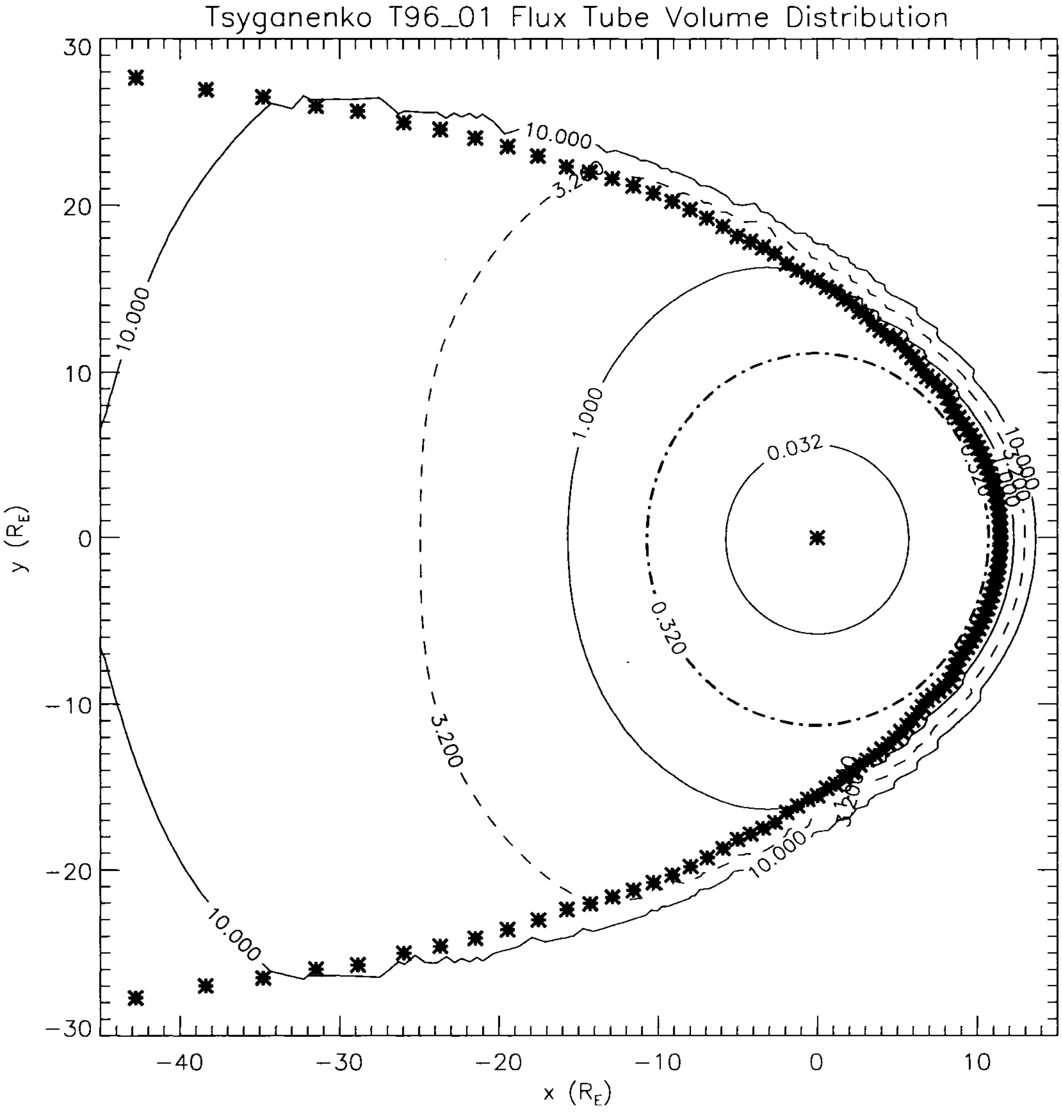

Figure 2.2. Flux tube volume contour map. Contours of the flux tube volume per unit magnetic flux (measured in R_E/nT) in the equatorial plane. The asterisks denote the position of the magnetopause.

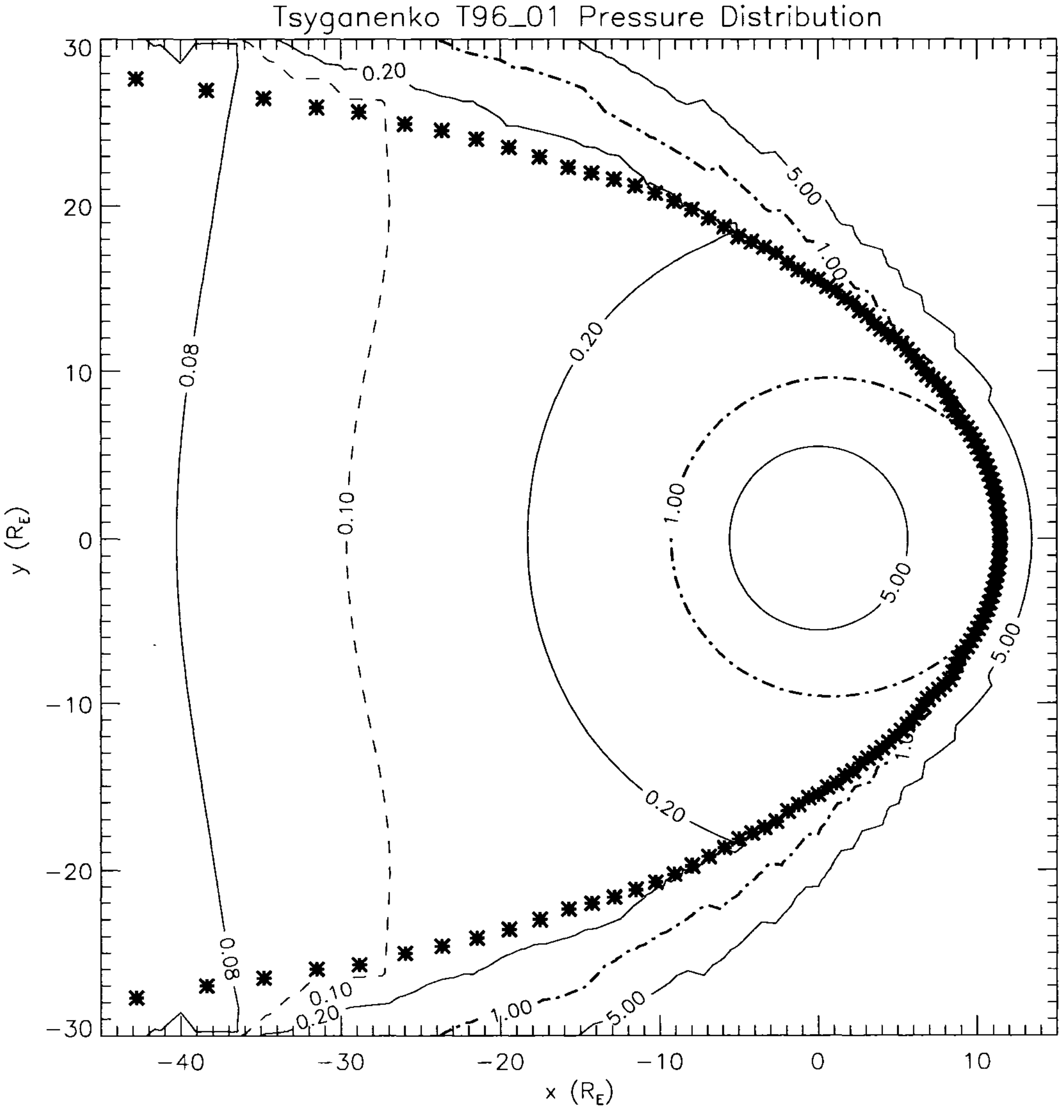

Figure 2.3. Thermal pressure contour map. Contours of the thermal pressure (measured in nPa) in the equatorial plane. The asterisks denote the position of the magnetopause.

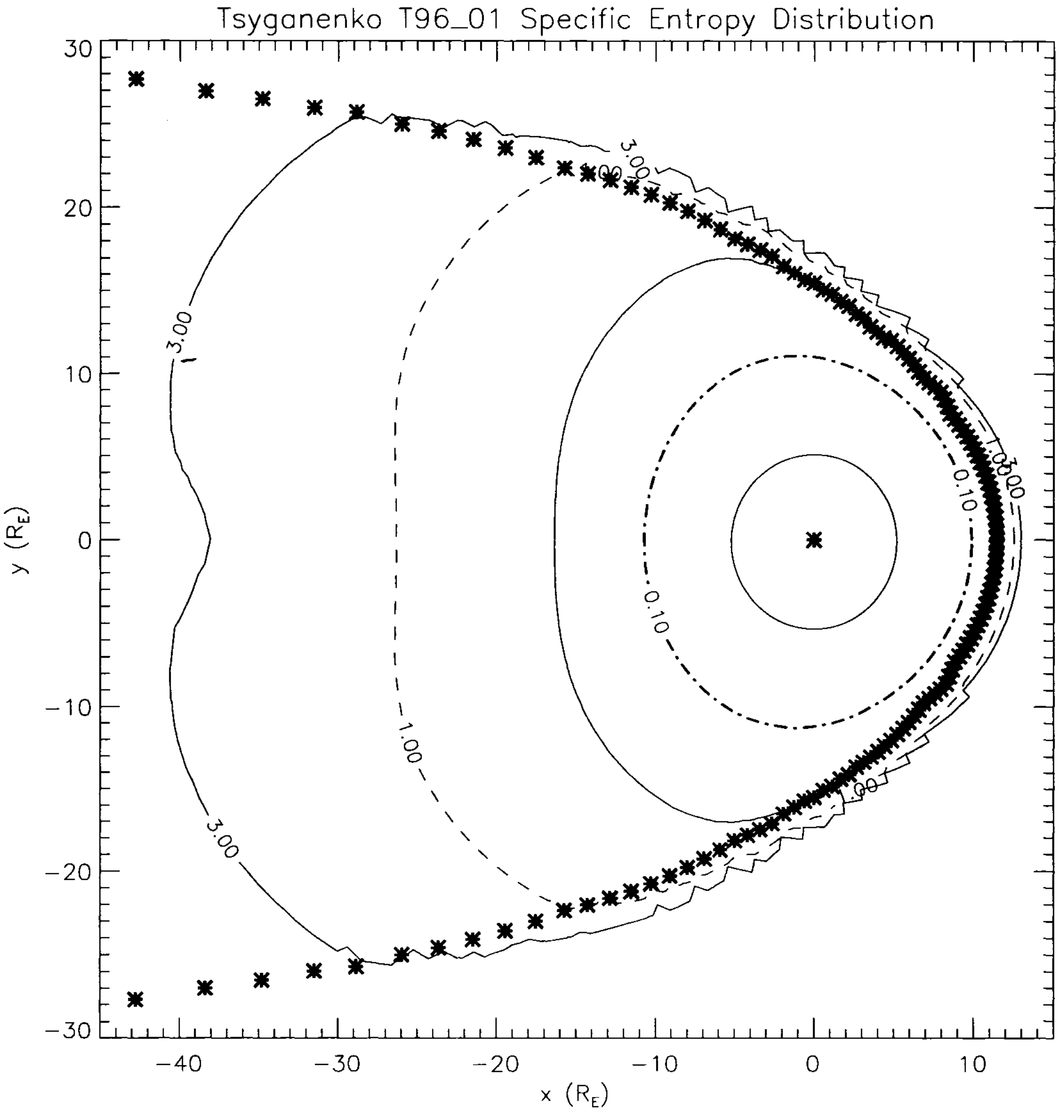

Figure 2.4. Specific entropy contour map. Contours of the specific entropy (measured in arbitrary units) in the equatorial plane. The asterisks denote the position of the magnetopause.

figures are given in Table 2.3. The asterisks in these figures indicate the location of the magnetopause.

Figure 2.2 shows the contours of the magnetic flux tube volume per unit magnetic flux, expressed in units of R_E/nT, in the equatorial plane. The contour line corresponding to 0.320 R_E/nT maps just inside the magnetopause on the dayside; it maps to $\sim 10\,R_E$ on the nightside. Note that the innermost contours of the magnetic flux tube volume per unit magnetic flux, corresponding to smaller values of that quantity, appear nearly circular. The contours deviate increasingly from circles as one moves outward (to contours corresponding to larger values of the magnetic flux tube volume per unit magnetic flux).

Figure 2.3 displays the contours of the thermal pressure in the equatorial plane. As one might expect, there is a large gradient in the pressure in the inner portion of the magnetosphere. As also shown in Figure 2.1, the pressure profile flattens considerably further downtail ($\sim 30\,R_E$ — $40\,R_E$). The contour lines lying outside the magnetopause in Figure 2.3 are spurious and should be disregarded.

The downtail pressure gradient is considerably smaller than the opposing flux tube volume gradient, such that the specific entropy increases strongly with distance from Earth. Figure 2.4 shows contour lines of the specific entropy in the equatorial plane. The solid contour between 0.10 and 1.00 (arbitrary units) corresponds to the magnetopause. It maps to $\sim 12\ R_E$ in the nightside magnetotail. This result is consistent with the results from Figure 2.1.

2.5 Parameter Study

I would like to ascertain the extent to which these results depend on the choice of input parameters to our model. To that end, I explored the effects of varying each of the input parameters P_{dyn}, IMF B_y, IMF B_z, and D_{st} while holding the others constant. I used the Tsyganenko magnetic field configuration given in Table 2.3 as a reference. These values specify a quiet magnetosphere buffeted by low-pressure solar wind carrying a weak, slightly northward, IMF. Although B_z is typically southward during the growth phase, I chose a slightly positive B_z for reasons given in the discussion of B_z and D_{st} effects. On the particular time and date chosen, Earth's dipole tilt was nearly normal to the solar wind direction.

The values assumed by the input parameters during the course of this parameter study are given in Table 2.4. Each column of this table lists the different values assigned to that parameter alone during a sequence of runs of the model. During the sequence of runs examining the influence of P_{dyn}, the reference value of 1.00 nPa was changed first to 2.00 nPa for one run, and then to 4.00 nPa for another run. All other input parameters remained at their reference values during these two runs of the model.

The results of this parameter study are illustrated in the next several figures. Figure 2.5, Figure 2.7, Figure 2.9, and Figure 2.11 illustrate the dependence of the value of the specific entropy as a function of downtail distance along $y = z = 0$ for different values of the input parameters P_{dyn}, IMF B_y, IMF B_z, and D_{st}, respectively. (Downtail distance is simply the negative of the x-coordinate in the GSM coordinate system.) Figure 2.6, Figure 2.8, Figure 2.10, and Figure 2.12 are provided to assist the reader in understanding the behavior observed in the earlier plots of the specific entropy. They each display the downtail (magnetospheric) magnetic field component B_z, the magnetic flux tube volume (per unit magnetic flux) V, and the thermal pressure P along the midnight meridian as functions of the downtail distance, as well as the specific entropy shown in the earlier figures.

2.5.1 Variation of the dynamic solar pressure $\mathbf{P_{dyn}}$

In this portion of the parameter study, the dynamic pressure P_{dyn} of the solar wind was increased from its reference value of 1.00 nPa to the values 2.00 nPa and 4.00 nPa. Figure 2.5 shows that the specific entropy is comparable for the different values of P_{dyn} from the inner model boundary of $5\,R_E$ to $\sim 25 - 27\,R_E$ tailward and the entropy is smaller for higher dynamic pressure in the mid and far tail. Overall, however, the specific entropy changes by less than a factor of 2 in the mid and far tail regions for each factor of 2 in the dynamic pressure.

Upon examining the plot of magnetospheric B_z in Figure 2.6, one sees that this distance corresponds to the minimum in the plot of this quantity for the case wherein $P_{dyn} =$ 4.00 nPa. The corresponding minimum for the case with $P_{dyn} = 2.00$ nPa lies somewhat further tailward, whereas the minimum for the reference case with $P_{dyn} = 1.00$ nPa lies even further tailward. The distribution of B_z (including the minimum location) is likely a result of the increasing compression of the magnetosphere with increasing solar wind dynamic

Parameter	**Value**
P_{dyn}	1.00 nPa
IMF B_y	+1.00 nT
IMF B_z	+1.00 nT
D_{st}	-15.00 nT
IOPT	1
Year	1980
Day	66
Hour	21
Minute	0
Second	0

Table 2.3. Input Parameters for the reference case used in the parameter study. IOPT is a program parameter with no physical significance that has been included here for the sake of completeness. Note that these values represent a relatively quiet magnetosphere.

	P_{dyn} (nPa)	IMF B_y (nT)	IMF B_z (nT)	D_{st} (nT)
Reference Value	1.00	+1.00	+1.00	-15.00
	2.00	-2.00	-5.00	-25.00
	4.00	-1.00	-2.00	0.00
		0.00	-1.00	+10.00
		+2.00	0.00	
			+2.00	
			+5.00	

Table 2.4. Parameter values used in the parameter study

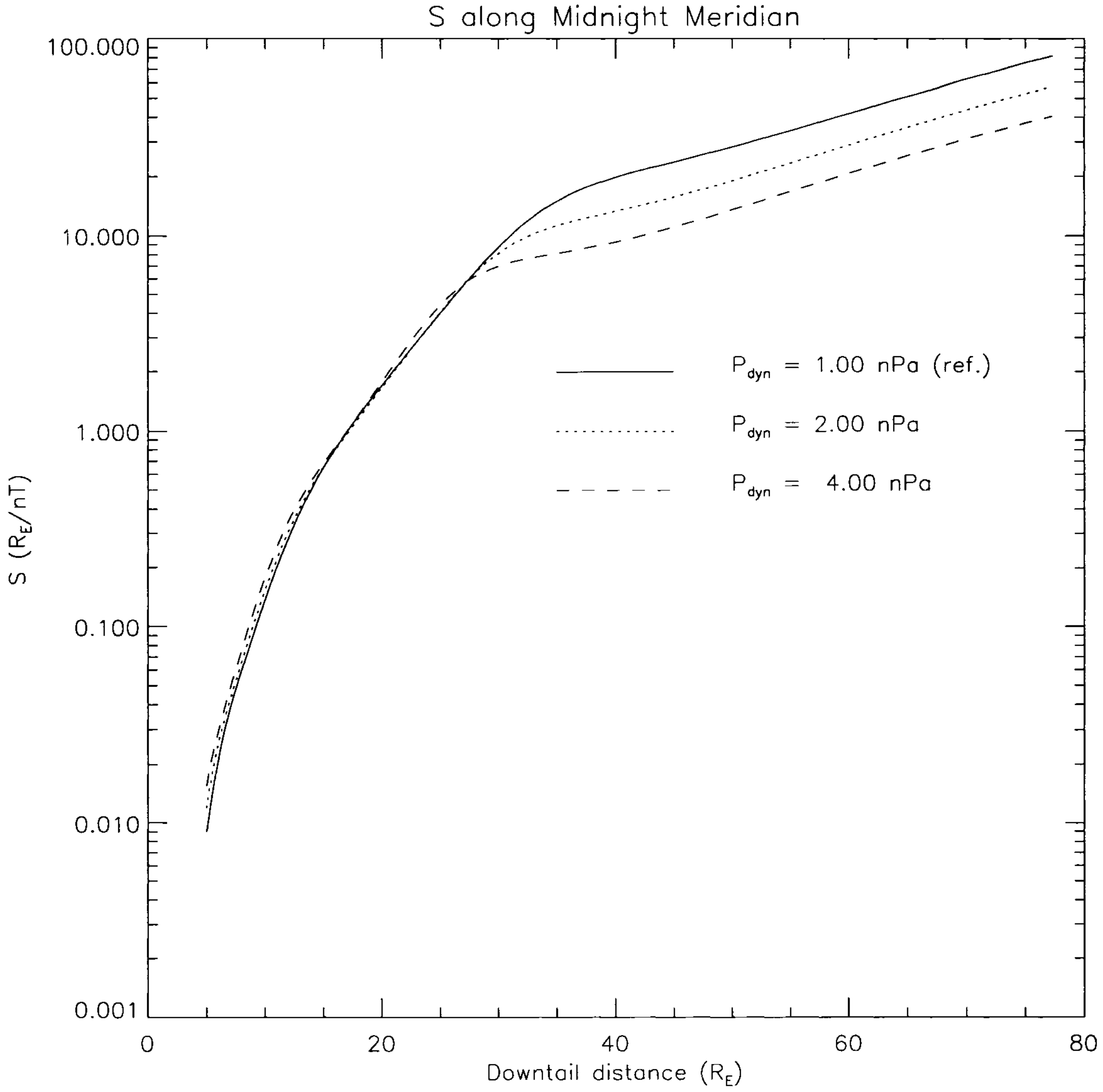

Figure 2.5. Dependence of specific entropy on P_{dyn}. The specific entropy S along y = z = 0 for different values of the solar wind dynamic pressure P_{dyn}.

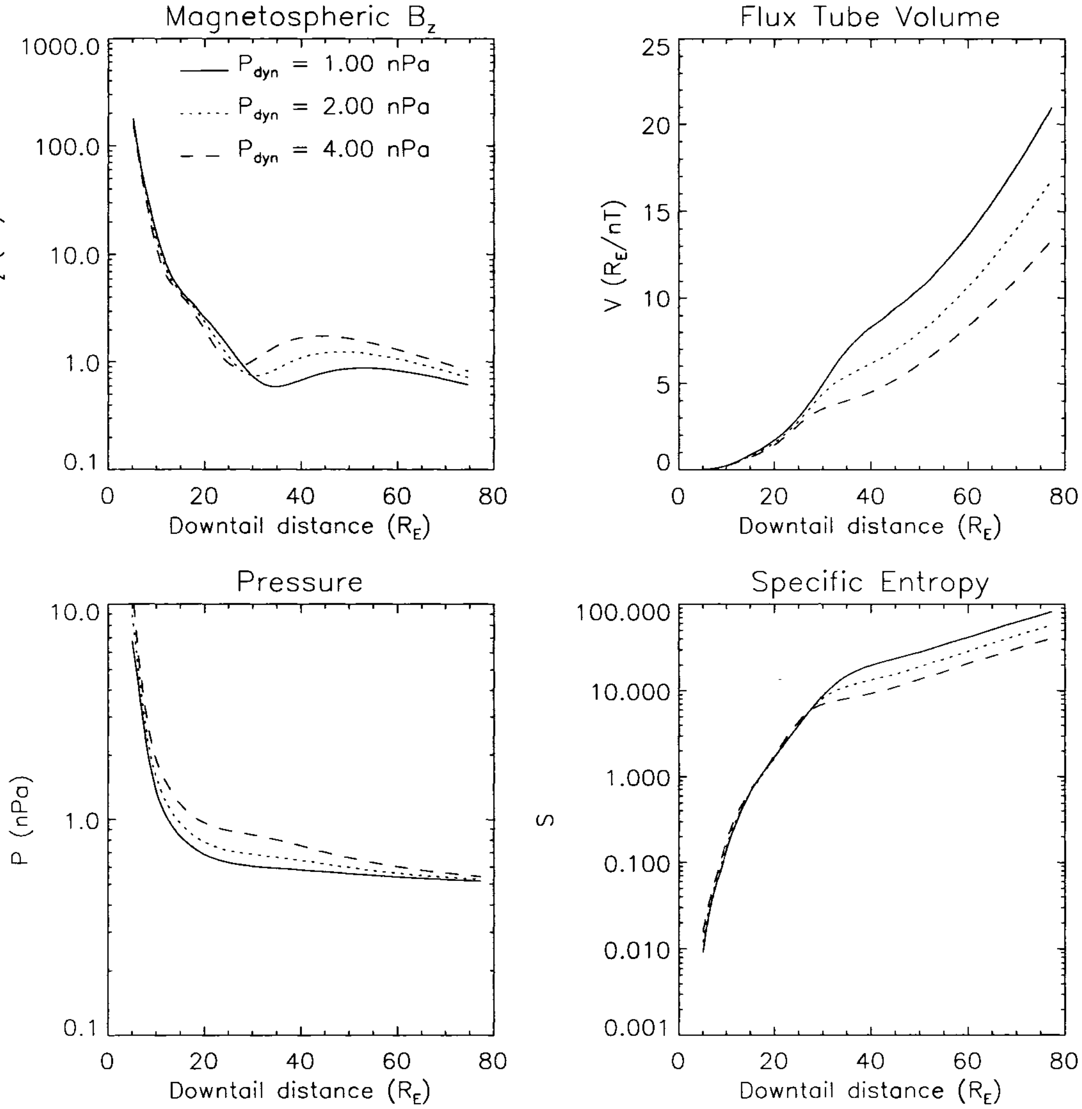

Figure 2.6. Dependence of B_z, V, P, and S on P_{dyn}. Magnetospheric B_z, magnetic flux tube volume (per unit magnetic flux) V, thermal pressure P, and specific entropy S along y = z = 0 for different values of the solar wind dynamic pressure P_{dyn}. Note that the plot of the specific entropy is the same as that in Figure 2.5.

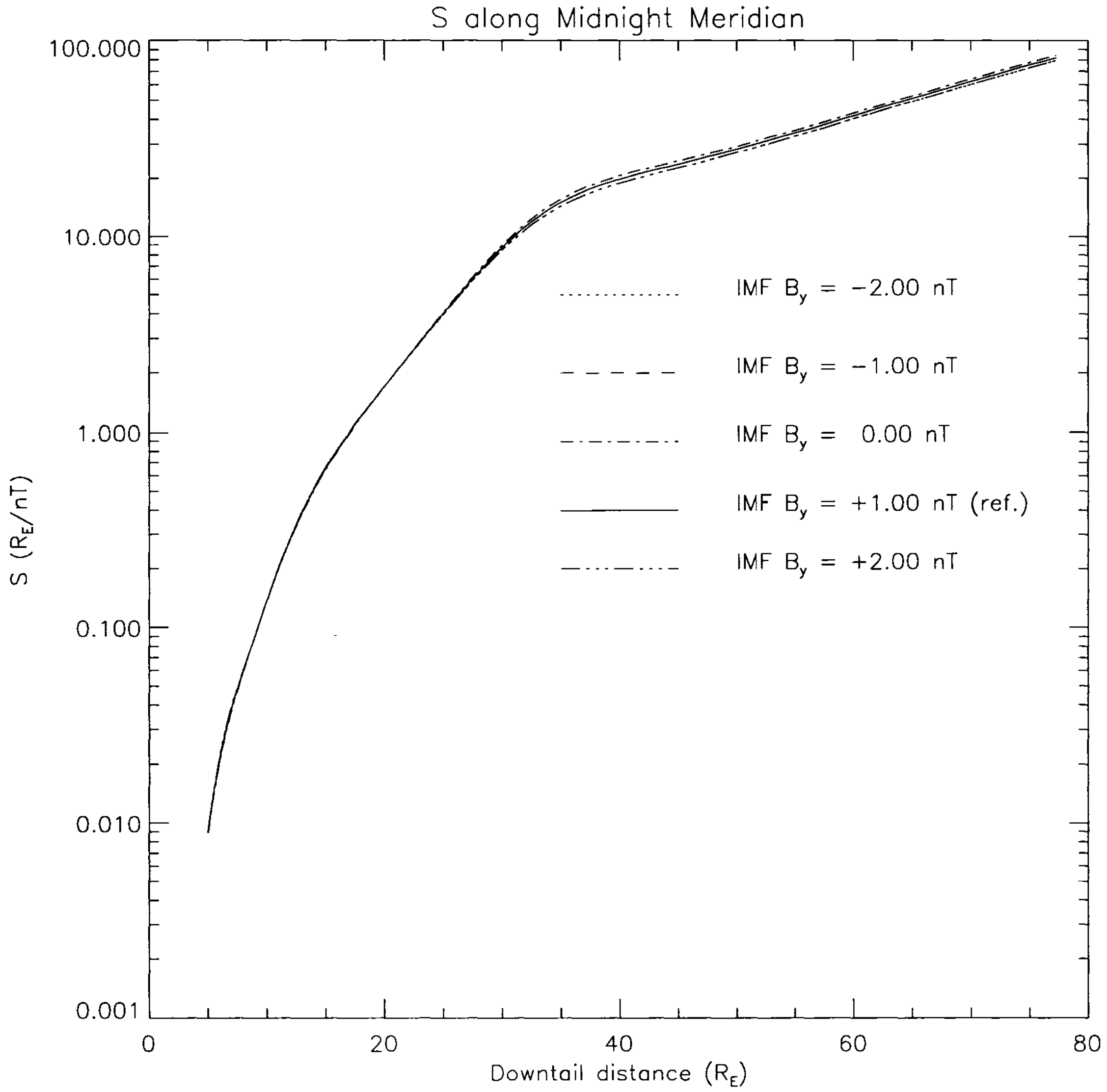

Figure 2.7. Dependence of specific entropy on IMF B_y. The specific entropy S along y = z = 0 for different values of IMF B_y.

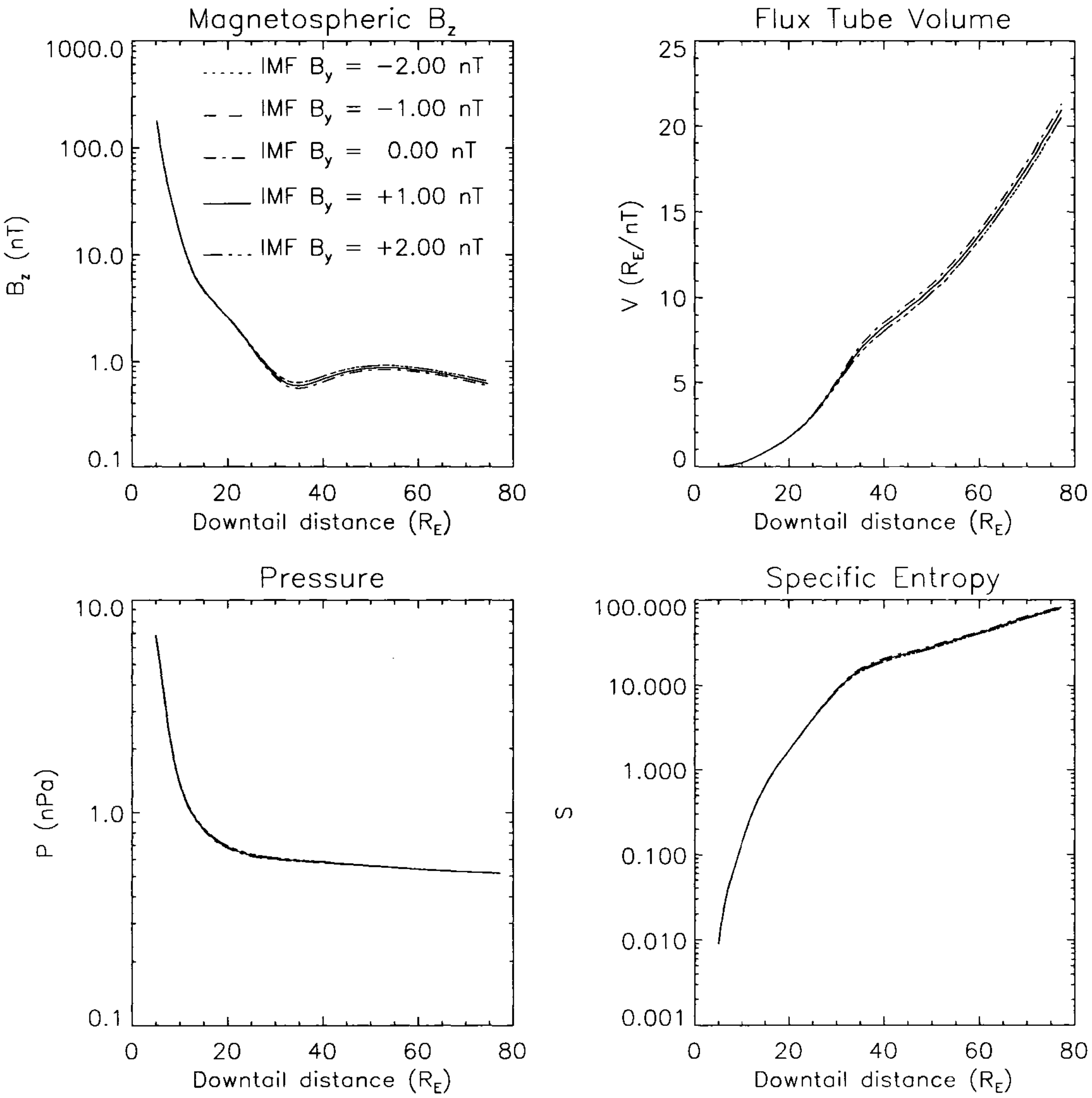

Figure 2.8. Dependence of B_z, V, P, and S on IMF B_y. Magnetospheric B_z, magnetic flux tube volume (per unit magnetic flux) V, thermal pressure P, and specific entropy S along y = z = 0 for different values of IMF B_y. Note that the plot of the specific entropy is the same as that in Figure 2.7.

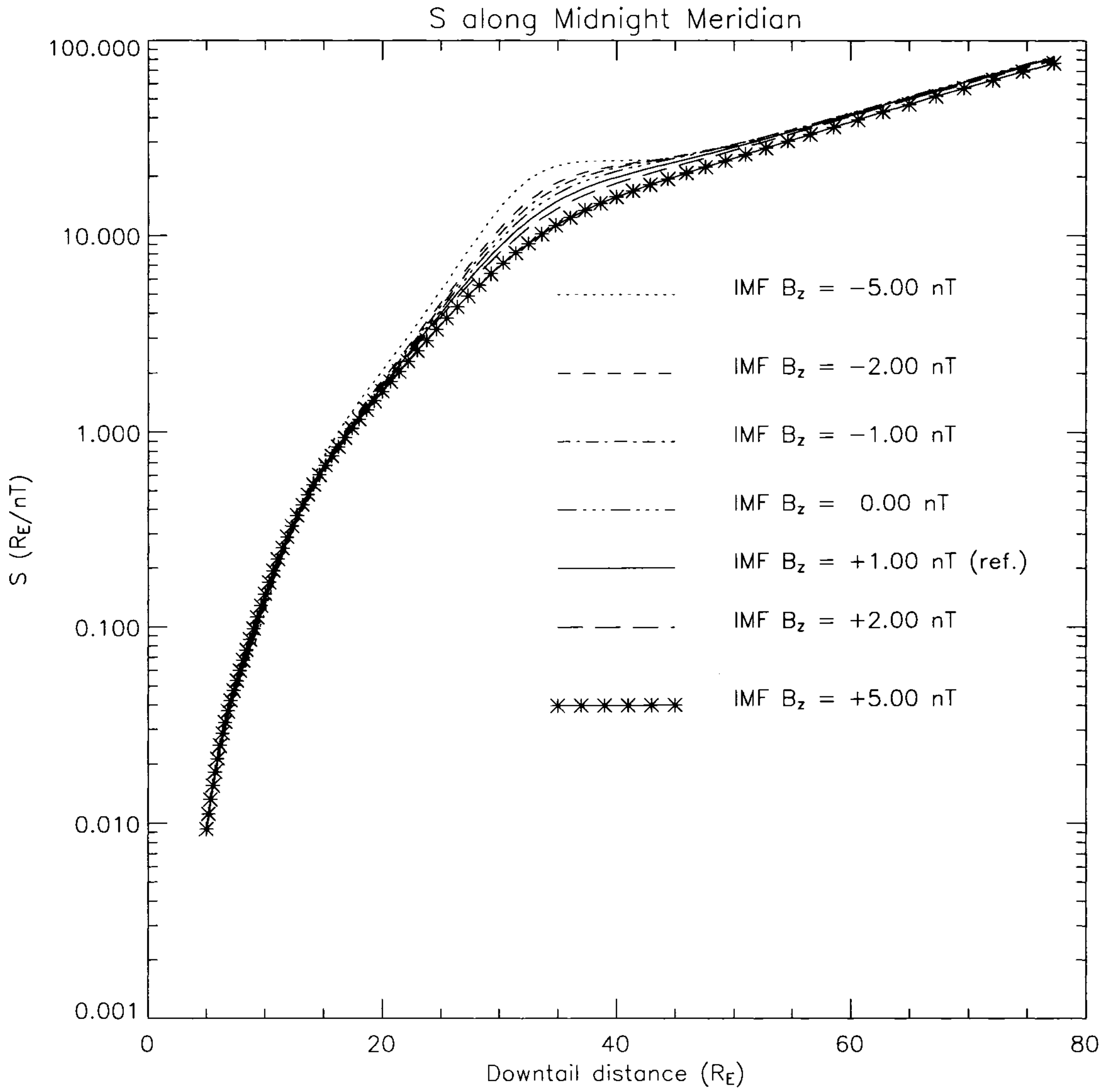

Figure 2.9. Dependence of specific entropy on IMF B_z. The specific entropy S along y = z = 0 for different values of IMF B_z.

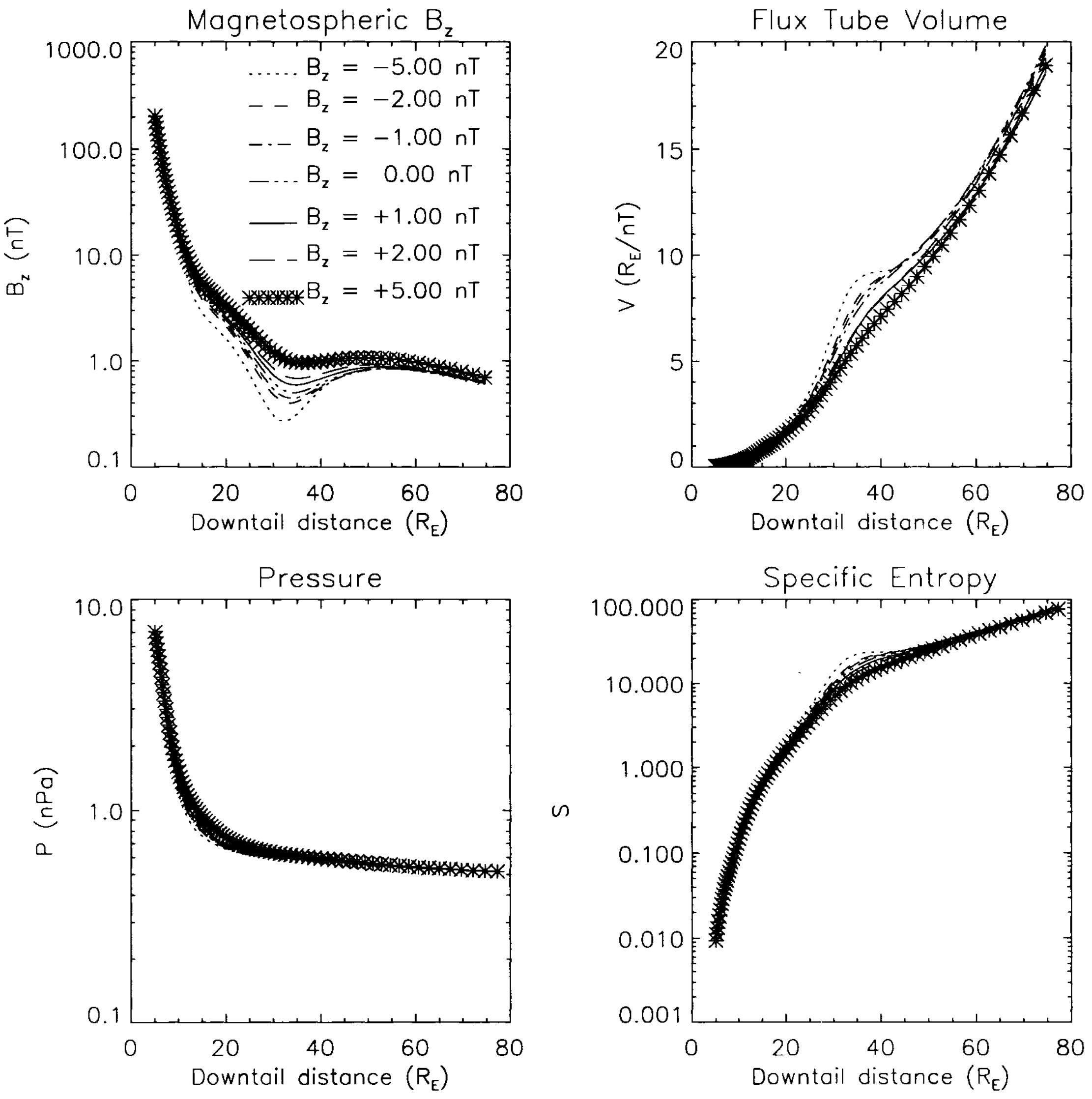

Figure 2.10. Dependence of B_z, V, P, and S on IMF B_z. Magnetospheric B_z, magnetic flux tube volume (per unit magnetic flux) V, thermal pressure P, and specific entropy S along y = z = 0 for different values of the IMF B_z. Note that the plot of the specific entropy is the same as that in Figure 2.9.

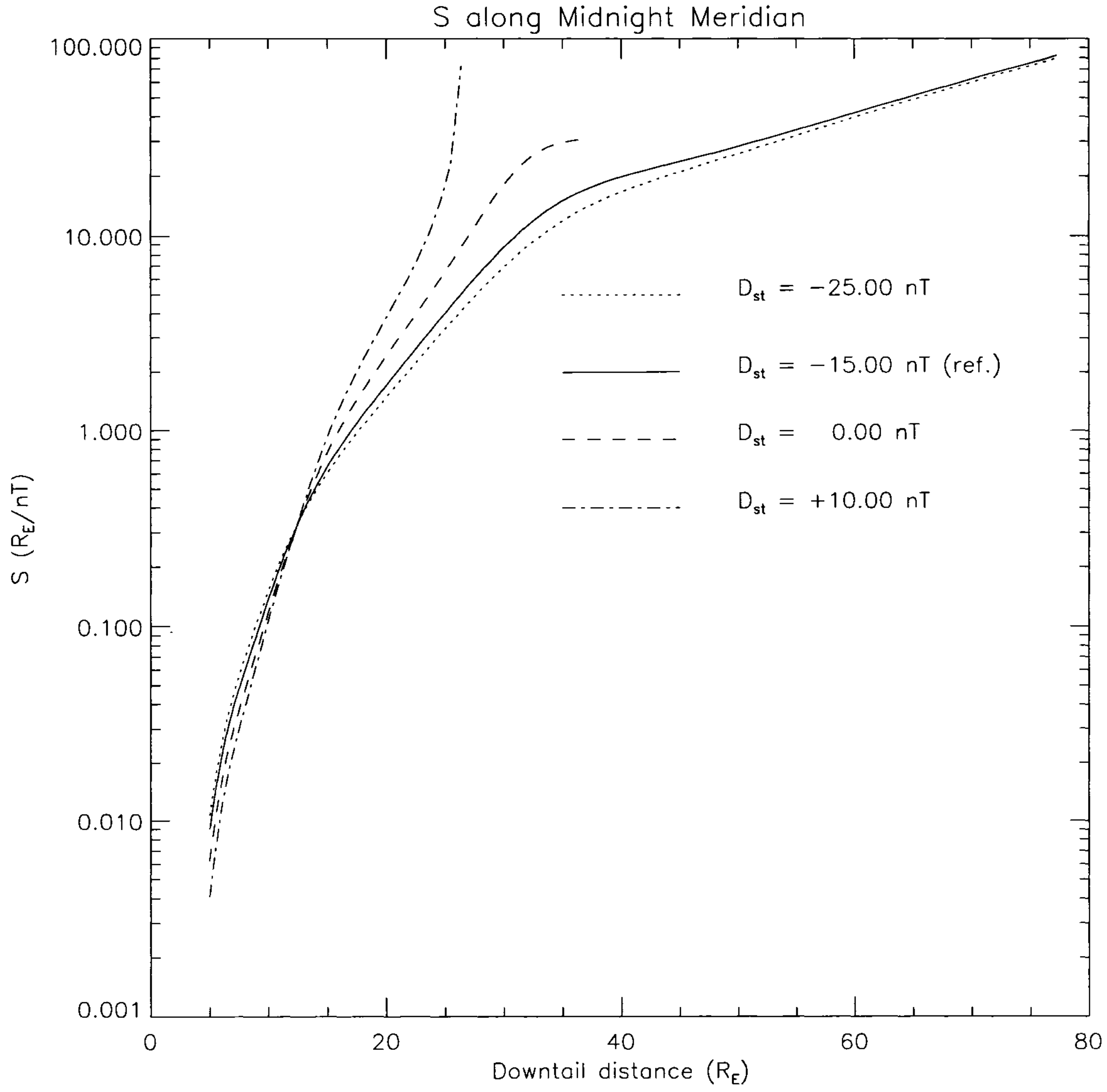

Figure 2.11. Dependence of specific entropy on D_{st}. The specific entropy S along y = z = 0 for different values of the D_{st} index.

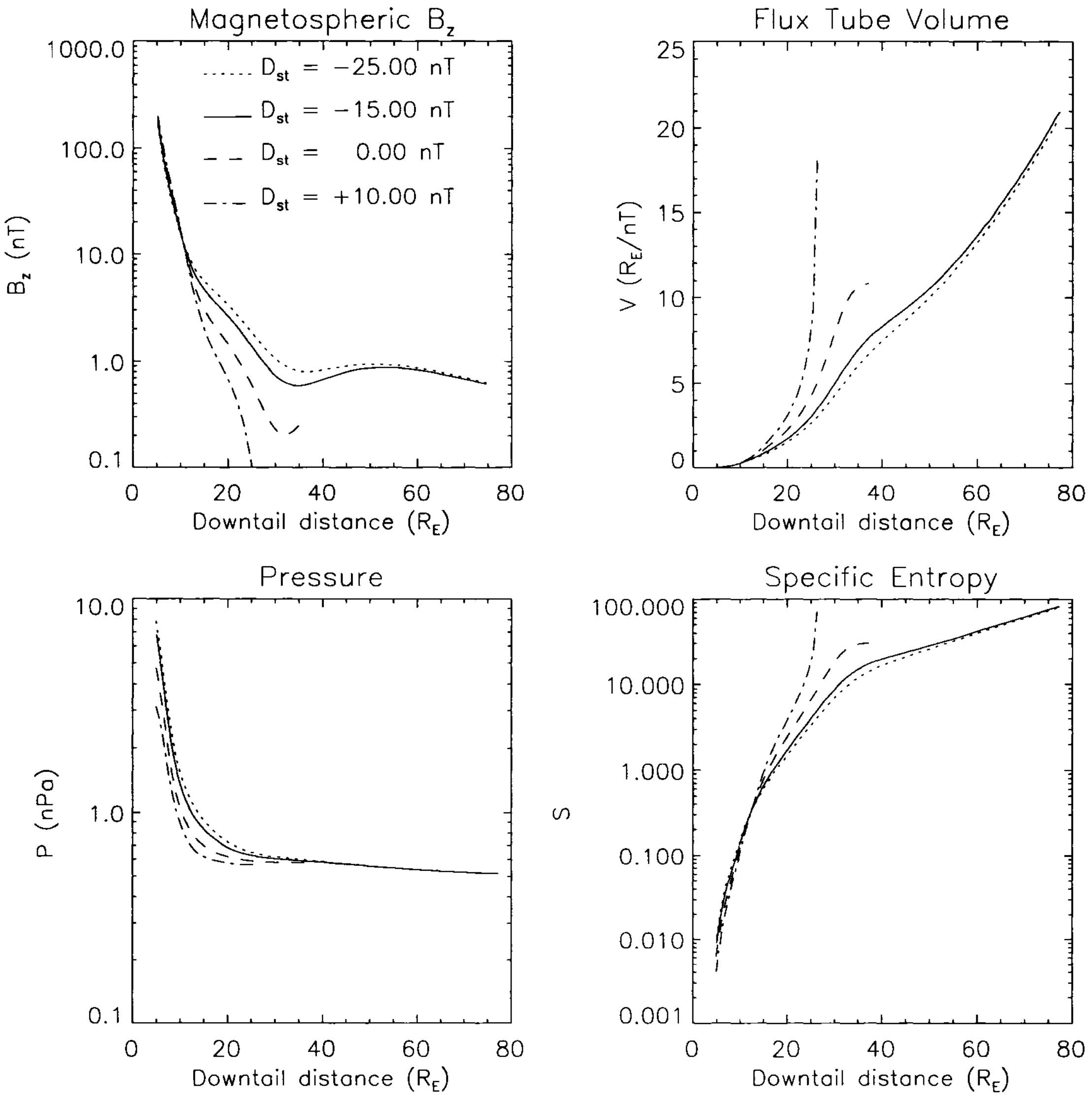

Figure 2.12. Dependence of B_z, V, P, and S on D_{st}. Magnetospheric B_z, magnetic flux tube volume (per unit magnetic flux) V, thermal pressure P, and specific entropy S along y = z = 0 for different values of the D_{st} index. Note that the plot of the specific entropy is the same as that in Figure 2.11.

pressure.

The B_z features are reflected in the plots of the flux tube volume, wherein one sees a maximum ratio of less than 2 between the flux tube volume corresponding to $P_{dyn} = 4.00$ nPa at a particular downtail distance and the analogous value for $P_{dyn} = 1.00$ nPa. Note that the magnetic field along a field line assumes a minimum in the equatorial plane with a value of $B \approx B_z$ such that this portion of a flux tube has the greatest contribution to the flux tube volume $V = \int \left(\frac{1}{B}\right) d\ell$.

The third panel of Figure 2.6 depicts the thermal pressure as a function of downtail distance. One sees that the thermal pressure is greater for larger values of P_{dyn} throughout the magnetotail, with the effect most pronounced at distances $\leq 40\,R_E$. In the far tail ($80\,R_E$), the thermal pressure is only slightly modified by increasing dynamic pressure. This is expected: the higher dynamic pressure has a stronger effect in the near-Earth region because the flaring angle of the magnetopause is larger. The thermal pressure is relatively smooth (as a function of downtail distance), and does not readily reflect the minimum in B_z. But that minimum is reflected in the plots of the specific entropy, in part through the contribution of the flux tube volume to that quantity. Still, the specific entropy varies, at any particular downtail distance, only by a factor slightly greater than 2, at most.

2.5.2 Variation of IMF $\mathbf{B_y}$

Figure 2.7 shows us that varying IMF B_y has very little effect on the value of the specific entropy along the midnight meridian. This result is not surprising, since one would expect the least effect of IMF B_y along that axis. Figure 2.8 lends credence to this expectation; magnetospheric B_z, flux tube volume V, and the thermal pressure P all share this behavior with the specific entropy S.

2.5.3 Variation of IMF $\mathbf{B_z}$

Figure 2.9 shows the effect of varying IMF B_z on the specific entropy. At small and large distances the effect of IMF B_z on the specific entropy is negligible. However, there is an effect in the midtail between 20 and 45 R_E where, Earthward of 30 R_E, the entropy gradient steepens and tailward the entropy flattens out for decreasing B_z up to the point where the entropy has a small maximum at $\sim 35\,R_E$ for $B_z = 5$ nT.

Looking at Figure 2.10, one sees a minimum in magnetospheric B_z of increasing depth with decreasing values of the IMF B_z. The location of that minimum is the same for the different values of the IMF. The influence of this superposition is seen in the plots of the flux tube volume: that quantity increases for decreasing values of the IMF B_z at this minimum. The influence of this input parameter is small in the pressure such that the changes in B_z and therefore the flux tube volume dominate the changes in entropy for different IMF B_z. Note that the minima in B_z may actually be somewhat artificial in the sense that they may well be a result of the sampling of both quiet and active (substorm) times. During active times reconnection and plasmoid formations actually generate negative B_z.

2.5.4 Variation of $\mathbf{D_{st}}$

Figure 2.11 shows the effect of varying the storm index D_{st} on the specific entropy. The plot for D_{st} equal to the reference value of -15.00 nT appears well-behaved, as does that for D_{st} equal to -25.00 nT. But the corresponding plots for D_{st} equal to 0.00 nT and +10.00 nT appear anomalous. Looking at Figure 2.12, one sees that the minimum in magnetospheric B_z attains rather small values for D_{st} equal to 0.00 nT and +10.00 nT. An x-line actually forms at the location of the magnetospheric minimum for the case with $D_{st} = +10.00$ nT. The anomalous behavior of these two cases suggests that we take great care in interpreting the corresponding results.

The storm index D_{st} provides a measure of the strength of the ring current. Increasingly negative values of D_{st} indicate the increasing magnitude of the ring current. As the ring current grows in magnitude, it increases the value of the magnetospheric B_z in the magnetotail. This behavior explains the larger values of magnetospheric B_z for increasingly negative D_{st}. The magnitude of the ring current is diminished for the cases with D_{st} equal to 0.00 nT and +10.00 nT, allowing for small and even negative values of magnetospheric B_z.

The plots of the specific entropy for D_{st} equal to -25.00 nT and -15.00 nT lie rather close to one another. If one restrict his consideration to downtail distances of less than $25\,R_E$, then he can also consider the cases with D_{st} equal to 0.00 nT and +10.00 nT. Even with these cases considered, one sees that the specific entropy varies considerably less than an order of magnitude among these four cases (for the limited downtail region mentioned above).

Again the results with negative values of B_z in the tail is an artifact of the sampling of active and quiet times. In the T96 model, D_{st} directly controls the magnitude of the ring current. The ring current plays an important role in the determination of the magnetic field in the near-Earth region. Note, from Table 3.1, that the allowed range of D_{st} in the T96 model is $-100\,nT \leq D_{st} \leq +20\,nT$. The values of D_{st} for which I obtained extremely small values of B_z in the magnetotail—namely, $D_{st} = 0\,nT$ and $D_{st} = +20\,nT$—are close to the maximum of that range. Accordingly, I have some concerns regarding the possible spareness of relevant data points in addition to aforementioned concerns regarding the sampling of active and quiet times.

2.6 Calculation of the Ionospheric Energy Flux Resulting from Steady Convection of Magnetic Flux Tubes

2.6.1 Motivation

In drawing conclusions about the implications of specific entropy conservation for the slow and steady convection of magnetospheric flux tubes, I have relied upon the assumptions given in Section 1.5:

- The 'frozen-in flux' approximation holds.
- The number of particles in a magnetic flux tube is conserved.
- No energy is transferred into or out of the flux tubes other than by adiabatic (slow) compression or decompression of the flux tubes.

The frozen-in condition is actually extremely well satisfied in the highly collisionless magnetospheric plasma on sufficiently large scales. Violation of the frozen-in condition occurs only on sufficiently small scales, specifically on the ion inertia scale $\lambda_i = \frac{c}{\omega_{pi}}$, which is about 100 km in the plasma sheet.

Let us consider the second assumption, regarding conservation of the number of particles in a magnetic flux tube. Particle production or loss mechanisms within the flux tube would lead to changes in the number of particles. Such mechanisms include ionization, recombination, and precipitation of particles out of the end of the magnetic flux tube. The last of these mechanisms—precipitation— is considered in the following sections. However, one would expect ionization and recombination to be significant only within or in the vicinity of the ionosphere. The vast bulk of any particular magnetic flux tube being considered in this analysis lies outside of the ionosphere. Accordingly, I disregard particle production through ionization or particle loss through recombination; precipitation out of the end of the flux tube is the only particle production or loss mechanism that I consider.

Even with the frozen-in flux approximation holding, one could envision particle drifts that carry particles out of a particular magnetic flux tube. But such drifts perpendicular to the magnetic field **B** would also carry particles into that same flux tube, replacing any that were lost. A particle drift would lead to a change in the number of particles in a flux tube only if a there is a large enough gradient in that drift across the flux tube to give rise to a difference between the number of particles leaving the flux tube and the number of particles entering the flux tube. I argue that no particle drifts give rise to appreciable violation of the conservation of particle number on magnetic flux tubes in this system.

This leaves as a potentially significant loss process the loss of particles out of the ionospheric ends of the magnetic flux tubes. Particles exiting a flux tube through these means will deposit their energy into the ionosphere.

I can calculate the energy flux into the ionosphere resulting from the steady convection of magnetic flux tubes. Once I have done so, I can determine if the calculated flux is consistent with the energy flux observed in the auroral zone.

2.6.2 Results from Derivation

The detailed derivation of the ionospheric energy flux is provided in Appendix D. Some of the key results from that derivation are reproduced here.

The energy flux out of the ionospheric end of a magnetic flux tube is given by the product of the instantaneous plasma energy density e and the instantaneous plasma speed u:

$$f = eu. \tag{2.10}$$

If the energy density e is identified as that corresponding to the internal energy of this system, then I can write

$$e = \left(\frac{3}{2}\right) P, \tag{2.11}$$

where P is identified as the thermal pressure as before. Accordingly,

$$f = \left(\frac{3}{2}\right) uP. \tag{2.12}$$

My challenge lies in determining an expression for the plasma speed u in terms of readily-available quantities. As shown in Appendix D, I can write

$$u = -\left(\frac{1}{2}\right)\left(\frac{E}{B_{msp}}\right) B_{isp} \left(\frac{1}{P^{\frac{1}{\gamma}}}\right)\left(\frac{dH}{dx}\right) \tag{2.13}$$

$$f = -\left(\frac{3}{4}\right)\left(\frac{E}{B_{msp}}\right) B_{isp} P^{1-\frac{1}{\gamma}} \left(\frac{dH}{dx}\right). \tag{2.14}$$

Here E is the magnitude of the convection electric field. B_{msp} is the magnetic field at a magnetic flux tube's intersection with the equatorial plane, and B_{isp} is the magnetic field at one of the ionospheric footpoints of the flux tube. The quantity

$$H = P^{\frac{1}{\gamma}} V \tag{2.15}$$

is simply related to the specific entropy S by

$$H = S^{\frac{1}{\gamma}}. \tag{2.16}$$

(This relationship is discussed further in Appendix D.)

2.6.3 Results of Calculations

For the purposes of my calculations, I use a constant value of 0.5 mV/m for E. This convection electric field corresponds to a cross-polar cap potential of 50 kV applied over a distance of approximately 16 R_E.

T96 is used to provide both B_{msp} and B_{isp}. The pressure and specific entropy models described in Section 2.3 are used to calculate the pressure P and the derivative $\frac{dH}{dx}$. The latter quantity is evaluated in the equatorial plane of the magnetosphere.

The ionospheric energy flux is shown as a function of the downtail distance (the distance to which a particular flux tube maps in the equatorial plane) for the reference case in Figure 2.13. The ionospheric flux is shown as a function of latitude in Figure 2.14. (The latitude in question here is the latitude of the ionospheric footprint of a magnetic flux tube, as determined through use of T96.) Various quantities affecting the value of the ionospheric energy flux are shown as functions of downtail distance in Figure 2.15.

The shape of the ionospheric flux plot in the near-Earth magnetotail is determined largely through the behavior of the magnetospheric magnetic field B_{msp}. The large magnetic field in that region strongly reduces the value of the ionospheric flux. Note that the magnitude of the derivative $\frac{dH}{dx}$ is also small here. The influence of these two trends overwhelms the (relatively) large value of the pressure P in the near-Earth tail.

The decrease of B_{msp} and the increasingly negative value of $\frac{dH}{dx}$ with downtail distance leads to the increase of the ionospheric flux to its global maximum. This maximum is reached in the vicinity of 25 to 35 R_E. It seems to coincide with the minima in both B_{msp} and $\frac{dH}{dx}$. The latter feature (namely, the minimum in $\frac{dH}{dx}$) seems to arise from a flattening of the curve of V in that region.

The ionospheric flux decreases from that point. It shortly reaches a local minimum (arising from a decrease in the magnitude of $\frac{dH}{dx}$). Note that a local maximum in B_{msp} seems to lie there, as well. It should also be noted that B_{isp} is nearly constant throughout the region of interest, varying by less than 0.51% of its average value of $\sim 5.4 \times 10^4$ nT throughout the plotted range.

It is shown that the ionospheric energy flux is appreciably greater than 100 ergs/($cm^2 \cdot$ s) for flux tubes convecting at downtail distances greater than 10 R_E. These results suggest that the steady convection of magnetic flux tubes under the constraint of conserved specific entropy on magnetic flux tubes is inconsistent with auroral observations even under extreme conditions (e.g., *Lanchester et al.* [1997], *Lummerzheim et al.* [1997]). I therefore conclude that flux eroded on the dayside cannot be replaced by magnetic flux from the mid and far tail regions. Therefore there is only a limited region in the near-Earth tail which can provide the magnetic flux reservoir for the eroded flux from the dayside.

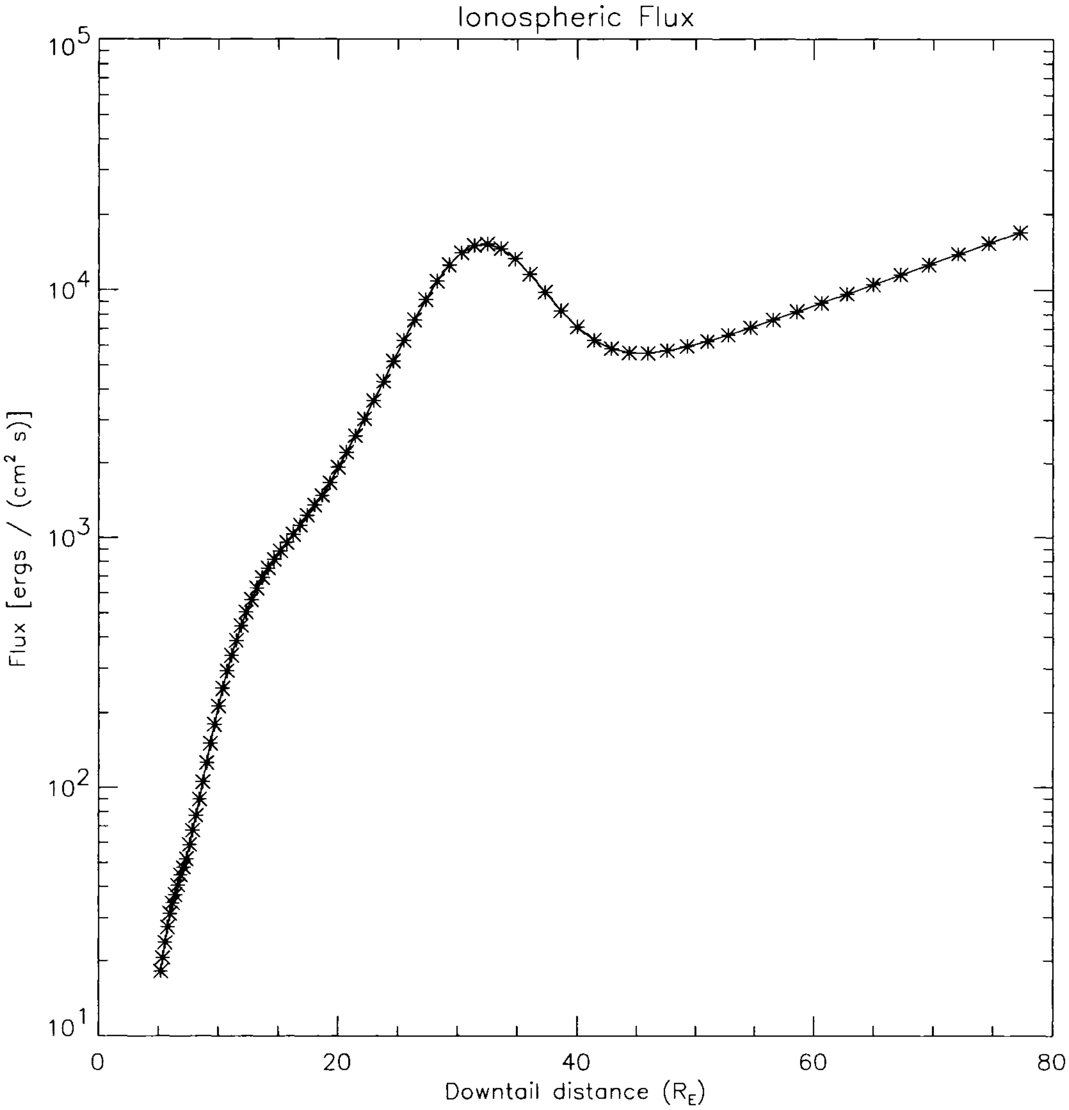

Figure 2.13. Ionospheric energy flux as a function of downtail distance along the midnight meridian (y = z = 0).

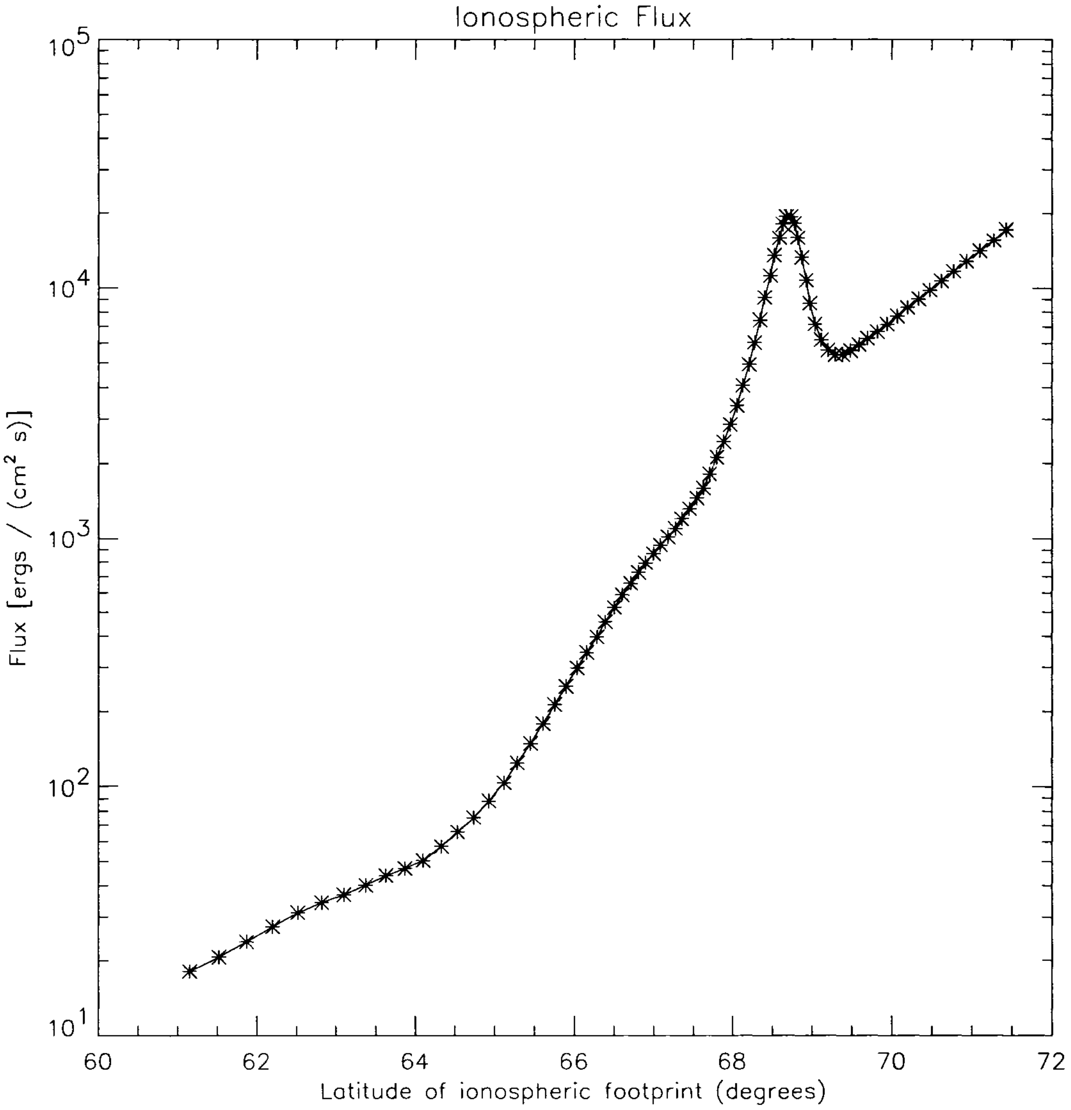

Figure 2.14. Ionospheric energy flux as a function of latitude.

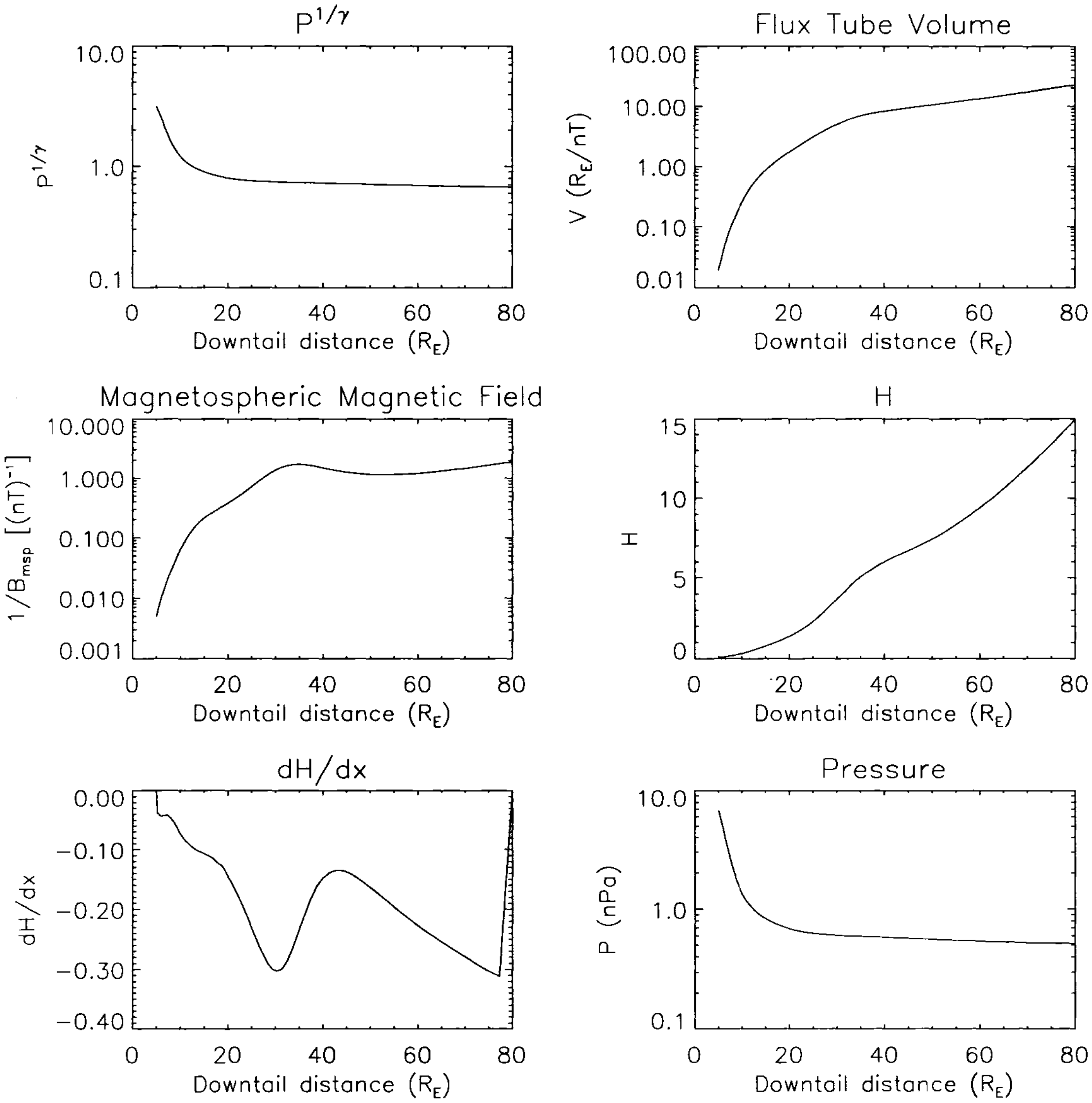

Figure 2.15. Factors in the ionospheric flux. Various quantities involved in the calculation of the calculation of the ionospheric energy flux, given as functions of downtail distance in the midnight meridian plane (y = z = 0). Note that the reciprocal of B_{msp}, instead of that quantity itself, is given in the panel labeled 'Magnetospheric Magnetic Field.'

2.7 Discussion and Summary

This chapter has discussed the construction of a time-independent model designed to examine the plausibility of the mechanism proposed for current sheet thinning in the late growth phase. This model uses the magnetic field provided by the semi-empirical magnetic field model of *Tsyganenko* [1996] (working in conjunction with the associated GEOPACK suite of subroutines) to calculate the specific entropy S on a cylindrical grid (uniform in the azimuthal angle φ, but non-uniform in the radial coordinate ρ). This calculation required the use of a pressure model. Lacking an appropriate pressure model, I developed one based on magnetostatic force balance with the magnetic field provided by *Tsyganenko* [1996].

Profiles of the specific entropy and related quantities along the midnight meridian were calculated to demonstrate how the specific entropy can be used to map the region of magnetopause erosion on the dayside magnetopause to a 'flux reservoir' in the near-Earth magnetotail. The extent of this reservoir was given as roughly $\sim 9R_E$ to $\sim 15R_E$ in the near-Earth magnetotail. Mapping of contour lines in the equatorial plane yielded a location of this 'flux reservoir' somewhere in the vicinity of $\sim 12\,R_E$ in the nightside magnetotail.

A parameter study was conducted to explore the effects of varying the input parameters of this model (the same as the inputs of *Tsyganenko* [1996] upon which it was based) upon the specific entropy. At any fixed location the specific entropy was found to vary by, at most, a factor slightly larger than two for the considered parameter variations.

This analysis has relied upon the assumption that the number of particles on a magnetic flux tube remains constant during convection—or that the departure from this condition can be safely neglected. This assumption is consistent with the constraint on the steady adiabatic convection of magnetic flux tubes from the far magnetotail to the near magnetotail proposed by *Erickson and Wolf* [1980]. I analyzed in detail the energy flux into the ionosphere required to allow steady convection. I found that the ionospheric energy flux that would result from slow, steady adiabatic convection of magnetic flux tubes is inconsistent (by several orders of magnitude) with the energy flux corresponding to auroral observations.

In summary the two central results from this chapter are the following.

- The specific entropy increases by several orders of magnitude from the near-Earth region at about 5 R_E to the mid and far tail at distances larger than 40 R_E. This increase is not significantly altered by any solar wind parameters.

- The amount of energy that must be lost from a flux tube which convects Earthward is far in excess of the energy loss that could be accounted for through energy flux into the ionosphere.

Despite the utility of these models, they are hindered by their time-independent nature. The distribution of specific entropy in the magnetosphere is changed by the convection consistent with the conservation of this quantity. Only the development and use of a self-consistent time-dependent model can model this convection as it develops. The development of such a model is described in the following chapter.

Chapter 3

3D MHD Model—Properties

3.1 Introduction

The results of the study described in the previous chapter give confidence that the suggested mechanism for current sheet thinning indeed provides a plausible explanation for the observed current sheet thinning. I was able to utilize the properties of magnetic flux tubes to draw conclusions regarding the dynamics of the system in three dimensions. However, my earlier study was not self-consistent, in the sense that it used static average properties of the magnetosphere and did not consider dynamical configuration changes such as the evolution of the entropy distribution caused by slow convection.

In order to demonstrate that our mechanism for current sheet thinning can indeed operate, I have developed a self-consistent local MHD model in three dimensions. This model is used to study the effects of a plasma flow which diverges from the near-Earth tail, i.e., from the previously identified 'magnetic flux reservoir' region, toward the dayside magnetopause. I would like to see if this model supports my hypothesis that this flow will lead to the observed formation and thinning of a current sheet in the region of this 'flux reservoir.'

The model has been developed through the coupling of the self-consistent three-dimensional magnetohydrodynamic code of *Otto* [1990] with the semi-empirical magnetic field model of *Tsyganenko* [1996]. The use of the model of *Tsyganenko* [1996] allows the proper treatment of Earth's magnetic field in the near-Earth magnetotail. However, as noted, the Tsyganenko model only provides a magnetic field configuration, and is not an equilibrium model because it does not provide plasma pressure and density in the magnetosphere. To use the Tsyganenko model it is necessary to include plasma pressure and density and to generate an equilibrium which is suitable as an initial configuration for the MHD simulation.

This chapter describes this model. It is worth noting that this model not only provides a suitable initial condition for this simulation but can also be used to study in general the quiet time magnetotail configuration, i.e., field-aligned current distribution, etc. After discussing some basic aspects (namely, the governing equations solved by it, the numerical technique used, the non-uniform grid used in the simulation, and the normalization of quantities used in the model), I will turn to a discussion of the boundary conditions. Once that is done, I will be prepared to consider the generation of an appropriate initial equilibrium state for the simulation. Then I will discuss how boundary conditions simulating plasma outflow from the 'flux reservoir' region of the near-Earth magnetotail are imposed.

3.2 Governing Equations, Normalizations, and Grid

The simulation domain in shown in Figure 3.1. Expressed in terms of geocentric solar magnetospheric (GSM) coordinates, it extends from $-45\ R_E \leq x \leq -5\ R_E$ downtail, $-15\ R_E \leq y \leq +15\ R_E$ in the dawn-to-dusk direction, and $0\ R_E \leq z \leq 12\ R_E$ in the z-direction. Note that the origin of the simulation domain is displaced $5\ R_E$ downtail from Earth's center (the origin of the GSM coordinate system). The equatorial plane of the magnetosphere is defined as $z = 0$.

The model formed through the combination of *Otto* [1990] and *Tsyganenko* [1996] solves the following (normalized) MHD equations:

$$\frac{\partial \rho}{\partial t} = -\nabla \cdot (\rho \mathbf{v}) \tag{3.1}$$

$$\frac{\partial (\rho \mathbf{v})}{\partial t} = -\nabla \cdot \left[\rho \mathbf{v}\mathbf{v} + \left(\frac{1}{2}\right)(p + \mathbf{b}^2)\,\bar{\mathbf{I}} - \mathbf{b}\mathbf{b}\right] \tag{3.2}$$

$$\frac{\partial \mathbf{b}}{\partial t} = \nabla \times (\mathbf{v} \times \mathbf{b} - \eta \mathbf{j}) \tag{3.3}$$

$$\frac{\partial h}{\partial t} = -\nabla \cdot (h\mathbf{v}) + \left\{\left[\frac{(\gamma - 1)}{\gamma}\right] h^{1-\gamma}\, \eta \mathbf{j}^2\right\} \tag{3.4}$$

$$\mathbf{j} = \nabla \times \mathbf{b} \tag{3.5}$$

with

$$h = \left(\frac{p}{2}\right)^{\frac{1}{\gamma}}, \tag{3.6}$$

and where $\bar{\mathbf{I}}$ is the identity tensor. The variables ρ, p, $\mathbf{v}$, $\mathbf{b}$, $\mathbf{j}$, and η represent the (normalized) mass density, thermal pressure, plasma velocity, magnetic field, current density, and resistivity, respectively. The ratio of specific heats γ, sometimes called the adiabatic

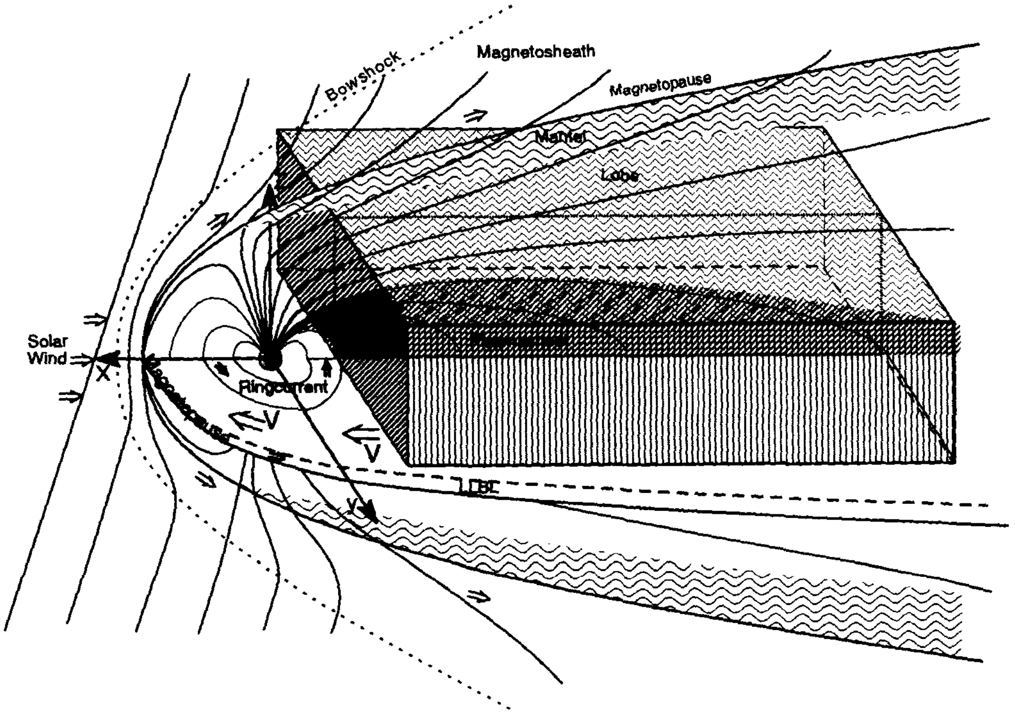
Bowshock
Magnetosheath
Magnetopause
Mantel
Lobe
Solar Wind
X
Ringcurrent
Magnetopause
V
V
V
LLBL

Figure 3.1. Domain of the simulation. The figure is not to scale. The domain of the simulation is shown in purple. Note the displacement of the origin of the coordinate system used in the simulation from the origin of the GSM coordinate system by the distance $r_{min} = 5\ R_E$ along the x-axis.

Quantity	Normalized value
Length	1 R_E (6378 km)
Number density	1 cm^{-3}
Mass density	1.67 $\times 10^{-24}$ g/cm^3
Magnetic field	20 nT
Plasma velocity	437 km/s
Time	14.6 s
Pressure	0.159 nPa

Table 3.1. Normalized values of simulation quantities

or polytropic index, is chosen to be $\frac{5}{3}$ (appropriate for an isotropic plasma with three degrees of freedom). Since this study is being performed within the realm of ideal MHD, the resistivity η is set identically equal to zero.

The quantities in the equations above are dimensionless, having been normalized to 'typical' or 'characteristic' values. Length scales in the model are normalized to the distance $L_0 = 1\,R_E$ (6378 km). Number densities are normalized to $n_0 = 1\,cm^{-3}$. The characteristic mass density ρ_0 is given by $\rho_0 = m_0 n_0$, where m_0 is the characteristic mass of a constituent ion. For my purposes, m_0 is equal to the proton mass, as is appropriate for a predominantly hydrogen plasma. Magnetic fields are normalized to $b_0 = 20.0$ nT, the typical lobe magnetic field. Plasma velocities are normalized to the Alfvén speed $v_A = \frac{b_0}{\sqrt{\mu_0 \rho_0}}$. Time is expressed in units of the Alfvén time $t_A = \frac{L_0}{v_A}$. Pressures are normalized to the magnetic pressure $\frac{b_0^2}{2\mu_0}$. With the values given above, I find (again, for a predominantly hydrogen plasma) that the typical Alfvén speed v_A has the value of 437 km/s, while the characteristic Alfvén time t_A is 14.6 s. The pressure is normalized to 0.159 nPa. These normalizations are summarized in Table 3.1.

3.3 Numerical Solution of the Governing Equations

The governing equations are solved using the leapfrog scheme, an explicit finite differences method that is accurate to second order in both space and time [e.g., *Fletcher* [1991], *Potter* [1973]], i.e., the error is proportional to $(\Delta x)^2$. To start my discussion of this numerical

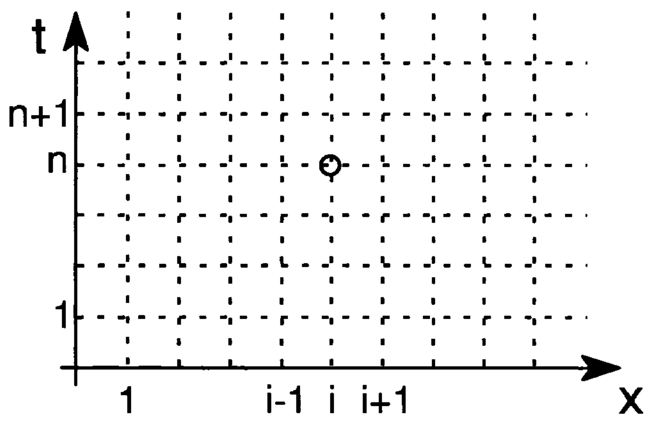

Figure 3.2. Uniform grid in one spatial dimension and time. A uniform numerical grid in one spatial dimension (x) and time (t). The index i indicates the position in space, whereas the index n indicates the 'position' in time. The grid spacing in x is Δx; the grid spacing in time is Δt. Note that Δt is sometimes called the 'time step.' The grid point (i,n) is indicated by a circle.

scheme, I will begin by considering a continuous scalar quantity $f(x,t)$ that is defined in one space dimension (namely, x) and time t. Let us define it on a uniform discrete grid such as that depicted in Figure 3.2. I shall adopt the convention scheme of *Fletcher* [1991]. Accordingly, the value of f at the position $x = x_i$ at the time $t = t_n$ is denoted by

$$f_i^n = f(x_i, t_n). \tag{3.7}$$

Returning to the governing equations (Equations 3.1 through 3.5), one sees that he must concern himself with first partial derivatives of various quantities in space and time. The central difference approximation of the first partial derivative of f with respect to position x, evaluated at position $x = x_i$ and time $t = t_n$, is given by

$$\left.\frac{\partial f}{\partial x}\right|_i^n = \frac{\left(f_{i+1}^n - f_{i-1}^n\right)}{2\Delta x}. \tag{3.8}$$

Similarly, the central difference approximation of the first partial derivative of f with respect to time t, evaluated at position $x = x_i$ and time $t = t_n$, is given by

$$\left.\frac{\partial f}{\partial t}\right|_i^n = \frac{\left(f_i^{n+1} - f_i^{n-1}\right)}{2\Delta t}. \tag{3.9}$$

I now consider applying these expressions to the continuity equation (Equation 3.1); for the sake of simplicity, I restrict my considerations to one dimension. Then I have

$$\frac{\partial \rho}{\partial t} = -\frac{\partial}{\partial x}\left(\rho v\right). \tag{3.10}$$

For the sake of later notational simplicity, I will introduce the mass flux

$$s = \rho v. \tag{3.11}$$

Then I can write Equation 3.10 as

$$\frac{\partial \rho}{\partial t} = -\frac{\partial s}{\partial x}. \tag{3.12}$$

Discretizing the partial derivatives in Equation 3.12 in the manner illustrated in Equations 3.8 and 3.9, I obtain

$$\frac{\left(\rho_i^{n+1} - \rho_i^{n-1}\right)}{2\Delta t} = -\frac{\left(s_{i+1}^n - s_{i-1}^n\right)}{2\Delta x}. \tag{3.13}$$

I can solve this expression for ρ_i^{n+1}, the mass density at the next time step. Doing so, I obtain the result

$$\rho_i^{n+1} = \rho_i^{n-1} - \left(\frac{\Delta t}{\Delta x}\right)\left(s_{i+1}^n - s_{i-1}^n\right). \tag{3.14}$$

One sees that the advancement of ρ at a particular position ($x = x_i$)—that is, its solution at successive time steps—requires knowledge of its value at that position at the previous time step ($t = t_{n-1}$), as well as knowledge of the mass flux s at the neighboring spatial points ($x = x_{i-1}$ and $x = x_{i+1}$) at the current time ($t = t_n$). This dependence is illustrated in Figure 3.3.

Since the leapfrog scheme requires knowledge of quantities at the previous time step, another numerical scheme must be used to advance the governing equations to the first time step (that is, to solve these equations and obtain the values of all quantities at time $t = \Delta t$). I use the Lax scheme to initialize the integration. The central difference approximation of first partial derivatives with respect to time (in the manner of Equation 3.9 are replaced by the forward difference approximation, which has the form

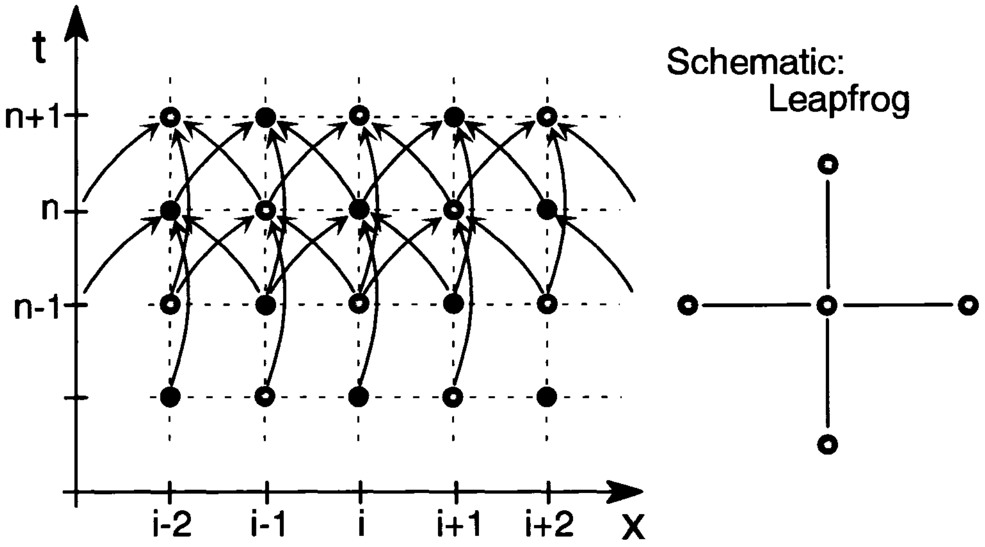

Figure 3.3. Leapfrog scheme in one spatial dimension. An illustration of the solution (Equation 3.14) of the one-dimensional mass continuity equation (Equation 3.1) for the mass density ρ at successive times through use of the leapfrog scheme. Note the dependence of the solution ρ_i^{n+1} at time $t = t_{n+1}$ on the mass density ρ_i^{n-1} at the previous time step $(t = t_{n-1})$ and the same spatial grid index (i), as well as its dependence on the mass fluxes s_{i+1}^n and s_{i-1}^n at the same time step $(t = t_n)$ but neighboring spatial grid indices. Quantities at the indices (i,n) are not used in the solution; they are 'leapt over.' Also note that the solution proceeds on separate 'sub-grids' (depicted here in red and purple).

$$\left.\frac{\partial f}{\partial t}\right|_i^1 = \frac{(f_i^1 - f_i^0)}{\Delta t}. \tag{3.15}$$

The central difference approximation is still used for the spatial partial derivatives. The mass continuity equation in one dimension now assumes the form

$$\frac{(\rho_i^1 - \rho_i^0)}{\Delta t} = -\frac{(s_{i+1}^0 - s_{i-1}^0)}{2\Delta x}. \tag{3.16}$$

Solving this expression for ρ_i^1, I obtain

$$\rho_i^1 = \rho_i^0 - \left(\frac{\Delta t}{2\Delta x}\right)\left(s_{i+1}^0 - s_{i-1}^0\right). \tag{3.17}$$

Note that this solution depends only on quantities at the initial time step $(t = t_0)$. The Lax step is also used to complete the solution of the governing equations on the grid at the end of a simulation run and every time a full output of all data is generated.

In extending the leapfrog scheme to two and three dimensions, one must take care to ensure that the neighboring grid points used to update a particular variable (such as the mass density) all correspond to the current time step. Circumventing the use of already-updated grid points results in the update of grid points in the leapfrog pattern that gives the scheme its name.

It should be noted that, strictly, the leapfrog method has no numerical diffusion, but suffers like other methods from numerical dispersion. Particularly, in the presence of strong gradients this can lead to strong grid oscillations. If and where these occur a small viscous or diffusive term is added to avoid this problem.

3.4 Boundary Conditions

The selection of boundary conditions for the simulation is an important, and often challenging, part of the specification of the problem to be solved. This selection is dictated by the character of the system under study. A proper mathematical formulation of the boundary conditions requires the solution of the characteristics of MHD in three dimensions. Note that the ideal MHD equations are hyperbolic and have only real characteristics. While possible in principle, the solution of the boundary problem has not been solved in three-dimensional MHD. Resistive terms contribute an additional challenge. For practical purposes, boundary conditions either employ well-defined symmetries or are good "guesses" of the real conditions using physical intuition and experimentation.

The boundaries in this simulation can be divided into three categories, based on the manner in which the boundary conditions are determined at the boundary in question:

- the equatorial plane ($z = z_{min} = 0$), at which the boundary conditions are determined by making use of the symmetry of the northern and southern lobes of the tail;
- the boundaries at x_{min}, y_{min}, y_{max}, and z_{max}, at which the physical behavior of the system variables and consideration of earlier studies is used to determine the boundary conditions; and
- the Earthward boundary at x_{max}, at which physical consideration and a fair deal of experimentation are used to determine the boundary conditions.

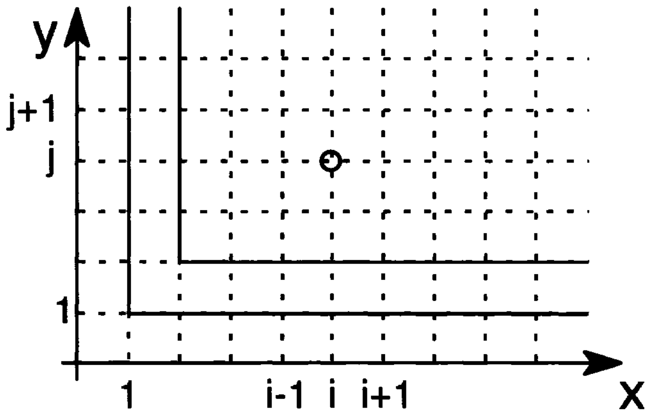

Figure 3.4. Physical and mathematical boundaries of the grid. A depiction of a two-dimensional grid in x and y. The indices corresponding to x and y are i and j, respectively. The portion of the mathematical boundary corresponding to the grid indices at $i = 1$ and $j = 1$ is shown in red. The portion of the physical boundary corresponding to the grid indices $i = 2$ and $j = 2$ is shown in green.

Boundary conditions are applied to all MHD variables (such as the mass density, velocity, and magnetic field) after every time step (that is, after all field quantities have been advanced). Since the evaluation of first order spatial derivatives in the leapfrog scheme requires values at surrounding grid points, the grids in x, y, and z contain 'mathematical boundary points' that are used for the implementation of the boundary conditions, usually by prescribing appropriate derivative conditions. This arrangement is illustrated for a two-dimensional (x,y) grid in Figure 3.4.

3.4.1 Boundary Conditions Applicable to All Boundaries

Before attending to the differences between the boundary conditions applied at different boundaries, I should first take a moment to consider the boundary conditions common to all boundaries. The mass density ρ and the pressure analogue h (and therefore the pressure p) are symmetric across all boundaries. The vanishing divergence of $\mathbf{b}$ (that is, the condition $\nabla \cdot \mathbf{b} = 0$) is explicitly maintained at all boundaries except for the equatorial plane (where its application could break the symmetry across that boundary) and where the symmetry includes $\nabla \cdot \mathbf{b} = 0$ as an initial condition.

3.4.2 The Equatorial Plane ($z = z_{min} = 0$)

Some physical systems, such as the magnetosphere, possess certain symmetries that make the selection of the boundary conditions across certain planes of symmetry somewhat easier. The half of the system on one side of a symmetry plane is mirrored across that plane. If a quantity is symmetric across that plane, it has the same value on both sides of the symmetry plane. For instance, if the mass density ρ is symmetric across the plane $z = 0$, then $\rho(x, y, z) = \rho(x, y, -z)$. If, on the other hand, that quantity is anti-symmetric across that symmetry plane, then its value on one side of the symmetry plane is the negative of its value on the other side; this also implies that the quantity is zero on the boundary. [If the mass density ρ is anti-symmetric across the plane $z = 0$, then $\rho(x, y, z) = -\rho(x, y, -z)$.]

In the case of the magnetosphere, two sets of symmetries present themselves. When IMF $B_y = 0$ and there is no dipole tilt, the magnetotail is symmetric across the noon-midnight meridian ($y = 0$). I utilize the symmetry of the magnetotail about the equatorial plane ($z = 0$). The northern and southern lobes of the magnetotail are symmetric. This symmetry across the equatorial plane allows us to reduce our computational effort by half, since I can model just the northern portion ($0 \leq z \leq z_{max}$) of the magnetosphere and use symmetry to extend those results to the southern region ($-z_{max} \leq z \leq 0$). Furthermore, this symmetry—which is associated with the magnetotail current (separating the northern and southern lobes of the magnetotail) that serves as the source of the magnetic field in the lobes—remains robust enough for me to use it for my purposes in determining the boundary conditions across the equatorial plane.

Let us consider the implications of that symmetry for the components of **b** and **v**. Before proceeding, I should attend to some matters of terminology. I can write the magnetic field as

$$\mathbf{b} = b_x \mathbf{e}_x + b_y \mathbf{e}_y + b_z \mathbf{e}_z. \tag{3.18}$$

The quantities b_x, b_y, and b_z are the components of the magnetic field in the x, y, and z directions, respectively. Those directions are given by the unit vectors $\mathbf{e}_x$, $\mathbf{e}_y$, and $\mathbf{e}_z$, respectively. Similar notation can be applied to **v** and its components.

If one follows a closed magnetic field line (that is, one anchored at both ends in the ionosphere) from the southern lobe of the magnetotail to the northern lobe of the magnetotail (or vice versa), he finds that b_x and b_y change sign across the equatorial plane. This reversal is illustrated in Figure 3.5. These components (tangential to the equatorial plane) of the magnetic field are anti-symmetric across the equatorial plane. That is, $b_x(x, y, z) = -b_x(x, y, -z)$ and $b_y(x, y, z) = -b_y(x, y, -z)$. On the other hand, the component of the magnetic field normal to the equatorial plane (namely, b_z) is symmetric across that plane. That is, $b_z(x, y, z) = b_z(x, y, -z)$.

Considering the plasma flow, one can argue that the tangential components of the plasma velocity (v_x and v_y) must be symmetric so that the portions of a magnetic flux tube immediately above (northward) and below (southward) of the equatorial plane move with one another. That is, $v_x(x, y, z) = v_x(x, y, -z)$ and $v_y(x, y, z) = v_y(x, y, -z)$. On the other hand, any motion of that field line perpendicular to the equatorial plane would destroy the symmetry of the system; and so the normal component of the plasma velocity (v_z) must be zero in the equatorial plane, and anti-symmetric across that plane. That is, $v_z(x, y, 0) = 0$ and $v_z(x, y, z) = -v_z(x, y, -z)$.

3.4.3 The Earthward Boundary at $x = x_{max}$

The Earthward boundary at $x = x_{max}$ is special in that it lies in the near-Earth region, wherein the magnetic field is making the transition from a dipole to a magnetotail configuration. The special nature of this boundary is not as evident during the relaxation of the system to an equilibrium (discussed in the next section). The Earthward boundary is subject to the same boundary conditions as those applied at $x = x_{min}$, $y = y_{min}$, $y = y_{max}$, and $z = z_{max}$ during the relaxation. The Earthward boundary plays a critical role in the later portion of the research, when a special outflow boundary condition is imposed on this boundary to simulate the depletion of the near-Earth 'flux reservoir.' This boundary condition is discussed in more detail in Section 4.1, because the applied outflow leads to the associated current dynamics. Here I discuss only the boundary conditions as applied to the relaxation to the initial equilibrium configuration.

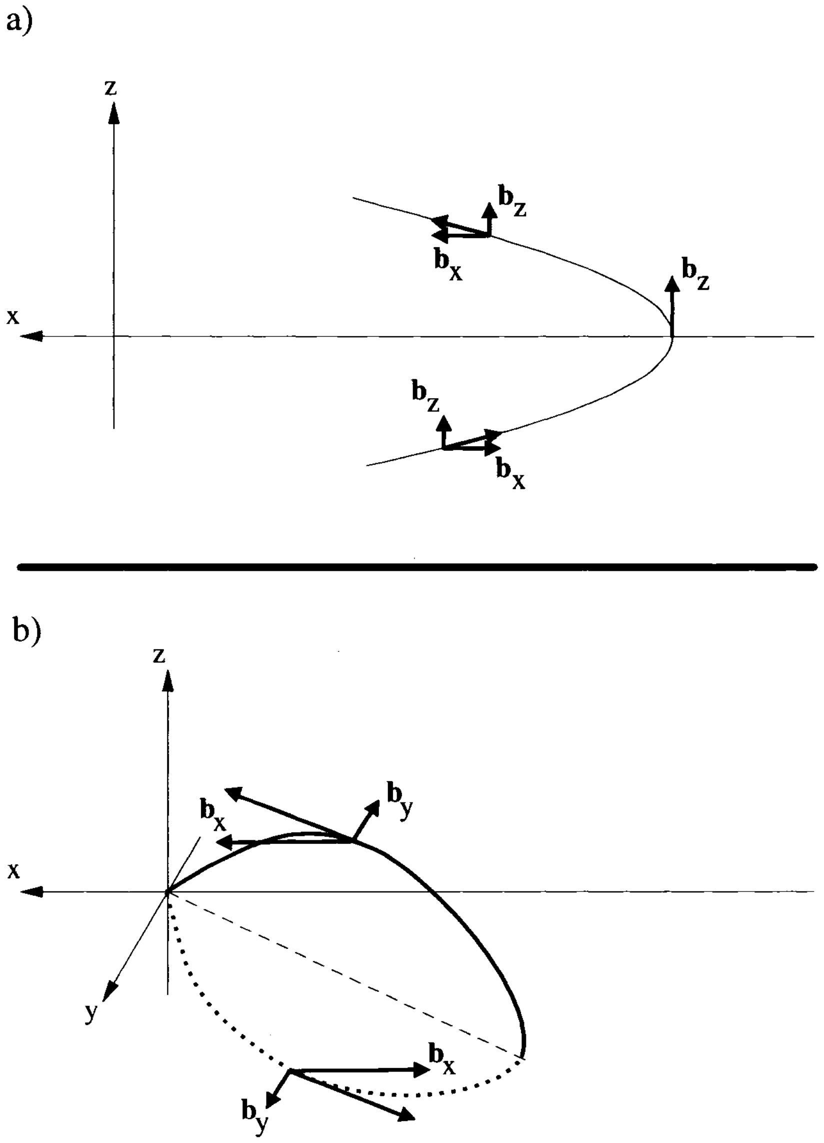

Figure 3.5. Illustrations of symmetries and anti-symmetries across the equatorial plane. a) Two dimensional sketch of a portion of a magnetotail magnetic field line lying in the noon-midnight meridian (x,z) plane. The magnetic field is decomposed into its x and z components at three points along the magnetic field. Note that the x-component b_x changes sign as one passes from below ($z < 0$) to above ($z > 0$) the equatorial plane ($z = 0$). b) Perspective sketch of a magnetic field line lying out of the noon-midnight meridian plane. The magnetic field is decomposed into its x and y components at two points along the magnetic field line. Note that both the x-component b_x and the y-component b_y changes direction as one passes from below ($z < 0$) to above ($z > 0$) the equatorial plane ($z = 0$).

3.4.4 The Boundaries at $x = x_{min}$, $y = y_{min}$, $y = y_{max}$, and $z = z_{max}$

The boundaries at $x = x_{min}$, $y = y_{min}$, $y = y_{max}$, and $z = z_{max}$ are chosen so that the system lies within the magnetopause, so that the additional challenges of modeling that boundary are avoided. Note that the same physics could be modeled with a global simulation, i.e., one which contains the entire magnetosphere embedded in the solar wind. However, such a model is not able to provide the required high resolution needed to model the dynamics of current sheet thinning appropriately. Determination of the appropriate boundary conditions to apply at these boundaries (again, at $x = x_{min}$, $y = y_{min}$, $y = y_{max}$, and $z = z_{max}$) requires some degree of experimentation and input from earlier numerical studies of relevance (e.g., *Otto* [1990], *Hesse and Birn* [1993]). A summary of the actual applied boundary conditions is presented in Table 3.2. The normal component of the plasma velocity $\mathbf{v}$ is set equal to zero at these remaining boundaries. The tangential components of $\mathbf{v}$ are symmetric across the boundaries at $x = x_{min}$, $y = y_{min}$, and $y = y_{max}$. On the other hand, the tangential component of $\mathbf{v}$ at $z = z_{max}$ is anti-symmetric across that boundary. As explained in Section 3.4.1, the mass density ρ and thermal pressure p are both symmetric across all these boundaries. The tangential components of the magnetic field at these boundaries are symmetric. The maintenance of the divergence-free condition on $\mathbf{b}$ (that is, $\nabla \cdot \mathbf{b} = 0$) on these boundaries determines the behavior of the normal component of the magnetic field across them.

3.5 Relaxation of the Initial Configuration to an Equilibrium State

The combination of the 3D MHD code of *Otto* [1990] with the semi-empirical magnetic field model of *Tsyganenko* [1996] allows me to establish an initial magnetic field configuration that properly includes the influence of Earth's strong dipolar magnetic field in the near-Earth magnetotail. However, this initial configuration is not in force balance (that is, the net force density is not zero everywhere in the system). The *Tsyganenko* [1996] model is only a magnetic field model; it does not incorporate plasma pressure and density. Hence force balance is not relevant to the *Tsyganenko* [1996] model.

In order to generate an acceptable equilibrium configuration, I must first introduce plasma pressure and density, and then allow the resulting system to relax to an equilibrium state from which I can start the plasma outflow. For a study such as this, it is absolutely

	x_{min}	x_{max}	y_{min}, y_{max}	z_{min}	z_{max}
ρ	Symm.	Symm.	Symm.	Symm.	Symm.
v_x	0	Special	0	Symm.	0
v_y	0	Special	0	Symm.	0
v_z	0	Special	0	Anti-symm.	0
b_x	$\nabla \cdot \mathbf{b} = 0$	$\nabla \cdot \mathbf{b} = 0$	Symm.	Anti-symm.	Symm.
b_y	Symm.	Symm.	$\nabla \cdot \mathbf{b} = 0$	Anti-symm.	Symm.
b_z	Symm.	Symm.	Symm.	Symm.	$\nabla \cdot \mathbf{b} = 0$
p	Symm.	Symm.	Symm.	Symm.	Symm.

Table 3.2. Summary of boundary conditions on the velocity and magnetic field used in the simulation. Magnetic field components identified with the entry $\nabla \cdot \mathbf{b} = 0$ are determined through use of the divergence-free condition on the magnetic field on that boundary. Variables denoted by the designation "Symm." are symmetric across the boundary in question, whereas those denoted by the designation "Anti-symm." are anti-symmetric across the boundary in question. The entries "Special" pertain to the velocity boundary conditions at x_{max}. During the ballistic relaxation, $v_x = v_y = v_z = 0$. Once the initial equilibrium configuration has been established, these velocity components are specified in the manner discussed in Section 4.1.

crucial to start with an equilibrium state; otherwise the effects of the plasma outflow cannot be distinguished from the dynamics resulting from a non-equilibrium configuration. Note also that the magnetosphere is very close to equilibrium during quiet times such as the growth phase.

As suggested in Chapter 1, many authors have addressed issues concerning equilibrium configurations of the magnetosphere (e.g., *Chodura and Schlüter* [1981], *Voigt and Wolf* [1988], *Hesse and Birn* [1993], *Lee et al.* [1995], *Voigt* [1996], *Lemon et al.* [2003]). My approach is based on the 'ballistic relaxation' described by *Hesse and Birn* [1993]. Over the course of a run establishing an equilibrium state (referred henceforth as an "equilibrium run"), the system is subjected to several intervals (in time) during which this relaxation is applied.

During such a relaxation interval, the system first evolves freely, thereby relaxing unbalanced forces (and converting magnetic energies into kinetic energy). At the end of each such interval the plasma velocity is set equal to zero everywhere in the simulation domain. This results in the removal of the plasma kinetic energy throughout the domain and a successive relaxation of unbalanced forces. This technique is strictly a computational tool designed to evolve the system toward an equilibrium.

A specific example might serve to better illustrate the relaxation process. Table 3.3 displays the parameters (namely, the starting time step N_a and the period τ_r for each relaxation interval) pertaining to the relaxation for a particularly successful 'equilibrium run.' The time step Δt was equal to 0.01 t_A during this run. The ballistic relaxation technique is first applied (that is, the plasma velocity is set to zero everywhere in the simulation domain) at time $t = 2\ t_A$. It is applied again at times $t = 3\ t_A$ and $t = 4\ t_A$. The interval from $t = 2\ t_A$ to $t = 4\ t_A$ constitute the first 'relaxation interval.' This first relaxation interval is followed immediately by another relaxation interval (starting at $t = 4\ t_A$), during which ballistic relaxation is applied every $\tau_r = 2\ t_A$. That is, the ballistic relaxation is applied at times $t = 4\ t_A$, $t = 6\ t_A$, and $t = 8\ t_A$. The time from $t = 4\ t_A$ to $t = 8\ t_A$ constitutes the second relaxation interval. During the third relaxation interval, starting at $t = 8\ t_A$, the ballistic relaxation is applied every $\tau_r = 4\ t_A$, up until $t = 40\ t_A$.

Table 3.3 illustrates that I change the period τ_r for setting the velocity to zero from each relaxation interval to the next. This is motivated by the following considerations. The

Starting time of relaxation interval t_A	Period τ_r of relaxation (t_A)
2	1
4	2
8	4
40	0.4
44	4
72	0.4
76	8
96	0.4
100	4

Table 3.3. Relaxation parameters for a sample 'equilibrium run.' The time step during this run was $\Delta t = 0.01\ t_A$. Ballistic relaxation was discontinued at $t = 120\ t_A$.

system has unbalanced forces on small and large scales. Carrying out the relaxation with relatively short relaxation periods will help to remove small-scale forces. However, running the relaxation only with small relaxation periods would lead to a very long relaxation time scale for the removal of large-scale forces. This process is accelerated by using longer relaxation periods. The system undergoes relaxation intervals with alternately frequent and infrequent applications of the ballistic relaxation until it is decided that the system has relaxed to a sufficient extent. But how is that decided?

It is useful to have a quantitative measure in order to follow the approach of the system to equilibrium. Following the convention of *Hesse and Birn* [1993], I define the 'force norm' as

$$N = \int_{\mathcal{V}} (-\nabla p + \mathbf{j} \times \mathbf{b})^2 \, d\mathcal{V}. \tag{3.19}$$

This quantity is a measure of the unbalanced forces throughout the system. The volume integral is evaluated throughout the total system volume $\mathcal{V}$. Figure 3.6 illustrates the value of the force norm through the course of an 'equilibrium run.' The force norm is seen to decrease by four orders of magnitude during the run. Although the length of an equilibrium run can be arbitrarily long (leading to arbitrarily small values of the force norm, limited only by numerical errors), practical considerations led me to consider this reduction of the

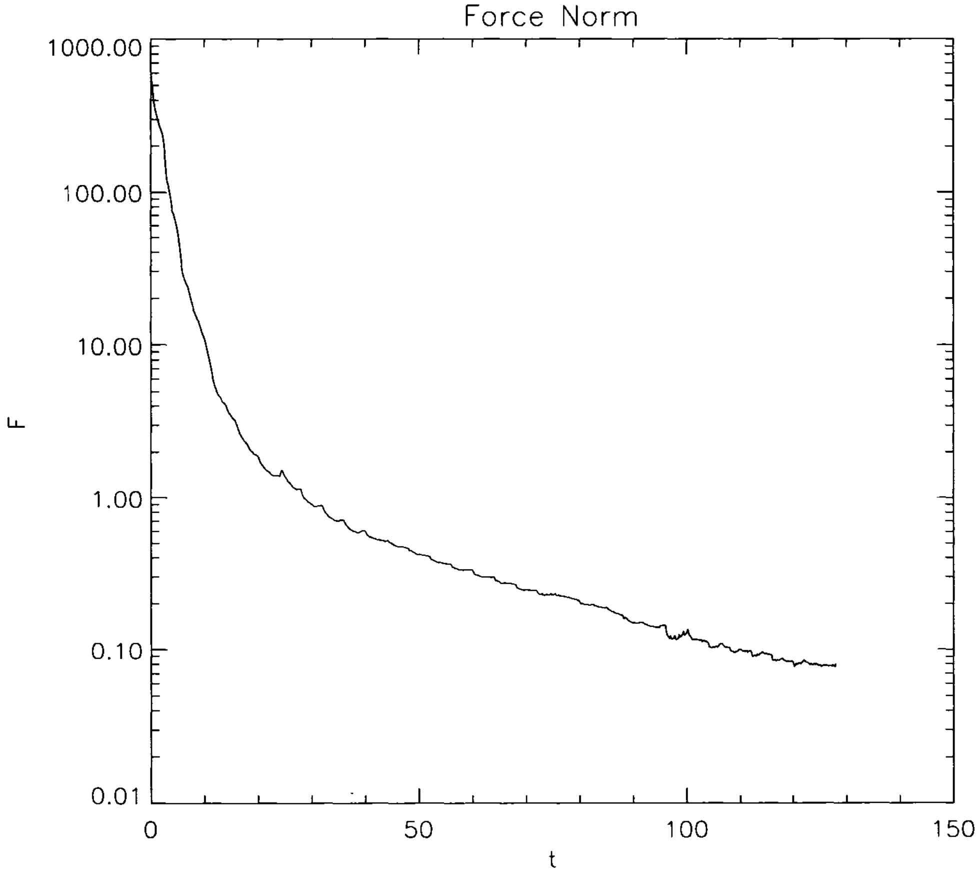

Figure 3.6. Force norm. The force norm throughout an equilibrium run. The horizontal axis is the time in units of the Alfvén time (t_A). The vertical axis is the (normalized) force norm.

force norm to be sufficient for my purposes.

As a second measure the maximum magnitude of the plasma velocity throughout the system is also used to monitor the the approach of the system to an equilibrium state. Figure 3.7 shows the plot of this quantity corresponding to the system used in Figure 3.6. The application of the ballistic relaxation—periodically setting the plasma velocity to zero everywhere in the system—is explicitly demonstrated in this figure.

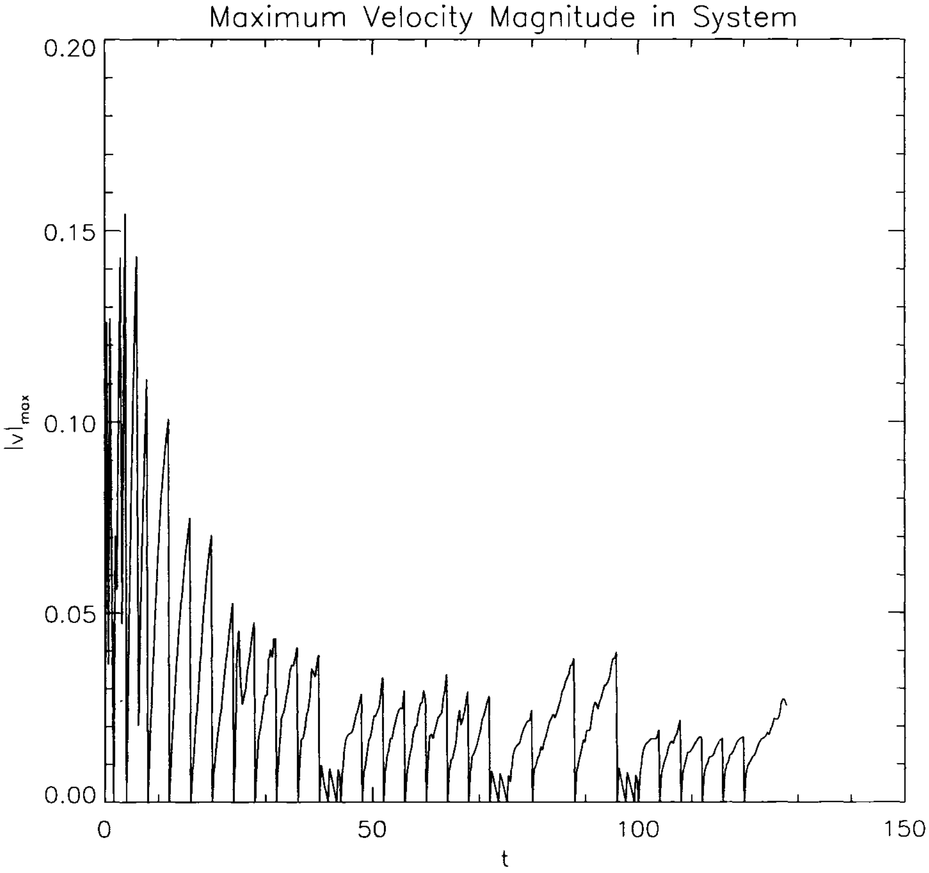

Figure 3.7. Maximum velocity magnitude. The maximum magnitude of the plasma velocity throughout an equilibrium run. The horizontal axis is the time in units of the Alfvén time (t_A). The vertical axis is the (normalized) velocity magnitude. Note that this run is the same as that for which the force norm is displayed in Figure 3.6.

3.6 Description of the Initial Equilibrium State

We will find it helpful to acquaint ourselves with the initial equilibrium state before considering the evolution of the system under the plasma outflow boundary conditions (discussed in Section 4.1). Doing so will also allow us the opportunity to compare this initial equilibrium state with the decidedly non-equilibrium state of the system at the start of the ballistic relaxation.

I will begin by considering the magnetic field at the Earthward boundary. Figure 3.8 shows this quantity at the beginning of the relaxation, while Figure 3.9 shows it at the end

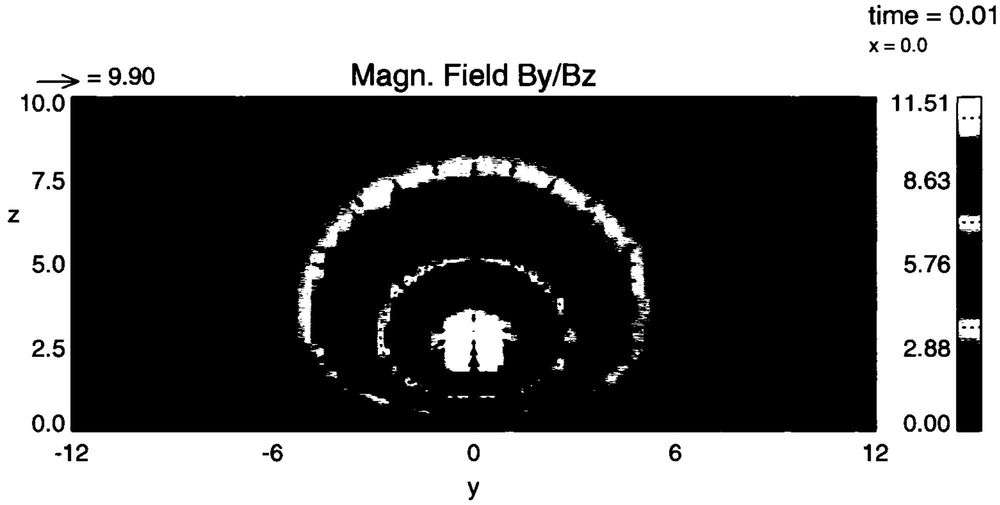

Figure 3.8. Non-equilibrium magnetic field at the Earthward boundary. The magnetic field at the Earthward boundary ($x = x_{max} = 0$) at $t = 0.01\ t_A$, shortly after the beginning of the relaxation. Arrows show the direction of the tangential magnetic field $\mathbf{b}_t = b_y\mathbf{e}_y + b_z\mathbf{e}_z$, while colors give the value of the normal magnetic field component b_x.

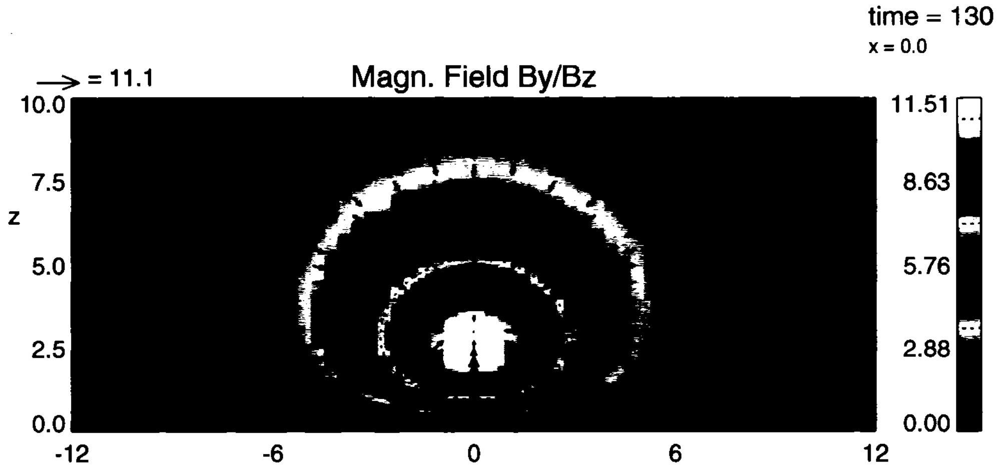

Figure 3.9. Equilibrium magnetic field at the Earthward boundary. The magnetic field at the Earthward boundary ($x = x_{max}$) at $t = 130\ t_A$, at the end of the relaxation. The same convention used in Figure 3.8 is used here.

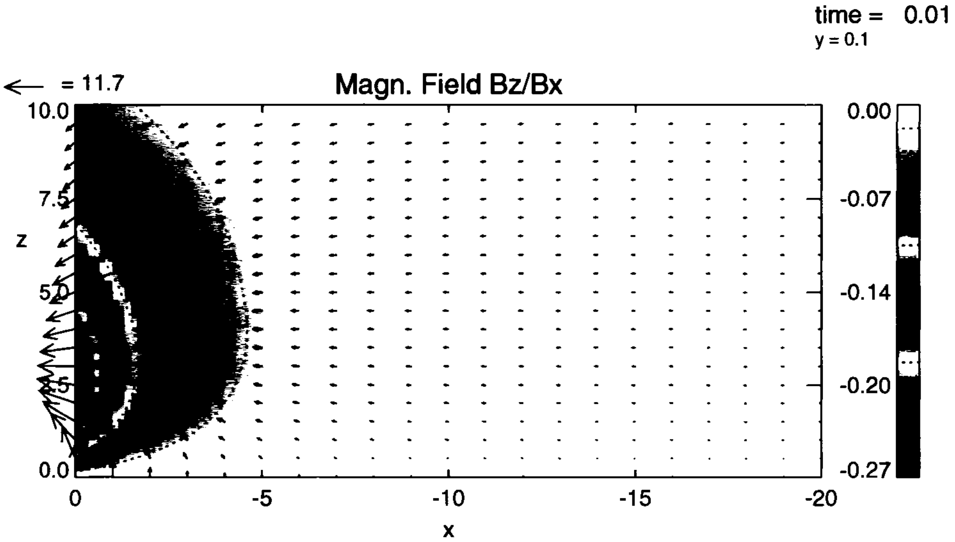

Figure 3.10. Non-equilibrium magnetic field near the noon-midnight meridian. The magnetic field in the plane $y = 0.1$ at $t = 0.01\ t_A$, very early in the relaxation. Arrows show the direction of the tangential magnetic field $\mathbf{b}_t = b_x\mathbf{e}_x + b_z\mathbf{e}_z$, while colors give the value of the normal magnetic field component b_y.

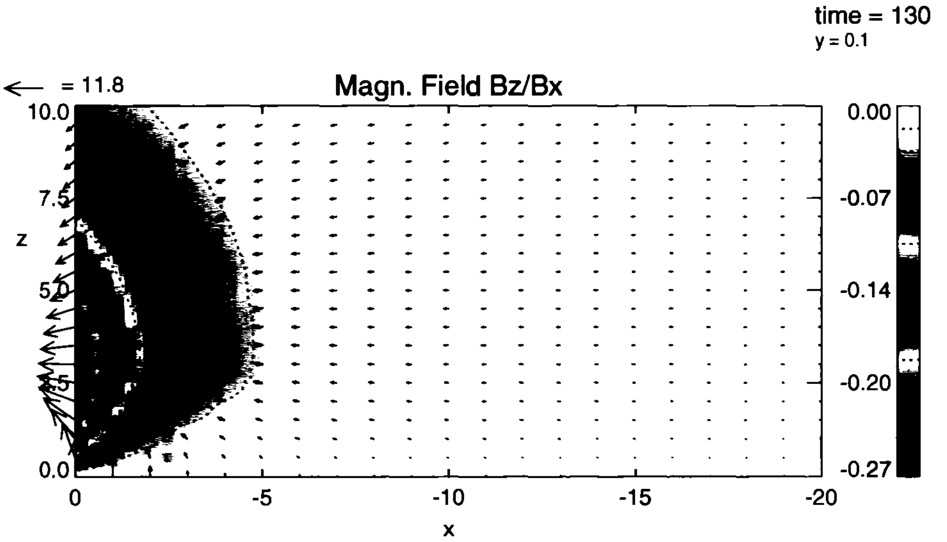

Figure 3.11. Equilibrium magnetic field near the noon-midnight meridian. The magnetic field in the plane $y = 0.1$ at $t = 130\ t_A$, at the end of the relaxation. The same convention used in Figure 3.10 is used here.

of the relaxation. The magnetic field at this boundary does not change appreciably in the course of the relaxation from the T96 configuration used for its initialization. This point is also illustrated in Figure 3.10, which shows the magnetic field in the plane $y = 0.1$ at $t = 0.01$, and Figure 3.11, which shows the corresponding plot at the end of the relaxation.

Now let us turn to the density and pressure in the noon-midnight meridian ($y = 0$) at two different times—at the beginning of the relaxation (at time $t = 0.01\ t_A$ and at the end of the relaxation (at time $t = 130\ t_A$). These profiles are shown in Figure 3.12 and Figure 3.13. One sees that the density decreases in the lobes as the relaxation proceeds. At the end of the relaxation, the high-density and high-pressure regions are confined to the vicinity of the equatorial plane, in the region that is identified as the plasma sheet. The maximum and minimum values of both the density and pressure decrease by the end of the relaxation.

Next let us consider the current density in the noon-midnight meridian ($y = 0$). These profiles are shown in Figure 3.14 and Figure 3.15. We see that the region of appreciable current density (with values denoted by reds and yellows in the figure) has greater extent at the end of the relaxation. At $t = 0.01\ t_A$, this tailward extent of this region is roughly $-8 < z < -3$, whereas its extent in z is roughly $0 < z < 1.8$. The corresponding ranges of values at time $t = 130\ t_A$ are $-12 < x < -2.8$ and $0 < z < 2.5$. Over the course of the relaxation the maximum magnitude of the current density decreased from 1.39 to 0.90—a decrease of slightly over 35%. The current density profile at the end of the relaxation (Figure 3.15) assumes a profile that is similar to those of the density and pressure at that time (Figure 3.13).

Figure 3.16 and Figure 3.17 show the current density at the Earthward boundary near the beginning ($t = 0.01$) and at the end ($t = 129$), respectively, of the relaxation. The regions of strong current extend to larger values of z at the end of the relaxation than they had at the beginning. This change is more prominent for larger values of $|y|$. Figure 3.18 shows the current density in the plane $x = -5.2$, near the maximum in the current density show in Figure 3.15. The closure of the current density is shown in the equatorial plane in Figure 3.19.

Let us focus for a short while on the field-aligned currents at the Earthward boundary. We see that the field-aligned current structure at the Earthward boundary ($x = x_{max}$)

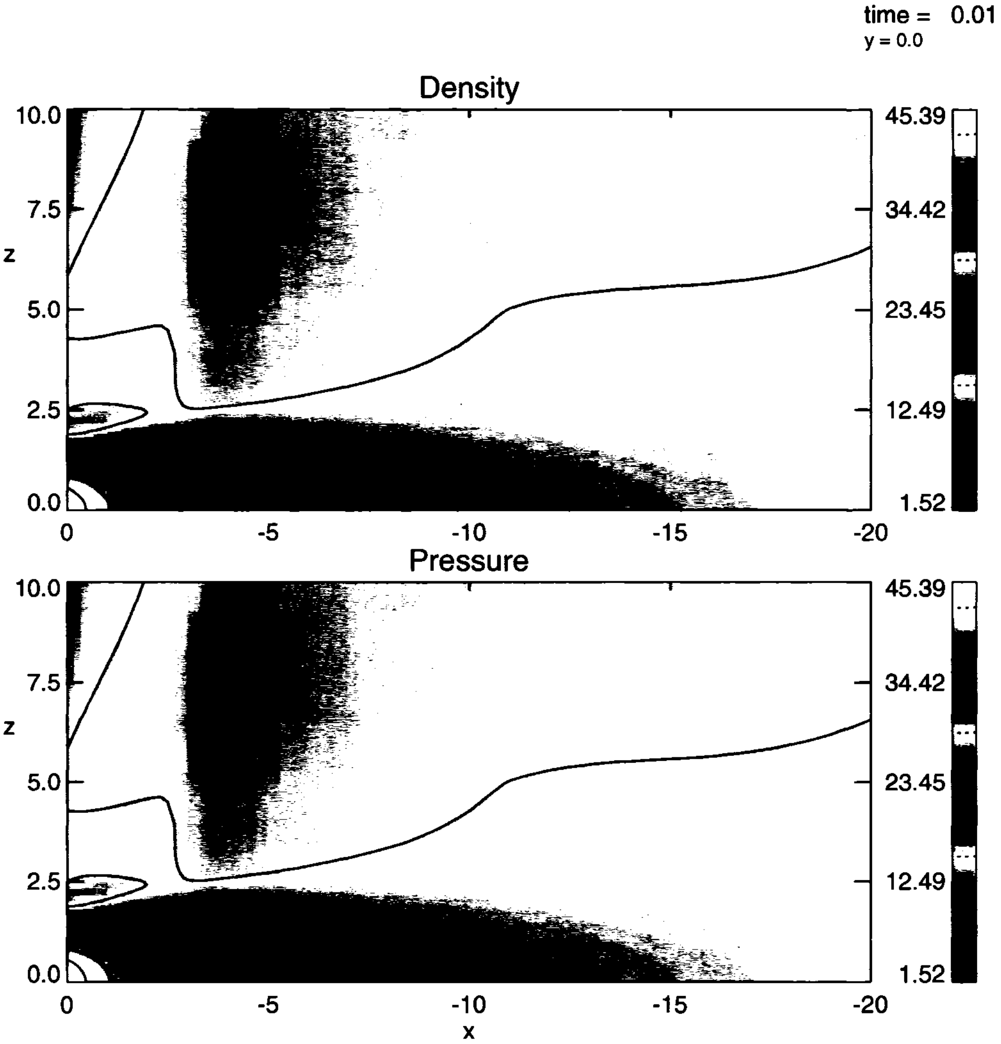

Figure 3.12. Non-equilibrium density and pressure in the noon-midnight meridian. The density and pressure in the noon-midnight meridian ($y = 0$) at $t = 0.01\ t_A$, at the beginning of the relaxation.

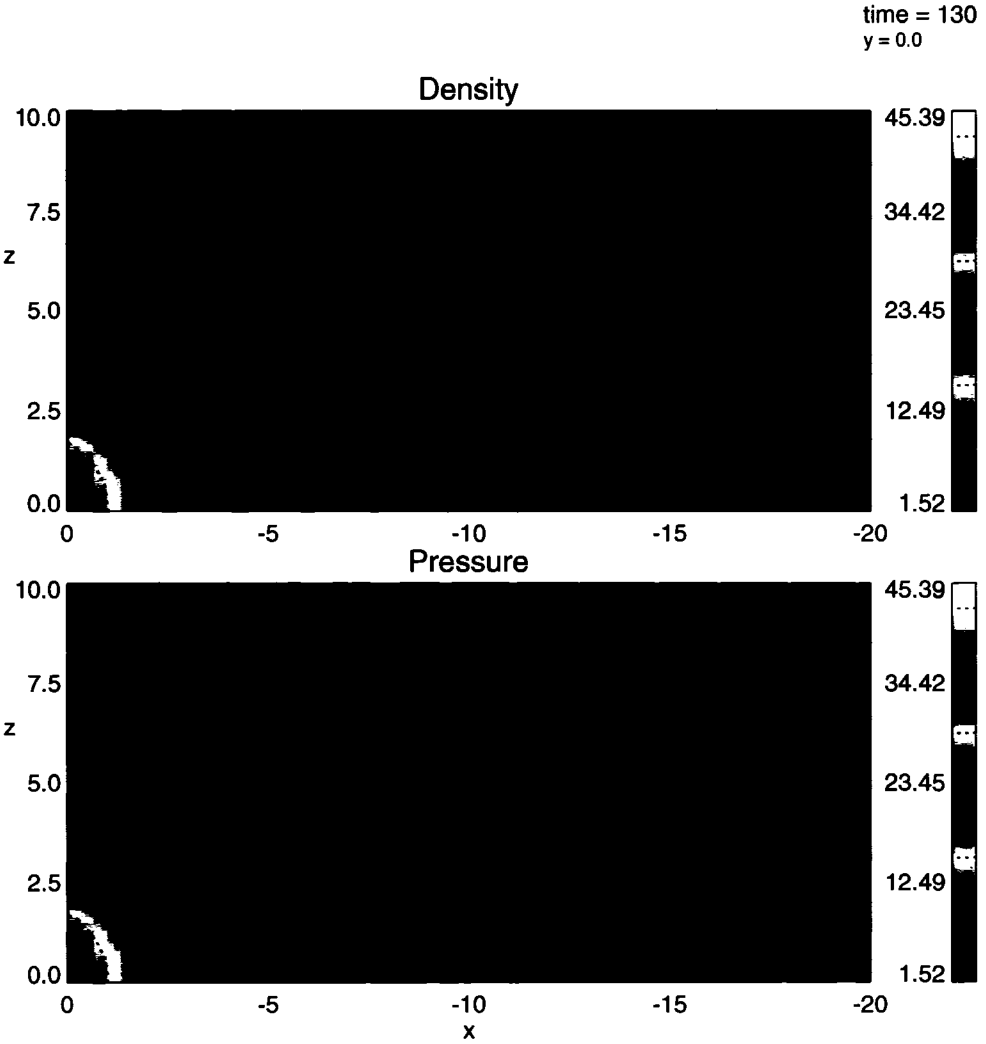

Figure 3.13. Equilibrium density and pressure in the noon-midnight meridian. The density and pressure in the noon-midnight meridian ($y = 0$) at $t = 130\ t_A$, at the end of the relaxation.

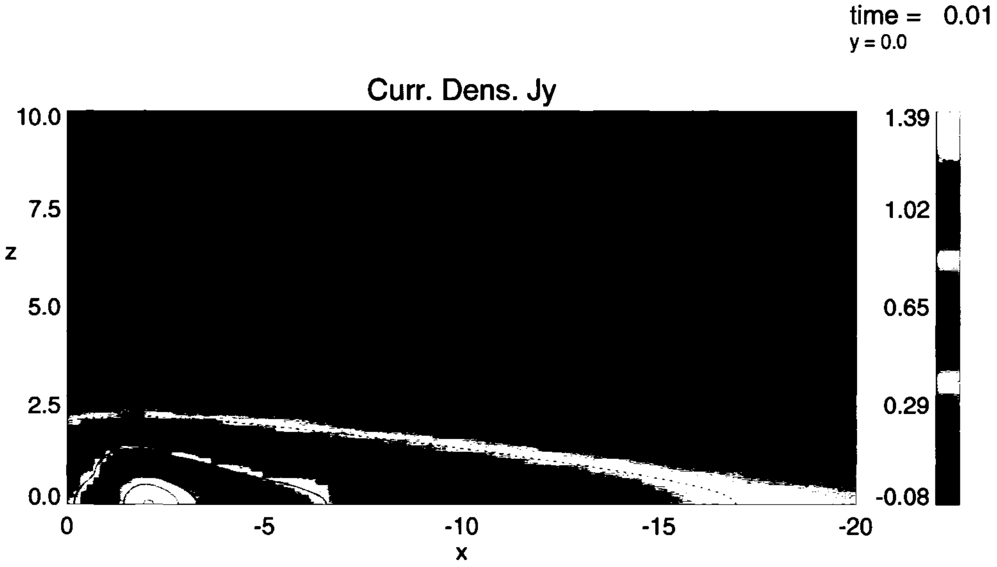

Figure 3.14. Non-equilibrium current density in the noon-midnight meridian. The y-component of the current density in the noon-midnight meridian ($y = 0$) at $t = 0.01\ t_A$, at the beginning of the relaxation.

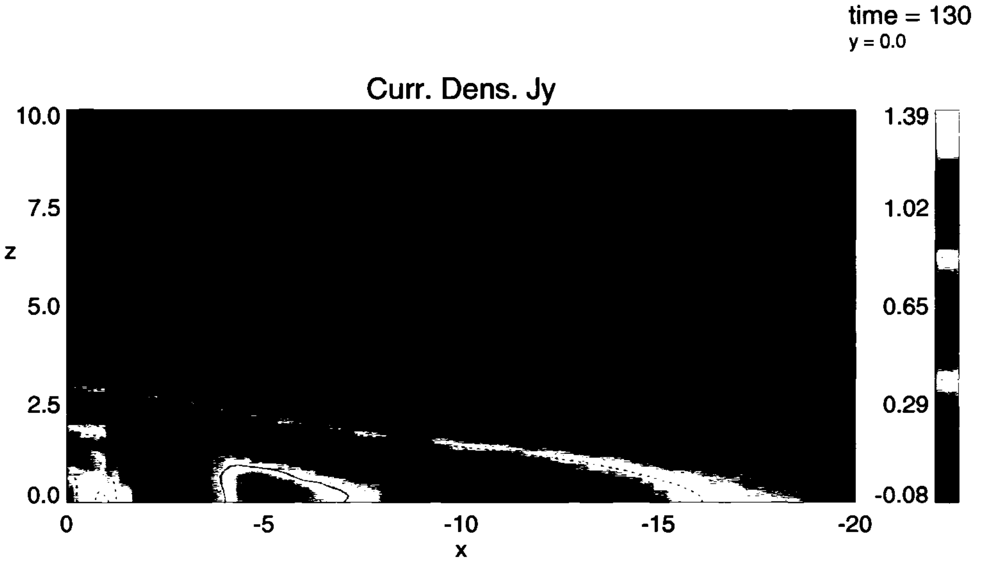

Figure 3.15. Equilibrium current density in the noon-midnight meridian. The y-component of the current density in the noon-midnight meridian ($y = 0$) at $t = 130\ t_A$, at the end of the relaxation.

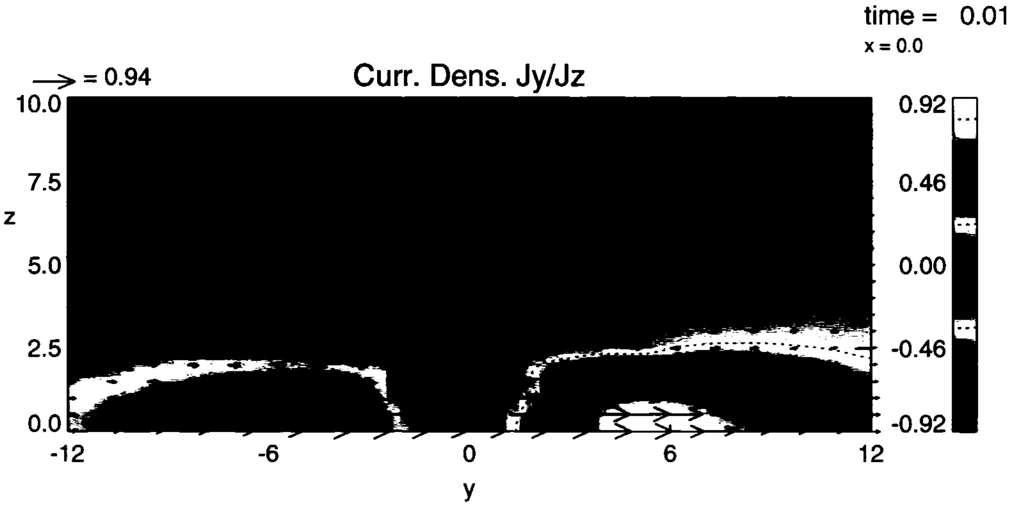

Figure 3.16. Non-equilibrium current density at the Earthward boundary. The current density at the Earthward boundary ($x = x_{max}$) at $t = 0.01\ t_A$, at the beginning of the relaxation. The arrows represent $\mathbf{j}_t = j_y \mathbf{e}_y + j_z \mathbf{e}_z$, the component of the current density that lies in this plane. The colors give the value of j_x, the component of the current density that is normal to this plane.

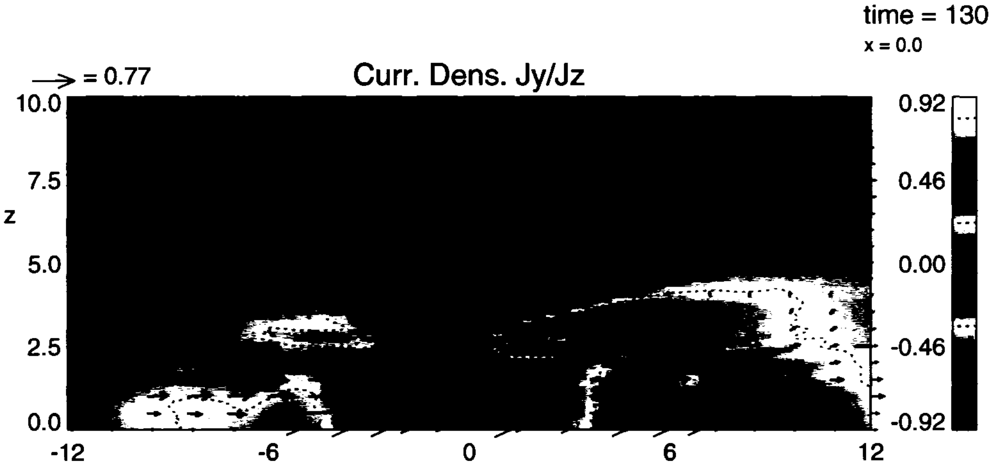

Figure 3.17. Equilibrium current density at the Earthward boundary. The current density at the Earthward boundary ($x = x_{max}$) at $t = 130\ t_A$, at the end of the relaxation. The same convention used in Figure 3.16 is used here.

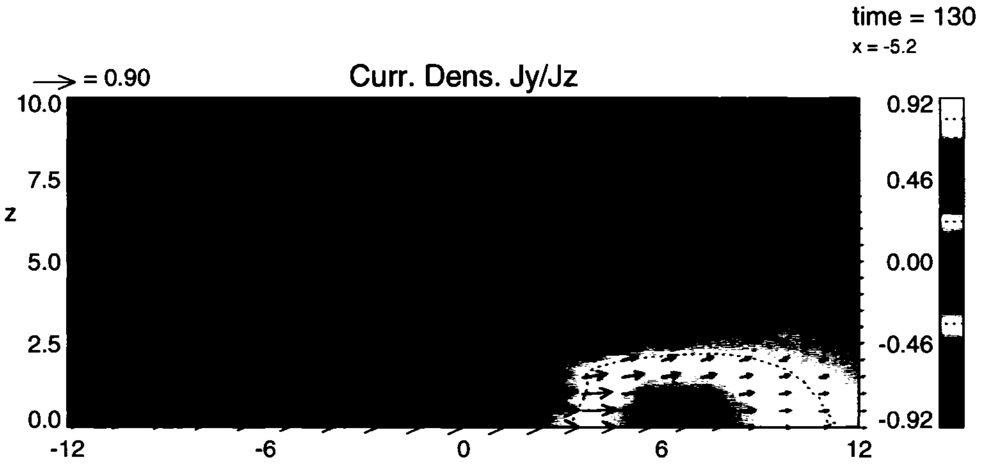

Figure 3.18. Downtail current density. The current density in the plane ($x = -5.2$) at $t = 130\ t_A$, at the end of the relaxation. The same convention used in Figure 3.16 is used here.

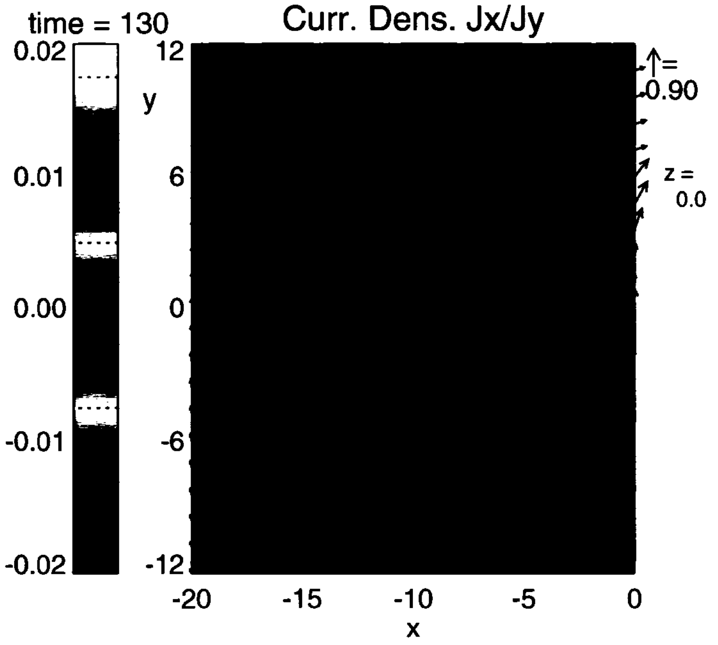

Figure 3.19. Equilibrium current density in the equatorial plane. The current density in the equatorial plane ($z = 0$) at $t = 130\ t_A$, at the end of the relaxation. The arrows represent $\mathbf{j}_t = j_x\mathbf{e}_x + j_y\mathbf{e}_y$, the component of the current density in this plane. The background color represents the value of j_z, the component of the current density that is normal to this plane.

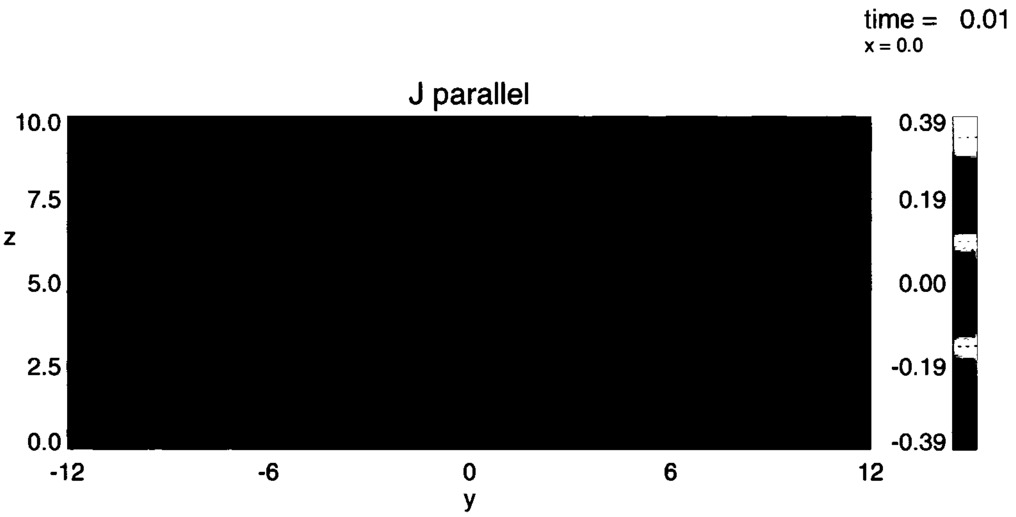

Figure 3.20. Non-equilibrium field-aligned currents at the Earthward boundary. Field-aligned currents at the Earthward boundary ($x = x_{max}$) at $t = 0.01\ t_A$, at the beginning of the relaxation.

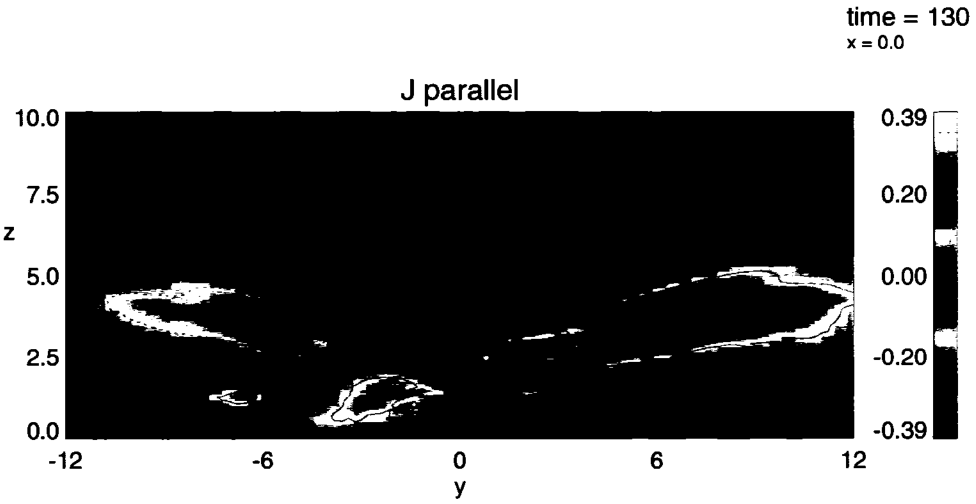

Figure 3.21. Equilibrium field-aligned currents at the Earthward boundary. Field-aligned currents at the Earthward boundary ($x = x_{max}$) at $t = 130\ t_A$, at the end of the relaxation.

changes form appreciably in both sense and structure over the course of the relaxation. The field-aligned currents there at the beginning of the relaxation ($t = 0.01\ t_A$) are shown in Figure 3.20, whereas that system at the end of the relaxation ($t = 130\ t_A$) is shown in Figure 3.21. We see that these field-aligned currents reverse direction by the end of the relaxation. Although there are similarities between the structure at the beginning of the relaxation and at its end, we see that the stronger currents at higher values of z have bifurcated. This field-aligned current system at the end of the relaxation has the sense of the Region-2 field-aligned current system. There is a weaker current system at smaller values of z that has the same sense as the Region-1 field-aligned current system. The Region-1 currents map to high latitudes in the ionosphere; the Region-2 currents map equatorward of the Region-1 currents. I have found that the sense of these field-aligned current systems depend sensitively to the manner in which the pressure is calculated. I continue work to better understand this dependence.

It serves one to compare the total acceleration at the beginning of the relaxation (at $t = 0.01\ t_A$) and at its end ($t = 130\ t_A$). The total acceleration in the plane $y = 0.1$, near the noon-midnight meridian, at these two times are shown in Figure 3.22 and Figure 3.23. These figures show two-dimensional cuts of the acceleration in the interior of the simulation domain. The acceleration on and immediately inside the simulation boundaries have not been plotted since it would overwhelm that in the interior. Note that this practice is consistent with the calculation of the force norm shown in Figure 3.6, which is calculated only in the interior of the simulation domain.

The magnitude represented by the reference arrow in Figure 3.22 is slightly more than three times the size of the corresponding arrow in Figure 3.23. One also sees that the range in the values of the normal component of the acceleration is slightly larger in Figure 3.22 than in Figure 3.23. But it is important to consider the structure of the acceleration profiles in the system.

One finds Figure 3.22 dominated by two structures: one extending from $-5 < x < -2.5$ and $2.5 < z < 10$ and the other extending from $-2.55 \leq x < 0$ and $0 < z < 2.5$. The structure at large values of z features large values of the tangential acceleration at its boundary at $x = -2.5$ throughout much of its extent in z. It features a smaller region, extending from $5 < z < 7.5$, in which the normal component of the acceleration is appreciable.

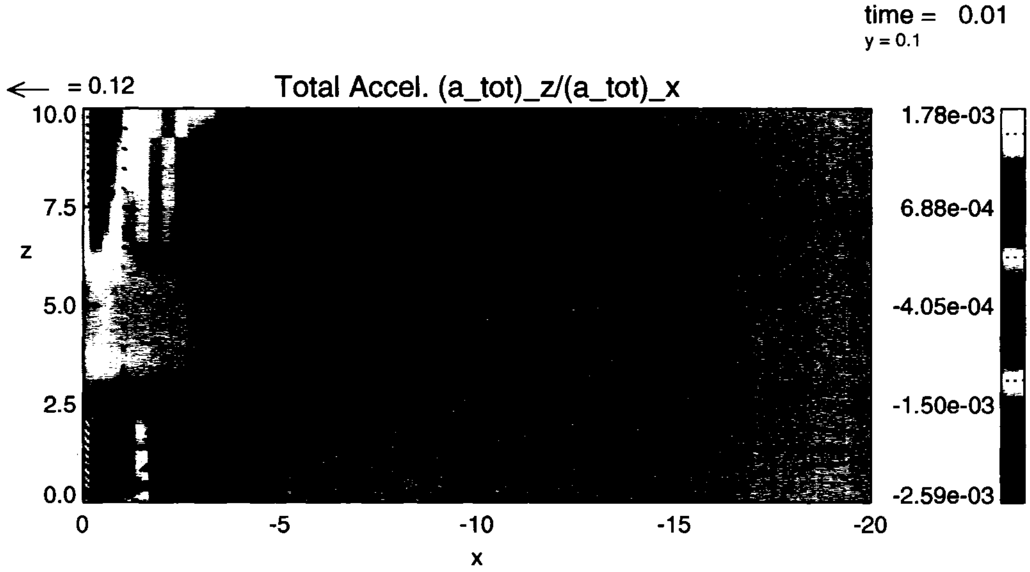

Figure 3.22. Total acceleration at the beginning of the relaxation. The total acceleration in the plane $y = 0.1$ at $t = 0.01\ t_A$, at the beginning of the relaxation. The arrows depict the acceleration $\mathbf{a}_t$ that is tangent to the plane ($\mathbf{a}_t = a_x\mathbf{e}_x + a_z\mathbf{e}_z$). The color bar give the value of the component of the total acceleration that is normal to the plane ($a_n = a_y$).

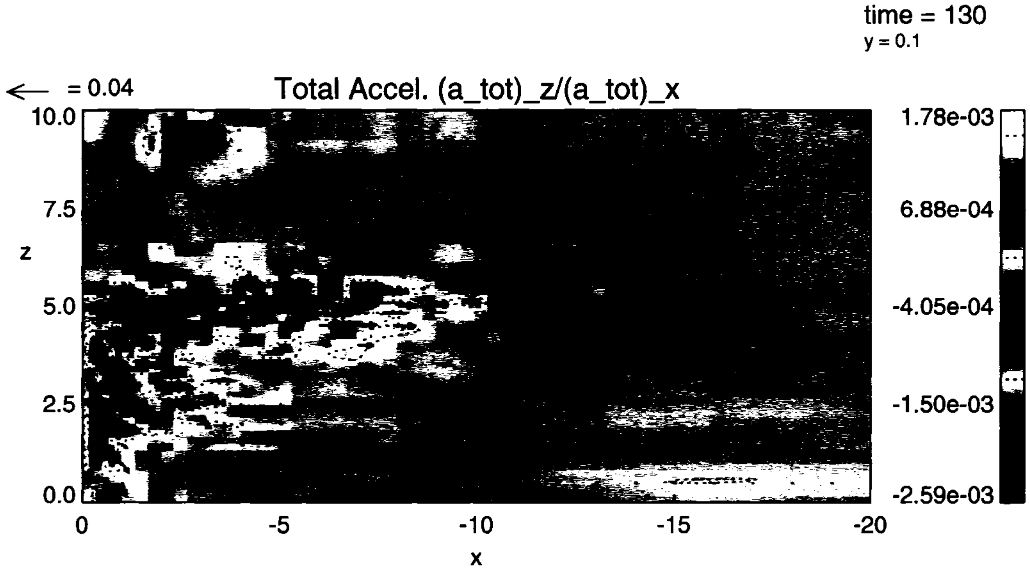

Figure 3.23. Total acceleration at the end of the relaxation. The total acceleration in the plane $y = 0.1$ at $t = 130\ t_A$, at the end of the relaxation. The same conventions used in Figure 3.22 are used here.

The structure at smaller z features appreciable tangential acceleration throughout much of its domain, as well as large magnitudes of the normal acceleration increasing toward the Earthward boundary.

Looking at Figure 3.23, one finds that the large ordered structures found in Figure 3.22 are gone. There is a region near the Earthward boundary, extending from $2.5 < z < 5$, where there are the normal component of the acceleration assumes large values. There is also a patch of high normal acceleration at (x,z) = (-4.8,5.1). There are two isolated instances of large tangential acceleration, namely at (x,z) (1,2.5) and (x,y) = (1,4.5). There is a region of smaller tangential acceleration extending from $-10 < x < -6$ and $3 < z < 5$. On the whole, the region of high acceleration at the end of the relaxation is mostly confined to the vicinity of the Earthward boundary.

I conclude by considering the distribution of the specific entropy in the equatorial plane for the initial equilibrium state, shown in Figure 3.24. Upon considering this figure along with Figure 2.4 (and keeping in mind that the origin of the x-axis in the simulation units of the former is offset 5 R_E from the origin of the x-axis in the latter) it seems that specific entropy contours in the range $-22 < x < -10$ (in simulation units) are relatively 'flat' (that is, remaining at the same value of x) in the vicinity of the noon-midnight meridian until drawing close to the dawn and dusk boundaries of the simulation domain. Contours lying further tailward bulge toward Earth, with these bulges growing increasingly prominent as one moves tailward.

3.7 Discussion and Summary

This chapter began with a discussion of basic aspects of the model, namely:

- the simulation domain
- the normalized equations solved by the simulation code, as well as the manner of their solution
- the normalization of quantities in the simulation
- the boundary conditions used in the simulation

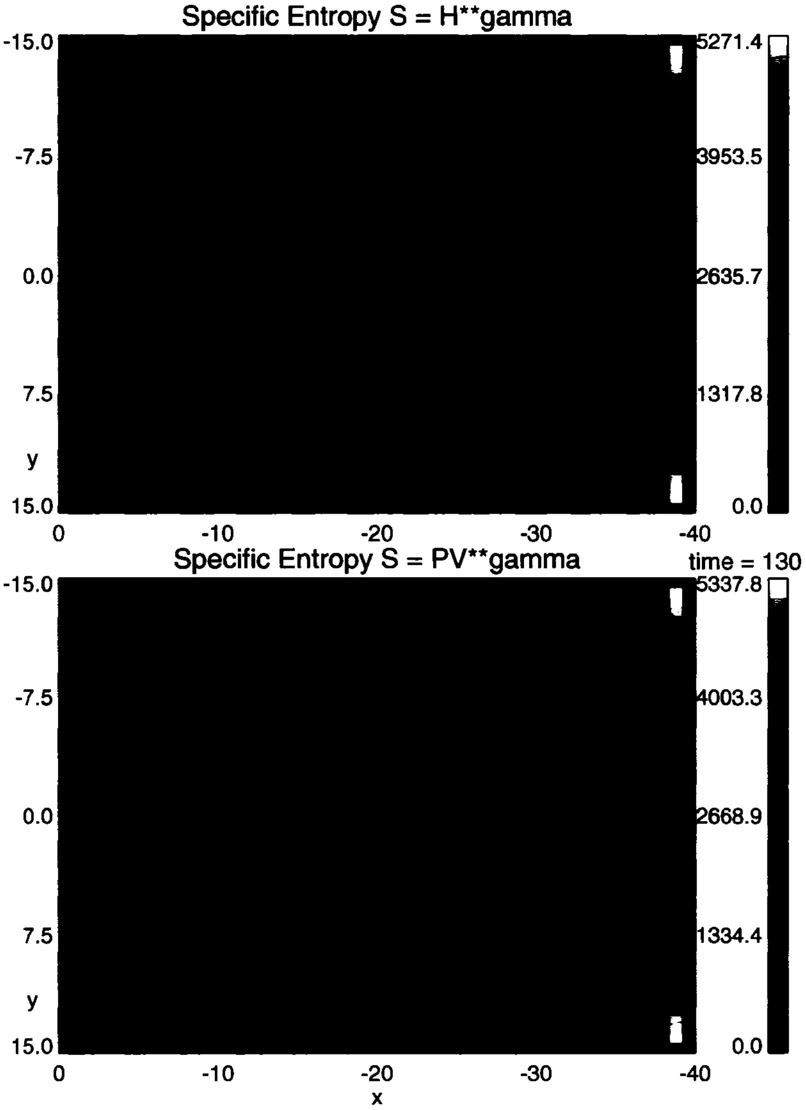

Figure 3.24. Specific entropy at the end of the relaxation. The specific entropy S at the time $t = 130\, t_A$. Colors are used to denote the value of the specific entropy (in simulation units). Contour lines are also provided. The top panel shows the specific entropy calculated using the expression $S = H^\gamma$. The lower panel shows the specific entropy calculated using the equivalent expression $S = PV^\gamma$.

That discussion gave way to another concerning the relaxation of the initial configuration to an equilibrium state (from which the plasma outflow can be instituted). The chapter ended with a discussion of the resulting initial equilibrium state.

Chapter 4

3D MHD Model—Outflow Boundary Condition and Results

4.1 Specification of the Outflow Boundary Condition

Once I have obtained a satisfactory equilibrium configuration, I need to apply the plasma flow toward the dayside as an outflow condition at our Earthward boundary (at x_{max}). In the real magnetosphere this flow is caused by erosion (through magnetic reconnection) at the dayside which causes a flow channel at a radial distance of about 10 R_E from the nightside to the dayside. The velocity in this channel is determined by the global reconnection rate which is approximately given by the cross polar cap potential. Thus each (westward and eastward) channel transports approximately the magnetic flux corresponding to half the cross-polar cap potential.

The outflow causes the evacuation of the flux reservoir located in the near-Earth magnetotail. This boundary condition is applied by mapping an azimuthal velocity profile specified in the equatorial plane to the Earthward boundary.

The velocity magnitude and width of the channel should be scaled with the observed flux transport rate. In order to speed up the simulation, the simulated transport is chosen to be slightly higher than observed. The outflow boundary condition is instituted shortly after the end of the relaxation.

4.1.1 Specification of Azimuthal Velocity Profile in the Equatorial Plane

I begin by specifying the velocity profile in the equatorial plane. The mapping of this profile to the Earthward boundary will be discussed in the following subsection. The velocity profile in the equatorial plane has the form

$$\mathbf{v} = v_\varphi \mathbf{e}_\varphi. \tag{4.1}$$

Here v_φ is the azimuthal component of the velocity in the equatorial plane (with the origin at Earth's center) and $\mathbf{e}_\varphi$ is the unit vector in the azimuthal direction. Note that this velocity has no radial component. (That is, $v_r = 0$.) The azimuthal component depends on both r and φ

$$v_\varphi = v_\varphi\left(r, \varphi\right) \tag{4.2}$$

Parameter	Value (in normalized units)	Value (in physical units)
r_0	9.0	9.0 R_E
r_ℓ	1.0	1.0 R_E
r_w	0.5	0.5 R_E
y_0	10.0	10.0 R_E
y_ℓ	2.0	2.0 R_E
z_ℓ	2.5	2.5 R_E
v_0	0.222991	97.45 km/s
t_0	0.2	2.92 s
t_{st}	130	31.6 minutes
Φ_E	1.035	57.7 kV

Table 4.1. Typical Outflow Parameters

and is chosen to have the form

$$v_\varphi\left(r,\varphi\right) = 2v_0 f(r)\left[\frac{(\varphi-\pi)}{\pi}\right]. \tag{4.3}$$

Here v_0 is the characteristic speed of the outflow and the φ dependence is chosen so that the flow is divergent in the midnight sector. (As shown in Figure 4.1, φ is measured from the Sunward direction.) The function $f(r)$ is designed to limit the outflow to an annular region in the equatorial plane. It is given by

$$f(r) = \left(\frac{1}{2}\right)\left\{\tanh\left[\frac{(r-r_0+r_\ell)}{r_w}\right] - \tanh\left[\frac{(r-r_0-r_\ell)}{r_w}\right]\right\}. \tag{4.4}$$

It has a magnitude near unity in the annular region wherein the outflow lies. It quickly, but smoothly, decreases to zero outside this 'outflow channel.' The values of the parameters r_0, r_ℓ, and r_w are given in Table 4.1. Note that the form of $v_\varphi\left(r,\varphi\right)$ ensures that its magnitude at both $\varphi = \frac{\pi}{2}$ and $\varphi = \frac{3\pi}{2}$ is v_0 scaled by the factor $f(r)$; it also ensures that the direction of the flow is correct. (Please refer to Figure 4.1.)

In order to implement this outflow profile in the simulation code, it must be expressed in Cartesian coordinates. The azimuthal unit vector $\mathbf{e}_\varphi$ can be decomposed into its Cartesian

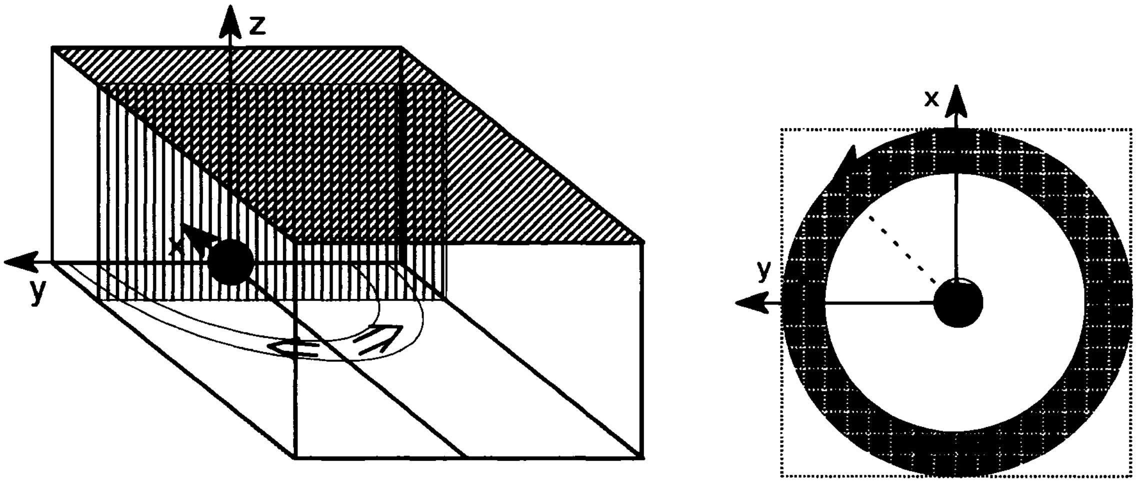

Figure 4.1. Specification of the plasma outflow at the Earthward boundary ($x = x_{max}$). On the left is shown the simulation domain, with the imposed plasma outflow from $y = 0$ in the equatorial plane being depicted by open arrows. The Earthward boundary of the simulation box is shown in red. Note that the origin of the coordinate system used in the simulation is displaced from the origin of the GSM coordinate system by the distance $r_{min} = 5\,R_E$ along x. The Earthward boundary lies at $x = 0$ in the simulation domain; but it is located at $x_{GSM} = -r_{min}$ in GSM coordinates. That is, the Earthward boundary of the simulation is located 5 R_E downtail from Earth. On the right is shown the polar geometry used to specify the outflow in the equatorial plane (viewed from above). Open arrows depict plasma flow. The 'flow channel' lies in the limited radial range depicted in blue. Note that the angle φ is measured from the x-axis.

components:

$$\mathbf{e}_\varphi = -\sin(\varphi)\,\mathbf{e}_x + \cos(\varphi)\,\mathbf{e}_y. \tag{4.5}$$

Here $\mathbf{e}_x$ and $\mathbf{e}_y$ are the unit vectors in the directions of x and y, respectively. Now I can write the velocity in terms of its x and y-components.

$$\mathbf{v} = v_x(r,\varphi)\,\mathbf{e}_x + v_y(r,\varphi)\,\mathbf{e}_y, \tag{4.6}$$

with

$$v_x(r,\varphi) = -2v_0 f(r)\left[\frac{(\varphi-\pi)}{\pi}\right]\sin(\varphi) \tag{4.7}$$

$$v_y(r,\varphi) = 2v_0 f(r)\left[\frac{(\varphi-\pi)}{\pi}\right]\cos(\varphi). \tag{4.8}$$

Since

$$\sin(\varphi) = \frac{y}{r} \tag{4.9}$$

and

$$\cos(\varphi) = \frac{x}{r}, \tag{4.10}$$

while the radius is given by

$$r = \left(x^2+y^2\right)^{\frac{1}{2}}, \tag{4.11}$$

I can write

$$v_x(r,\varphi) = -2v_0 f(r)\left[\frac{(\varphi-\pi)}{\pi}\right]\left[\frac{y}{(x^2+y^2)^{\frac{1}{2}}}\right] \tag{4.12}$$

$$v_y(r,\varphi) = 2v_0 f(r)\left[\frac{(\varphi-\pi)}{\pi}\right]\left[\frac{x}{(x^2+y^2)^{\frac{1}{2}}}\right]. \tag{4.13}$$

These expressions use GSM coordinates, rather than simulation coordinates. To write them in terms of the simulation coordinates, one must take into account the displacement of the origin of the simulation along the x-axis by the distance $r_{min} = 5\,R_E$. If one applies the transformation

$$x \longrightarrow x + r_{min} \tag{4.14}$$

the results above will be expressed in simulation coordinates. Typical parameters used to specify this imposed velocity profile in this study are shown in Table 4.1.

4.1.2 Mapping of the Equatorial Velocity Profile to the Earthward Boundary

The actual formulation of the outflow boundary condition is a non-trivial problem. A rigorous approach to MHD boundary conditions would require the solution of the characteristics of the MHD equations for the actual configuration. However, the problem has not been solved for a general three-dimensional system. Therefore any 3D MHD boundary condition except for cases with a defined symmetry (e.g., the equatorial plane in our simulation) is usually a more or less intelligent guess. The choice of boundary conditions is subject to a number of constraints depending on the specific situation. In this case the challenge is to move not only plasma but also magnetic flux through a boundary in a continuous and smooth manner, i.e., without causing extreme currents that will ultimately lead to the termination of a simulation. In initial attempts I specified an outflow profile at the Earthward boundary without considering the magnetic field structure inside the simulation. Despite a large number of variations on the outflow conditions, attempts to apply smoothing and diffusion (to suppress high current densities), etc., these efforts were not successful. I finally came to the conclusion that a specified outflow has to consider the structure of the magnetic field that maps into the outflow region. The assumption of the outflow channel (Equations 4.12 and 4.13) finally provided a solution to the outflow problem. For the actual mapping I used two methods, one of which would map the convection electric field from the equatorial plane along the magnetic field to the Earthward boundary. The other one would ensure a rigid rotation of field lines for this mapping. Since the second method proved slightly better I describe it in more detail. While these methods did not yield the desired duration for the runs, they did improve stability greatly and allowed the results presented here.

Consider a magnetic field line that connects a point on the Earthward boundary with a point on the equatorial plane. If one assumes that this magnetic field line moves as a rigid body, then those two points will move with the same angular velocity $\dot{\varphi} = \frac{d\varphi}{dt}$. Since the magnitude of the azimuthal velocity of the point on the equatorial plane, located at the radial distance r_{eq}, is given by

$$(v_\varphi)|_{eq} = r_{eq}\,\dot{\varphi}, \tag{4.15}$$

I can write

$$\dot{\varphi} = \frac{(v_\varphi)|_{eq}}{r_{eq}}. \tag{4.16}$$

Similarly, the magnitude of the azimuthal velocity of the corresponding point on the Earthward boundary, located at the radial distance r_b, can be written as

$$(v_\varphi)|_b = r_b\,\dot{\varphi}. \tag{4.17}$$

I can use Equation 4.16 to write

$$(v_\varphi)|_b = r_b \left[\frac{(v_\varphi)|_{eq}}{r_{eq}}\right] \tag{4.18}$$

or

$$(v_\varphi)|_b = \left(\frac{r_b}{r_{eq}}\right)(v_\varphi)|_{eq}. \tag{4.19}$$

The magnetic field line passing through each point on the Earthward boundary is traced to the equatorial plane to determine the location of its footpoint on the equatorial plane. Once that location is known, r_{eq} can be readily calculated. Since $(v_\varphi)|_{eq}$ is the specified outflow velocity given by Equation 4.3, I can use Equation 4.19 to compute the velocity field on the Earthward boundary. I invoke Equation 4.19 to write the x and y components of the velocity at the Earthward boundary as

$$[(v_\varphi)|_b]_x = \left(\frac{r_b}{r_{eq}}\right)\left[(v_\varphi)|_{eq}\right]_x \tag{4.20}$$

and

$$[(v_\varphi)|_b]_y = \left(\frac{r_b}{r_{eq}}\right)\left[(v_\varphi)|_{eq}\right]_y, \tag{4.21}$$

where $\left[(v_\varphi)|_b\right]_x$ and $\left[(v_\varphi)|_b\right]_y$ are given by Equations 4.12 and 4.13, respectively. These expressions are applied to the specification of the mass flux at the Earthward boundary:

$$(s_x)|_b = \rho_b \left[(v_\varphi)|_b\right]_x \tag{4.22}$$

$$(s_y)|_b = \rho_b \left[(v_\varphi)|_b\right]_y . \tag{4.23}$$

4.2 Evolution of the System under the Influence of the Outflow Boundary Condition

4.2.1 Outflow and Magnetic Flux Transport

In the following section I will discuss and analyze one specific case in more detail. This case is representative of several runs that gave very similar results. Parameters that I varied for these runs include the frequency with which the magnetic field line tracing was performed and the application of anti-symmetry of s_x across the Earthward boundary. The main objective for these variations was the attempt to maintain the simulation for about 120 to 160 Alfvén times (corresponding to the 30 to 40 minute growth phase). However, the best runs have durations of 7 to 12 minutes, short of the ~30 minutes expected for drastic thinning. However, the results show the beginning of current sheet thinning, documenting the dynamics associated with current sheet thinning, and allow one to determine the rate of current sheet thinning. For these reasons I believe I are justified in focusing on one particular case.

The outflow described in the last section is imposed at t = 130 t_A, immediately after the end of the relaxation. The velocity profile in the plane $z = 0.03$, just above the equatorial plane, at t = 135 t_A is shown in Figure 4.2. The arrows in this figure represent the velocity $\mathbf{v}_t = v_x\mathbf{e}_x + v_y\mathbf{v}_y$ in this plane. The colors represent the value of v_z, the velocity component that is normal to this plane. Although there is some slight variation in v_z, the velocity in the z-direction is less than 0.01 (in simulation units) in this plane. The imposed azimuthal flow pattern is clearly dominant. This flow was discussed in Section 4.1.1 and sketched in Figure 4.1. Again, the parameters corresponding to this flow are shown in Table 4.1. This flow is divergent, increasing in magnitude as one moves to larger values of $|y|$; the velocity

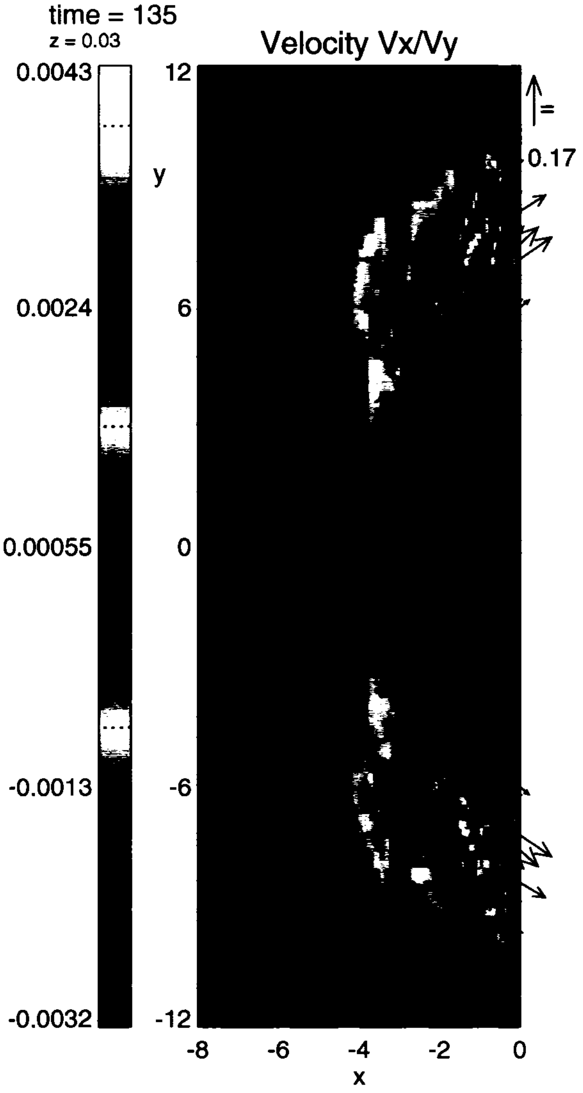

Figure 4.2. Velocity profile immediately above the equatorial plane. The imposed velocity profile in the plane $z = 0.03$, just above the equatorial plane, at $t = 135\,t_A$. The arrows represent the tangential velocity $\mathbf{v}_t = v_x\mathbf{e}_x + v_y\mathbf{e}_y$. The colors represent the value of the normal velocity component v_z.

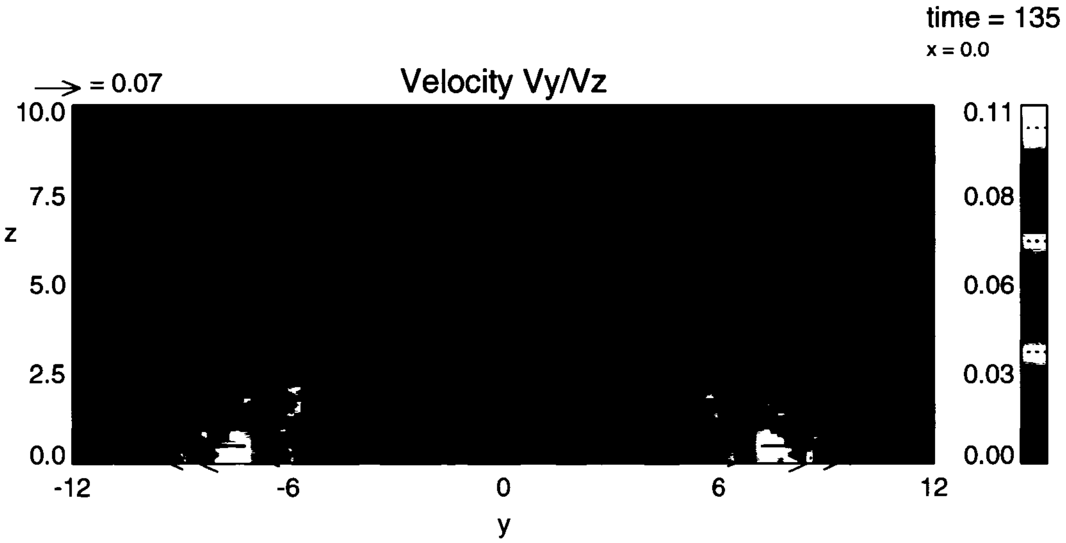

Figure 4.3. Velocity profile at the Earthward boundary. The velocity profile mapped to the Earthward boundary ($x = x_{max} = 0$) at $t = 135\,t_A$. The arrows represent the velocity $\mathbf{v}_t = v_y\mathbf{e}_y + v_z\mathbf{e}_z$ in this plane. The colors represent the value of v_x, the velocity component that is normal to this plane.

is zero along $y = 0$. The flow is confined to a narrow annular channel. The width of this channel corresponds to the narrow downtail extent of the 'magnetic flux reservoir.' It is worthy that there is rather little flow from downtail of this flow channel. This confirms that such flow is greatly restricted by the conservation of specific entropy.

The velocity mapped to the Earthward boundary at that same time is shown in Figure 4.3. Here the arrows represent the velocity $\mathbf{v}_t = v_y\mathbf{e}_y + v_z\mathbf{e}_z$ tangential to the Earthward boundary. The colors represent the value of v_x, the component of the velocity normal to this boundary. One sees that the outflow is confined to two regions of the Earthward boundary lying near the equatorial plane. The flow along the Earthward boundary lies nearly entirely in the y-direction; that is, v_z is quite small compared to v_y in this plane. The magnitude of v_x is comparable to v_y. One sees that v_x has two maxima corresponding to the two 'edges' of the outflow seen near the Earthward boundary in Figure 4.2.

Note that the characteristic magnitude $v_0 = 0.222991$ that is used here (as given in Table 4.1) is over four times the value used, in Section 1.5 in Chapter 1 and Appendix E, to estimate the time needed to evacuate the magnetic flux reservoir. Accordingly, I expect that the time needed to evacuate the flux reservoir, using these flow parameters, should be reduced by a corresponding factor of four from that estimated earlier. Given the characteristic Alfvén time of the simulation is $t_A = 14.6$ s, the estimate of 30 minutes given earlier corresponds to approximately 123 t_A. Since I am using a characteristic outflow speed that is four times the expected physical value, I would expect to see appreciable evolution of the system in approximately 31 t_A. The outflow was started at the end of the relaxation at 130 t_A and continued until 161 t_A, where the code terminated due to numerical instability. The choice of this high value of v_0 was motivated, in part, by a desire to keep the length of program runs practical. Given the large number of treatments of the Earthward boundary condition attempted through the study, this consideration is an important one.

This plasma outflow removes a considerable amount of magnetic flux from the near-Earth magnetotail, as evidenced in the plots of the magnetic field at the Earthward boundary shown in Figure 4.4. The change in b_x seen in the vicinity of $z = 2.5$ results from the removal of magnetic flux from the region mapping to the location on the Earthward boundary. The effect of this flux removal can also be seen in the plots of the magnetic field in the equatorial plane shown in Figure 4.5. One can see that the region of lower b_z (represented by purple and black) has encroached upon the near-Earth magnetotail. The magnetic flux in the rectangular region bounded by $-5.2 \leq x \leq 2.1$ and $-5.9 \leq y \leq +5.9$ has been reduced to 82% of its initial value at $t = 130\,t_A$ by the time $t = 161\,t_A$, as shown in Figure 4.6. As the magnetic field evolves and becomes more tail-like, the distribution of specific entropy in the system will also change. Accordingly, the flow profile will itself evolve as time progresses. Figure 4.7 shows the specific entropy profile in the equatorial plane at times 130 and 161 t_A. The tailward extension of contour lines at the later time is most pronounced in the vicinity of the noon-midnight meridian. I will now examine consequences of this transport of magnetic flux out of the near-Earth magnetotail for the distributions of current density and velocity in the system.

4.2.2 Development of Current Density and Velocity Features

Figure 4.8 illustrates the evolution of the current density in the noon-midnight meridian ($y = 0$) in the course of the simulation. In the top panel one sees the current density at $t = 130\,t_A$. The maximum current density occurs near the equatorial plane, near $x = -5$.

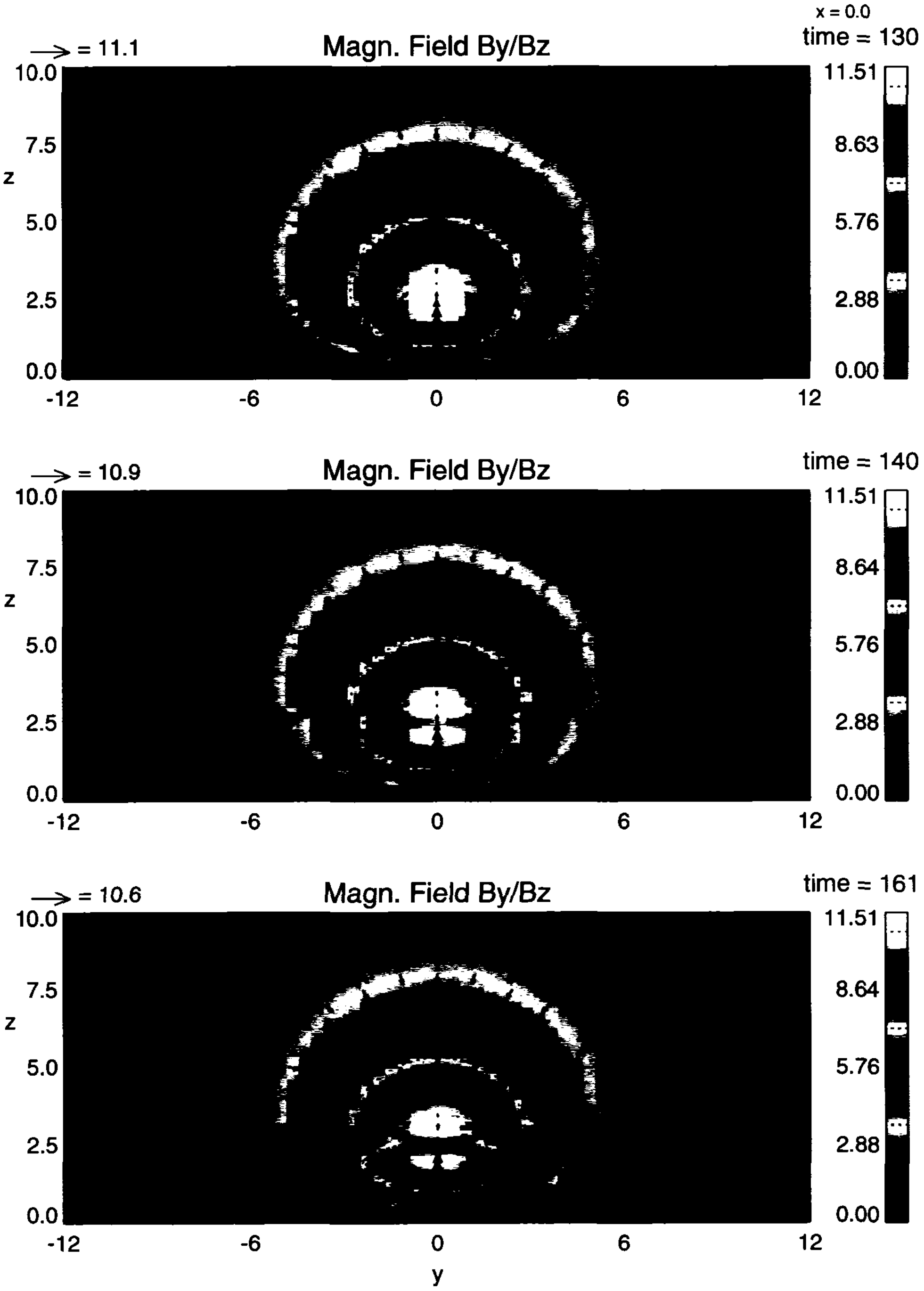

Figure 4.4. Evolution of the magnetic field at the Earthward boundary. The magnetic field at the Earthward boundary ($x = x_{max} = 0$) at 130, 140, and 161 t_A. The same convention used in Figure 3.8 is used here. Arrows show the direction of the tangential magnetic field $\mathbf{b}_t = b_y \mathbf{e}_y + b_z \mathbf{e}_z$, while colors give the value of the normal magnetic field component b_x.

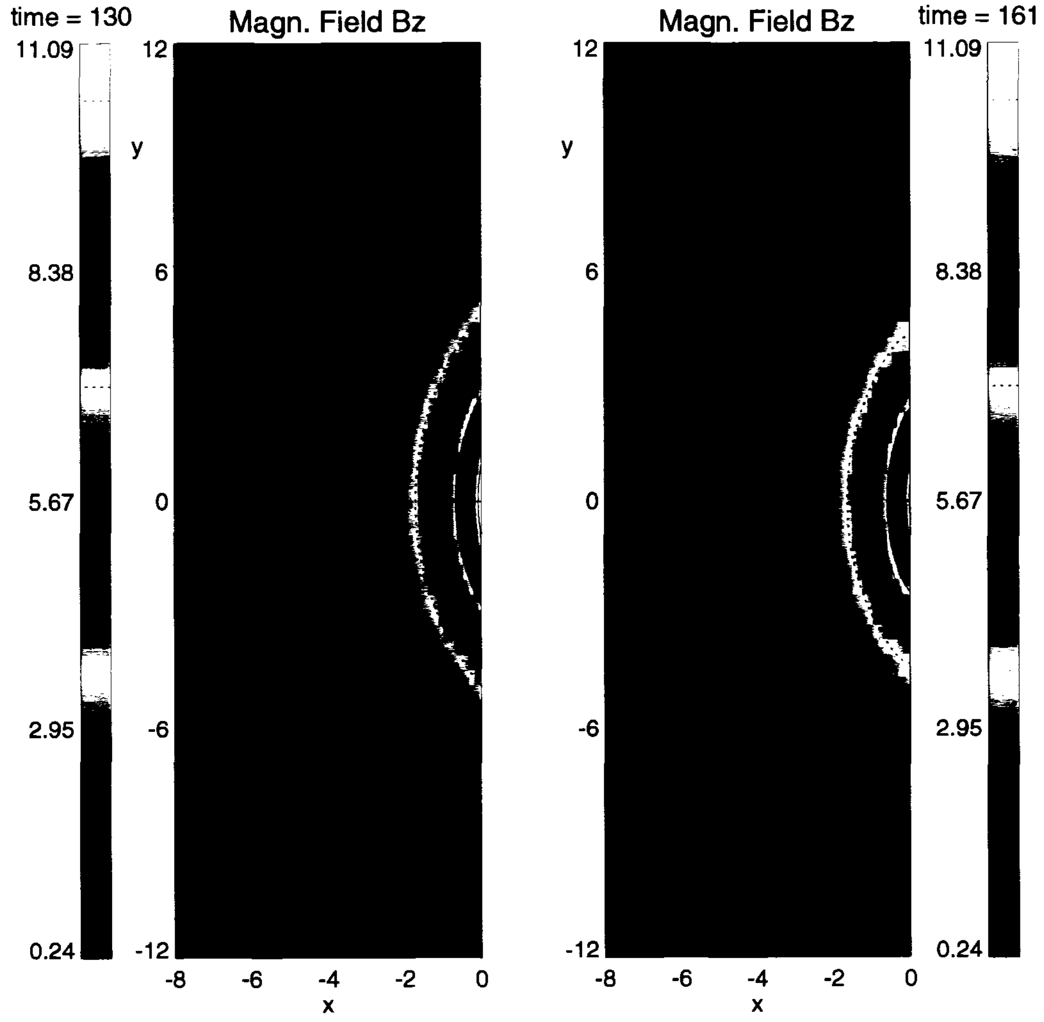

Figure 4.5. Evolution of the magnetic field in the equatorial plane. The magnetic field in the near-Earth equatorial plane ($z = 0$) at 130 and 161 t_A. Since b_x and b_y are anti-symmetric across this plane, the magnetic field there is entirely in the z-direction. That is, $\mathbf{b} = b_z \mathbf{e}_z$ in the equatorial plane.

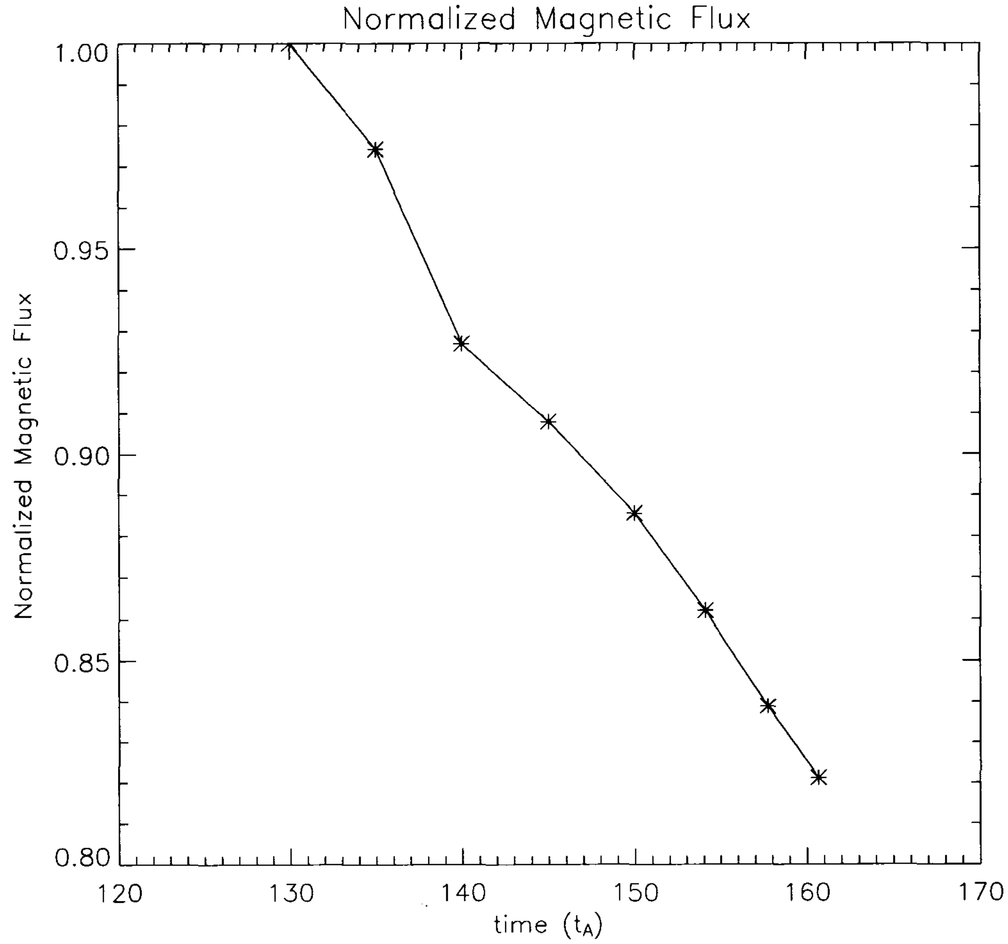

Figure 4.6. Magnetic flux reduction in the central equatorial plane. The normalized magnetic flux in the region $-5.2 \leq x \leq -2.1$ and $-5.9 \leq y \leq +5.9$ in the equatorial plane ($z = 0$) as a function of time while the outflow boundary condition is applied. The values of the magnetic flux have been normalized to the value of the magnetic flux when the outflow was started at $t = 130\, t_A$.

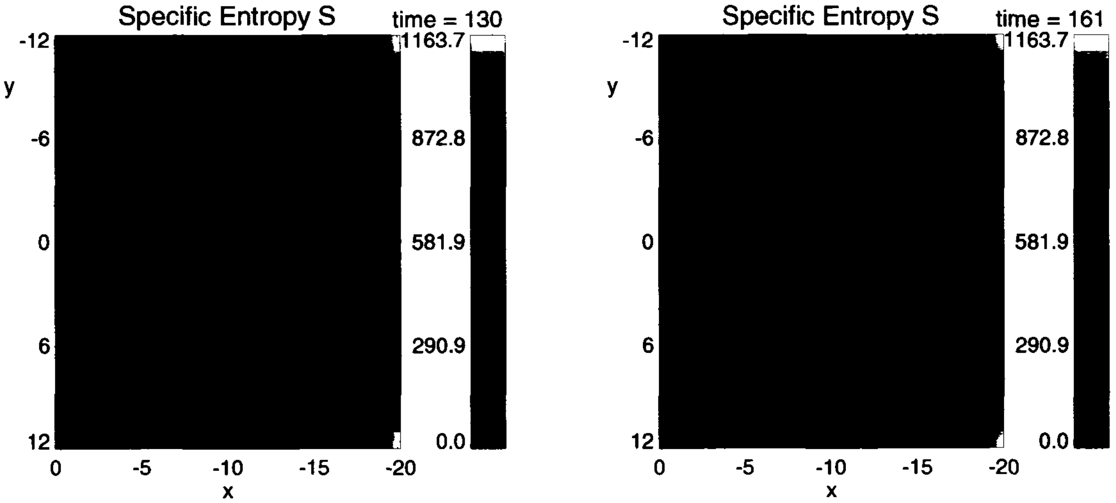

Figure 4.7. Evolution of the specific entropy in the equatorial plane. The specific entropy in the equatorial plane ($z = 0$) at 130 and 161 t_A.

In the course of the simulation, the profile of the current density becomes more complex. The current maximum is no longer confined to the vicinity of the equatorial plane. Instead, one sees the development of a long, thin current structure—extending diagonally from near (x,z) = (-3.8,2) to (x,z) = (-8,0) in the second panel of Figure 4.8. This current feature is associated with the corresponding feature in the velocity that is shown in the third panel of Figure 4.8. This plot shows the velocity in the plane $y = 0.06$, immediately adjacent to the noon-midnight meridian. These structures are even more prominent further away from the noon-midnight meridian, as seen in Figure 4.9. The plasma is accelerated across this current feature, as one can see in the third panel of Figure 4.8.

I interpret this structure as a type of plasma discontinuity known as a slow shock. The properties of the plasma can change abruptly across such a discontinuity. Both the pressure p and the density ρ increase, while the magnetic field component tangential to the shock decreases, downstream of a slow shock. The downstream direction is defined as Earthward of the slow shock, whereas the upstream direction is defined as tailward of the slow shock. The changes in p, ρ, and $\mathbf{b}$ across the shock are superposed on other variations in these plasma properties that arise because of magnetospheric structure; accordingly, they are not readily apparent on visual inspection. On the other hand, the change in the velocity and

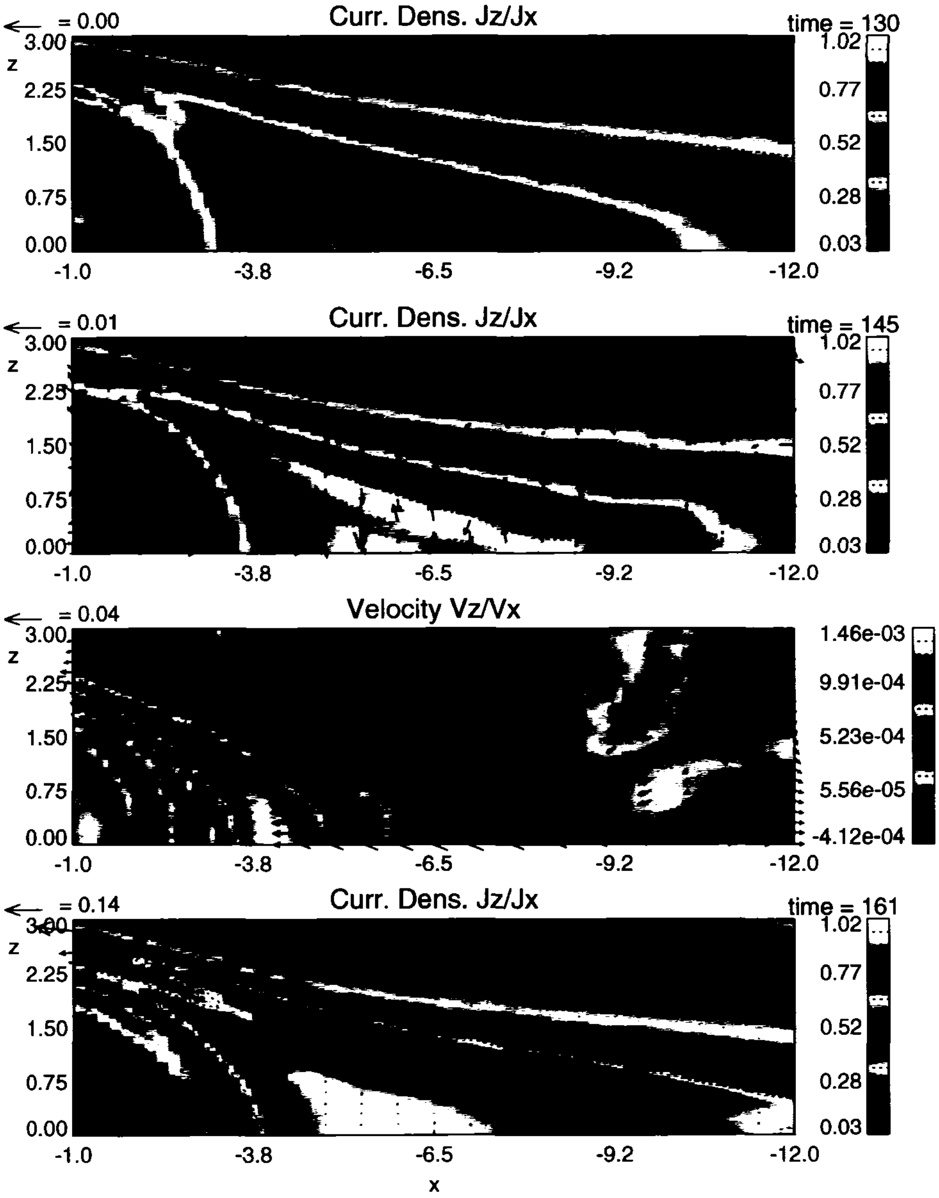

Figure 4.8. Current density and velocity in the vicinity of the noon-midnight meridian ($y = 0$). The top panel shows the current density at $t = 130\,t_A$. The next two panels show the current density and velocity at the time $t = 145\,t_A$. The bottom panel shows the current density at $t = 161\,t_A$. As in earlier plots, arrows depict the tangential component of vector quantity (current density or velocity) in consideration. The colors give the value of the component normal to the plane shown. The plots of the current density correspond to the noon-midnight meridian ($y = 0$). The plot of the velocity corresponds to the plane $y = 0.06$, immediately adjacent to the noon-midnight meridian.

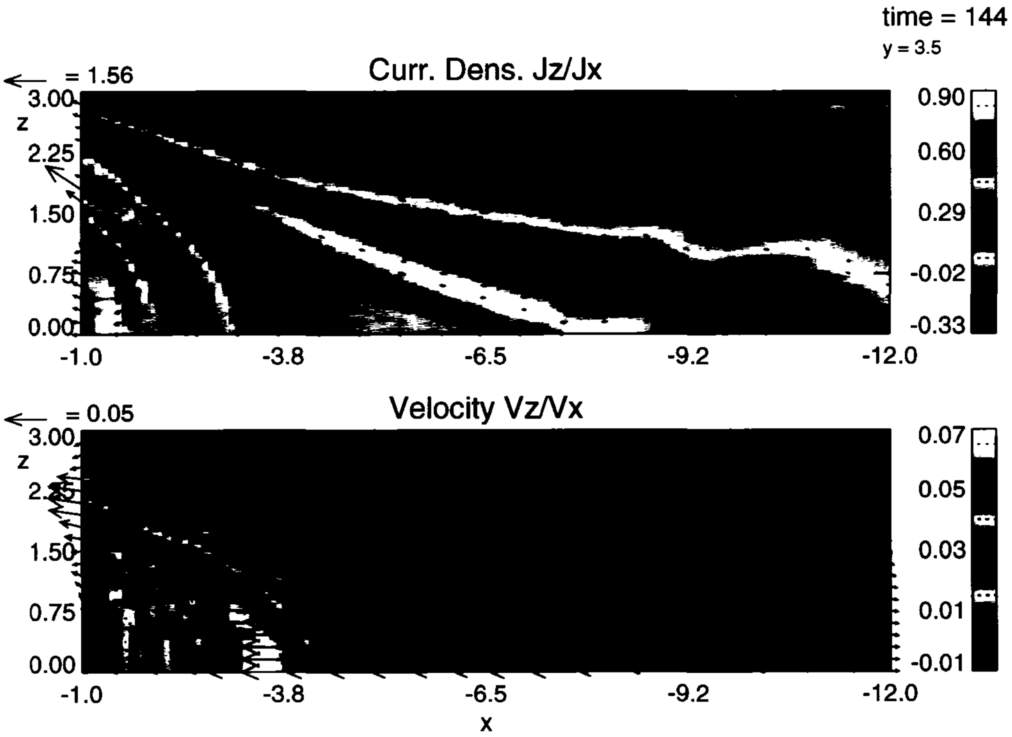

Figure 4.9. Current density and velocity away from the noon-midnight meridian. The current density and velocity in the plane $y = 3.5$ at $t = 145 t_A$. The same conventions in Figure 4.8 are used here.

the intensification of the current associated with this feature (which carries ~6% of the total cross-tail current) are readily apparent. Further analysis is needed to quantify the nature of this slow shock. I interpret this structure as the means through which the outflow boundary condition is communicated in the plasma. Plasma is accelerated across this structure to the velocities required to satisfy the imposed boundary condition.

Note that the maximum value of j_y has increased by 13% from its value at $t = 130\,t_A$ by the time $t = 145\,t_A$. Again, the region of maximum current density has moved from a location near the equatorial plane at $t = 130\,t_A$; at $t = 145\,t_A$ it lies along the upper edge of the slow shock. By $t = 161\,t_A$, the maximum of the current density again lies in the vicinity of the equatorial plane. But the value of this maximum has decreased slightly from the maximum value of j_y at $t = 145\,t_A$, from 113% of the maximum value at $t = 130\,t_A$ to 111% of that maximum value.

One must take care in interpreting these maximum values of the current density. The steady intensification of the current density in the vicinity of $x = -5$ is masked, at time $t = 145\,t_A$, by the strong current density along the slow shock. The intensification of the current density in that vicinity continues as long as magnetic flux is removed from the flux reservoir in the near-Earth magnetotail. This trend is illustrated in Figure 4.10, which shows j_y in the equatorial plane in the region $-12 \leq x \leq -1$ along the noon-midnight meridian ($y = 0$). The maximum of j_y, initially near $x = -5$ at $t = 130\,t_A$, lies near $x = -8$. However, the profile of the current density has bifurcated; there is a local maximum near $x = -5$ only slightly smaller than the maximum at $x = -8$. By $t = 161\,t_A$, the profile of j_y has returned to a form more akin to that at $t = 130\,t_A$, with only a single 'hump.' But this maximum has moved slightly tailward, to the vicinity of $x = -6$. While j_y decreases with time $y > -5$ (Earthward of the magnetic flux reservoir), it increases in time over much of the reservoir, in the range $-12 \leq x \leq -5$. Note that while the increase in the global maximum of the current density is on the order to 11 to 13%, locally the current density can increase appreciably more. For instance, one sees that in the vicinity of $x = -8$ that the current density has increased by an amount on the order of 25 to 30% of its value at $t = 130\,t_A$. While a portion of that increase likely arises from the overall increase in the current density with time, a portion of the increased value of the current density arises from the local thinning of the current sheet in that vicinity.

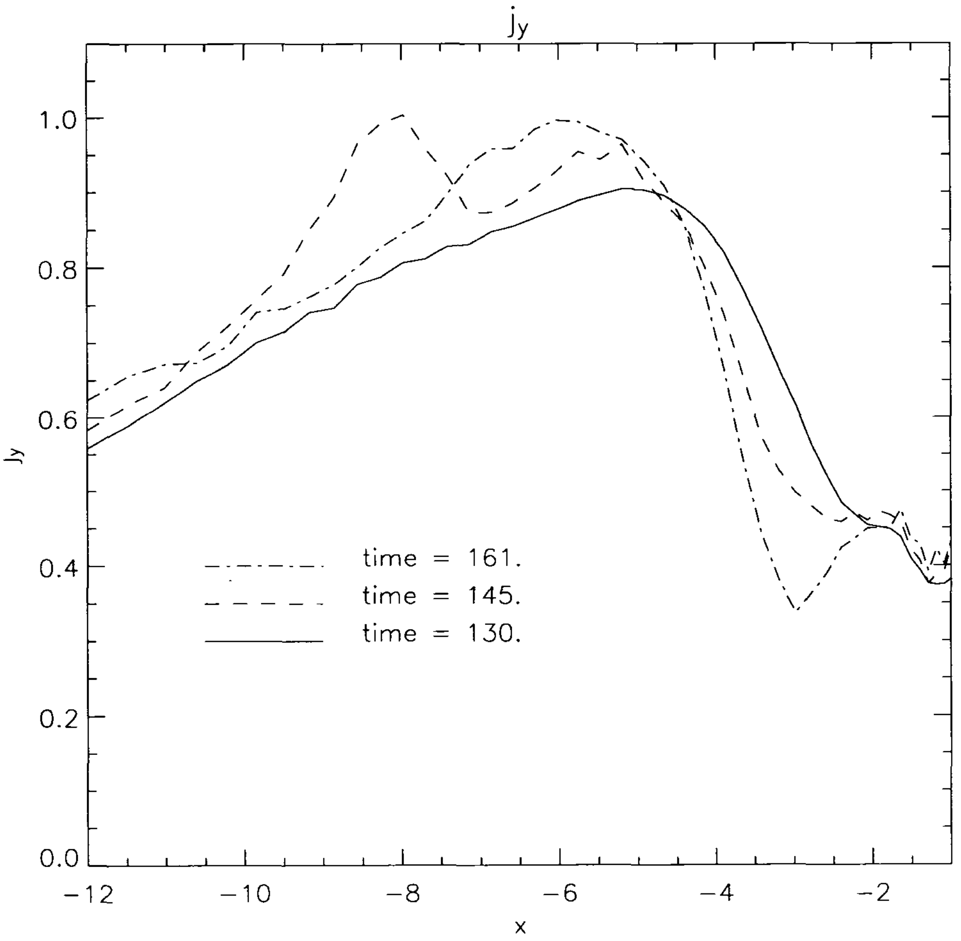

Figure 4.10. Current density along the noon-midnight meridian. The dominant component of the current density, j_y, in the range $-12 \leq x \leq -1$ in the equatorial plane ($z = 0$) for the times 130, 145, and 161 t_A.

It is instructive to examine the behavior of the current density in the equatorial plane over time, as illustrated in Figure 4.11. This figure shows j_y, the dominant component of the current density, in the equatorial plane at 130, 145, and 161 t_A. One sees that the maximum of the current density at $t = 130\,t_A$ lies near $x = -5$ along the noon-midnight meridian. By $t = 145\,t_A$, the maximum has moved to the vicinity of $x = -8$. The profile of the current density in the equatorial plane has changed at this time, reflecting the influence of the slow shock. Note, however, that the current density in the vicinity of $x = -5$ has still increased. At $t = 161\,t_A$, one sees that the overall maximum of the current density once again lies near $x = -5$. The influence of the slow shock is not readily seen in the equatorial plane at $t = 161\,t_A$. However, examination of Figure 4.8 reveals its presence, even then, at larger values of z. In the end, I find that the current density in the flux reservoir increases by approximately 11% in the course of the simulation.

The slow shock can still be seen in the bottom panel of Figure 4.8 (corresponding to $t = 161\,t_A$), although it is no longer coincident with the region of maximum current density. The current along the shock is still relatively strong. Its presence, along with the intense current density near the equatorial plane, can account for reports of bifurcated current sheets (as reported by *Nakamura et al.* [2002], *Runov et al.* [2003], and *Sergeev et al.* [2003]). However, this more complicated current sheet structure also complicates interpretations of the thickness of the current sheet.

4.3 Estimate of Current Sheet Thinning Time Scale

In Section 1.5 (also see Appendix E) I estimated the time needed to evacuate the magnetic flux reservoir to be roughly 30 minutes. However, this estimate did not directly address the current sheet thinning and assumes that our hypothesis for current sheeting thinning in fact applies. The actual dynamics of from our simulation results in this chapter provide a more direct measure of the typical time for current sheet thinning.

Consider the plots of the velocity at the time $t = 161\ t_A$ in the planes $z = 0.33$, $z = 0.55$, and $z = 0.98$ shown in Figure 4.12. One sees extended regions of downward flow—roughly from $-6.5 < x < -3.8$ and $-9 < y < +9$—just tailward of the flow channel (blue and dark blue colors). This flow converges toward the equatorial plane. Consider the minimum values of v_z in the Figure 4.12, given by the minimum value on the color bars. The minimum

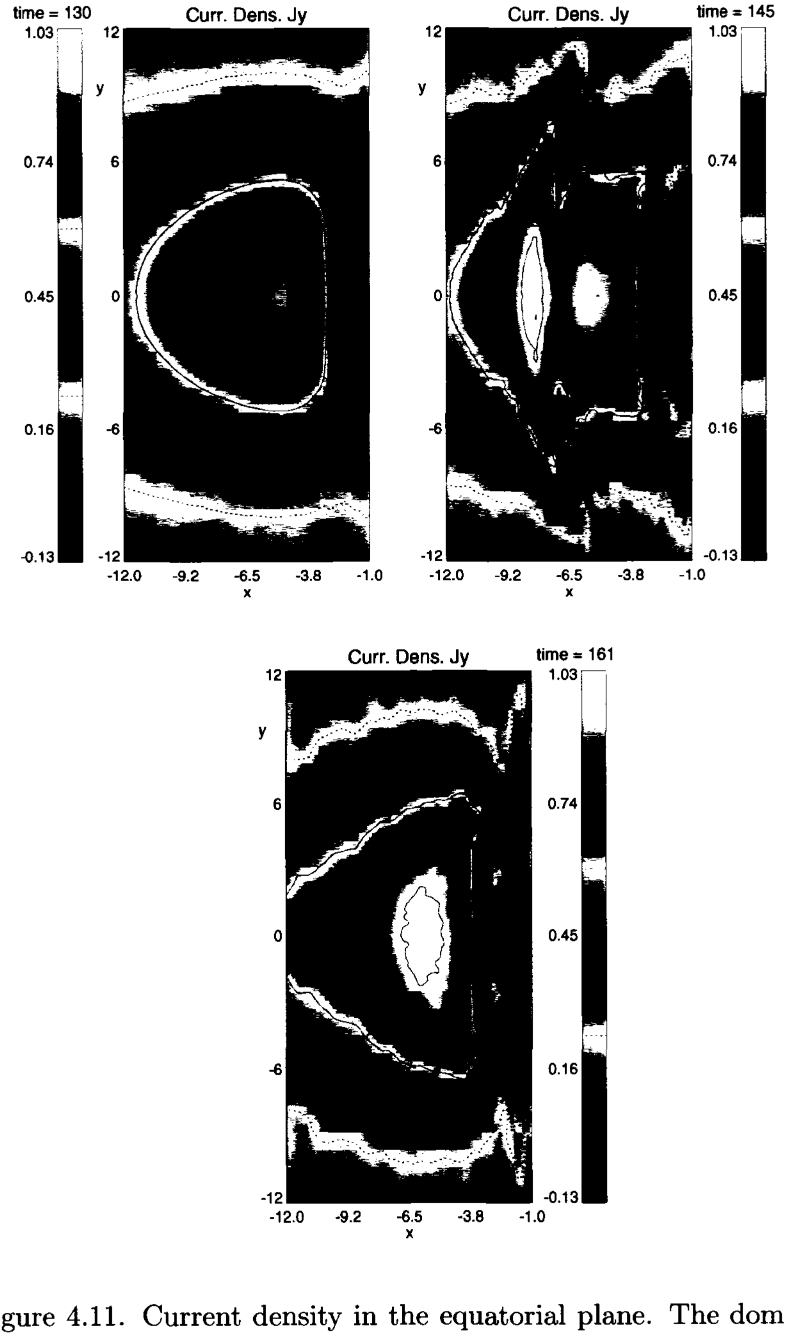

Figure 4.11. Current density in the equatorial plane. The dominant current density component, j_y, in the equatorial plane at 130, 145, and 161 t_A.

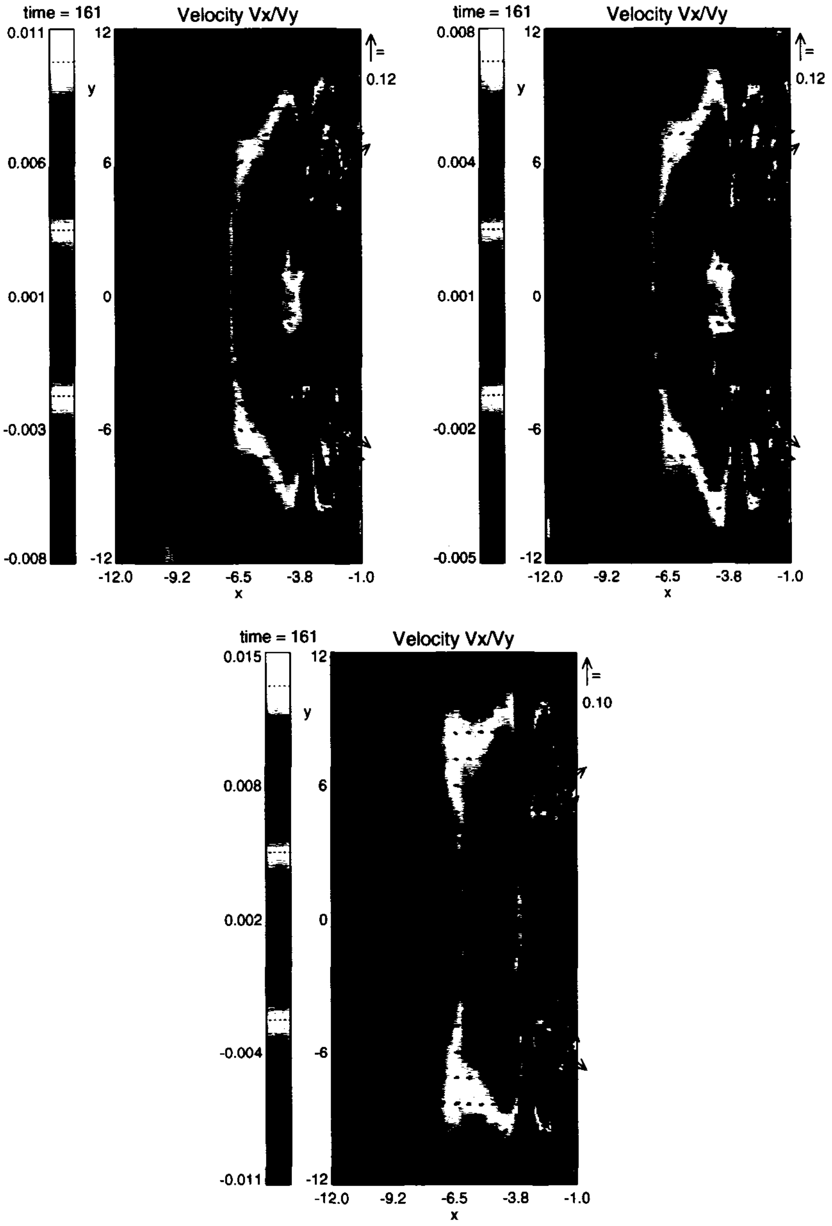

Figure 4.12. Velocity in planes above the equatorial plane. The velocity at $t = 161\ t_A$ at three different values of z. The upper left plot shows the velocity in the plane $z = 0.33$. The upper right plot shows the velocity in the plane $z = 0.55$. The bottom plot shows the velocity in the plane $z = 0.98$. The same conventions in Figure 4.2 are used here.

values of v_z produce the plot akin sketched in Figure 4.13. This implies for the motion of plasma elements that

$$v_z = \frac{dz}{dt} = sz, \tag{4.24}$$

where s is the slope in Figure 4.13. Introducing the constant $t_c = -\frac{1}{s}$, this equation becomes

$$\frac{dz}{dt} = -\left(\frac{1}{t_c}\right) z, \tag{4.25}$$

with the solution

$$z(t) = z_0 \exp\left(-\frac{t}{t_c}\right). \tag{4.26}$$

Here z_0 is a constant of integration. Using the minimum values of v_z in Figure 4.12, as well as the value of $v_z = 0$ at $z = 0$ (required by the magnetotail symmetry discussed in Section), and calculating a best fit for the slope, I obtained a characteristic time constant of $t_c \simeq 82\ t_A$, which corresponds to ~20 minutes. Thus t_c can be interpreted as the e-folding time for current sheet thinning. Note that in $t = t_c = 40$ minutes the current sheet thins by a factor of $e^2 \approx 7.4$. If the current sheet originally has a thickness of 4 R_E, it has a thickness of $sim0.54$ R_E at the end of that time. This result is also a quantitative confirmation that the proposed mechanism indeed works and leads to a time scale for current sheet thinning compared to the one based on the magnetic flux transport. Note that this time scale is also comparable to the duration of the growth phase and the earlier estimate of the time needed to evacuate the magnetic flux reservoir (in Section 1.5 and Appendix E).

4.4 Discussion and Summary

This chapter concerned the outflow boundary condition applied to the Earthward boundary of the simulation described in Chapter 3 and the resulting dynamics of the system. It began with a discussion of the outflow boundary condition itself, addressing in turn

- the specification of an azimuthal velocity profile in the equatorial plane, and
- the mapping of that profile to the Earthward boundary along magnetic field lines.

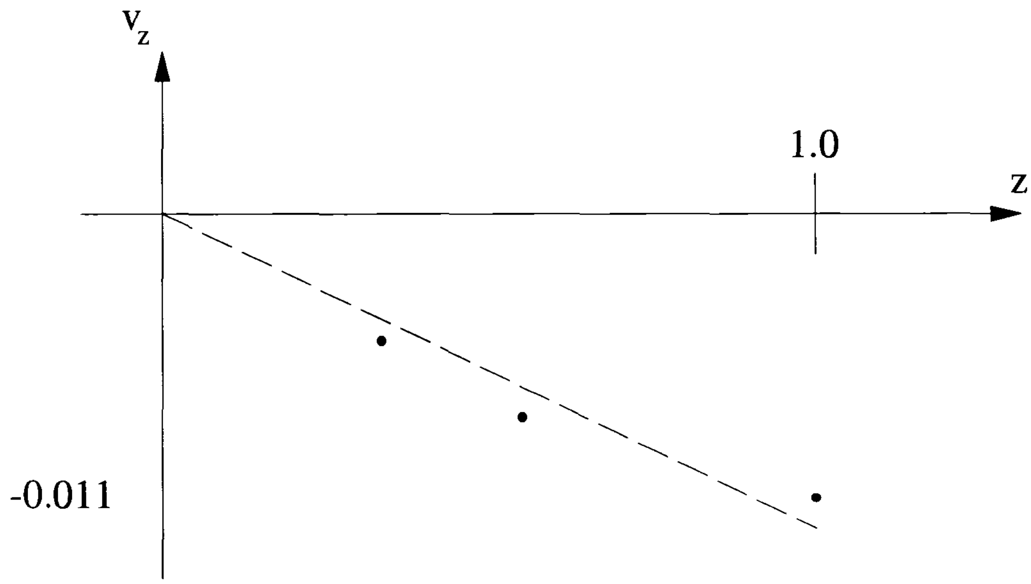

Figure 4.13. Minimum v_z versus z. A sketch of the dependence of the minimum value of v_z as a function of z for the planes shown in Figure 4.12.

I then examined the velocity profile and found that it had the characteristics that we would expect to model the evacuation of magnetic flux from a limited region in the near-Earth magnetotail. I found that, indeed, the magnetic flux decreased appreciably in the expected location of our 'magnetic flux reservoir.' An unexpected consequence of the evacuation of this flux reservoir was the establishment of a feature, especially apparent in the current density and velocity, that I interpret as a slow shock.

This structure can carry ~6% of the total cross-tail current. Note also that the width of this structure is only a few grid points, i.e., limited in the simulation by the resolution. In reality, although this structure carries only a fraction of the cross-tail current its thickness could be much smaller (on the order of ~600 km) with a correspondingly higher current density, with possible implications for the onset of micro-instabilities and/or magnetic reconnection. This feature can also mask, at intermediate times, the intensification of the current density in the equatorial plane that we would expect from current sheet thinning. The intense current density associated with this slow shock, coupled with the intensified current density in the equatorial plane, might serve as an explanation of observations of bifurcated current sheets in the growth phase, when I expect the treatment of the magnetosphere using ideal MHD to still be useful.

The maximum global intensification is about 20%, with values of over 30% for the local current increase. This actually corresponds to a significantly more pronounced thinning than apparent at first glance. Note that the simulation does not contain the typical increase of the lobe magnetic field of 10 to 20% (caused by accumulation of magnetic flux from the dayside). Vice versa, the removal of flux through outflow actually lowers the lobe magnetic field in the near-Earth tail by ~5 to 10%. Thus the current density increase in the simulation underestimates the actual increase by probably 10 to 20%.

Consideration of the minima values of v_z as a function of z allows the estimate of a time scale of current sheet thinning, $t_c \simeq 82\ t_A \simeq 20$ minutes, that is comparable to growth phase time scales.

The duration of the case discussed here was limited because of numerical instability. I did generate cases which ran longer. Figure 4.14, Figure 4.14, and Figure 4.15 show, respectively, the magnetic field at the Earthward boundary, the velocity just above the equatorial plane, and the current density in the noon-midnight meridian for a case that ran for about 20 t_A longer than the case discussed earlier. One sees that in Figure 4.14 that the depletion of magnetic flux is even more pronounced than it was in Figure 4.4. Figure 4.15 shows us that there is a small amount of flow from further tailward—still small, but not zero as was the case in Figure 4.2. Figure 4.16 demonstrates that the current density continues to increase as the code is run longer. But this extra time came at a price. In order to increase the stability of the code, I added a localized distribution of viscosity. Although the code ran longer, the viscosity masks the dynamics of the slow shock structure, which is not evident at all in Figure 4.16. The importance of the slow shock to the dynamics leads me to believe that this cost of increased stability may be too high.

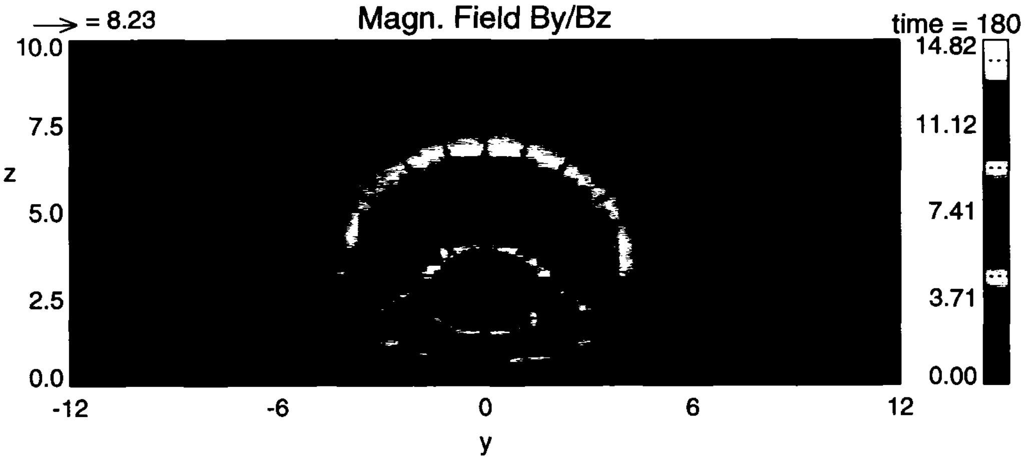

Figure 4.14. Magnetic field at the Earthward boundary for an especially long-running case. The magnetic field at the Earthward boundary at $t = 180\,t_A$ for a case that ran for especially long time. The same convention used in Figure 3.8 is used here. Arrows show the direction of the tangential magnetic field $\mathbf{b}_t = b_y\mathbf{e}_y + b_z\mathbf{e}_z$, while colors give the value of the normal magnetic field component b_x.

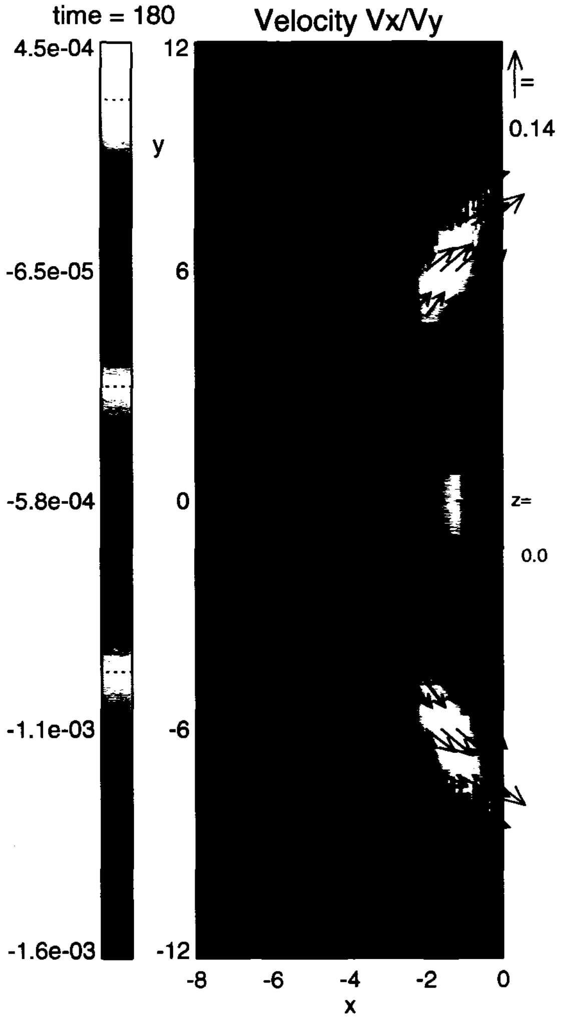

Figure 4.15. Velocity profile immediately above equatorial plane for an especially long-running case. The imposed velocity profile in the plane $z = 0.03$, just above the equatorial plane, at $t = 180 t_A$ for the case corresponding to Figure 4.14. The arrows represent the tangential velocity $\mathbf{v}_t = v_x \mathbf{e}_x + v_y \mathbf{e}_y$. The colors represent the value of the normal velocity component v_z.

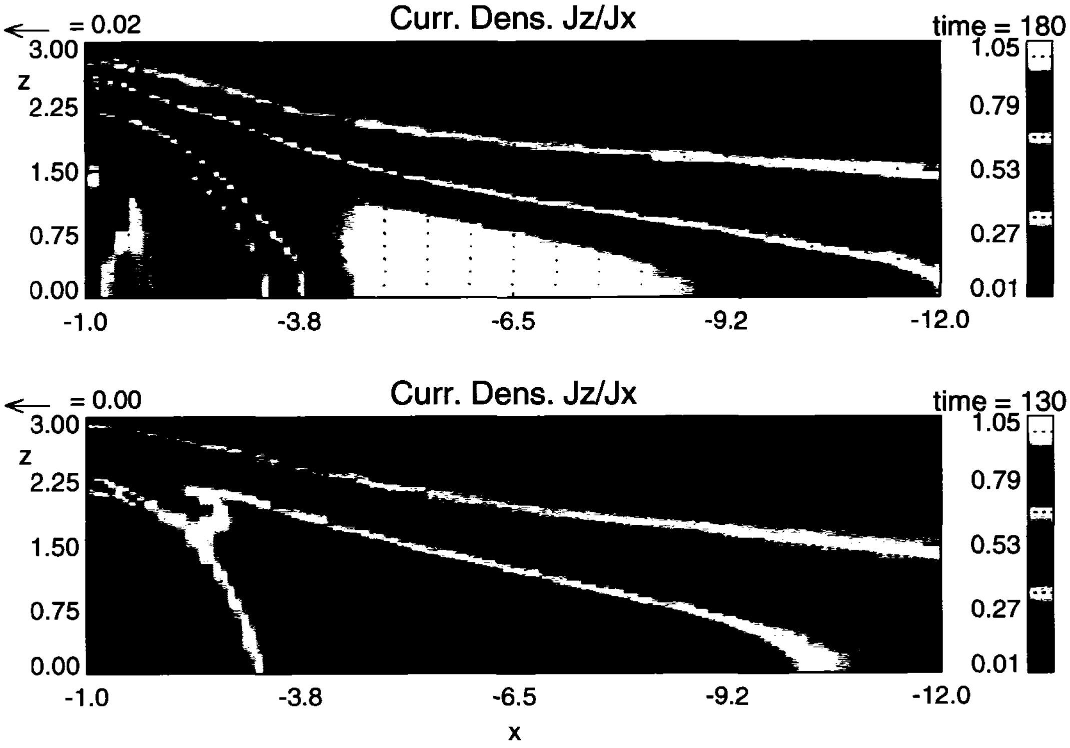

Figure 4.16. Comparison of the current density in the noon-midnight meridian. The top panel shows the current density for the case shown in Figure 4.14 and Figure 4.15. The bottom panel shows the current density at the end of the relaxation for the case discussed earlier in the chapter for comparison. The same conventions in Figure 4.8 are used here.

Chapter 5

Summary and Conclusions

5.1 Proposed Model for Current Sheet Thinning During the Growth Phase of Magnetospheric Substorms

Current sheet thinning is recognized (*McPherron et al.* [1987], *Sergeev et al.* [1990], *Sanny et al.* [1994], *Thompson et al.* [2005]) as a critical process in the dynamics of the magnetospheric substorm. It is a characteristic property of the slow, steady evolution of the magnetosphere during the growth phase, during which a portion of the bulk kinetic energy of the solar wind is transformed into and stored as magnetic field energy in the magnetotail lobes. Current sheet thinning establishes the conditions for the onset of the expansion phase, and an explanation for current sheet thinning is fundamentally important for the understanding of the physical mechanism responsible for the onset of the expansion phase with its rapid evolution during which the stored energy is released.

This dissertation has examined a mechanism for current sheet thinning. **I propose that current sheet thinning occurs because of the evacuation of the near-Earth flux reservoir by convection to replace magnetic flux that is eroded on the dayside.** Unlike two other possible mechanisms (*Schindler and Birn* [1993] and *Lee et al.* [1998]), my hypothesis is able to predict basic properties of current sheet thinning, such as the location, temporal evolution, and dynamics of this process. The slow, quasi-static convection of the plasma during the growth phase constrains the location and downtail extent of this 'magnetic flux reservoir.' As magnetic flux is removed from this region, the magnetic field becomes increasingly tail-like. This evolution of the magnetic field leads to the development and thinning of the current sheet in the near-Earth magnetotail.

5.2 Three-Dimensional Magnetic Field and Plasma Constraints for Adiabatic Convection

The slow, quasi-static convection of plasma during the growth phase justifies the assumption that this convection is adiabatic. Accordingly, the plasma moves largely along contours of the specific entropy. For prescribed models of the magnetic field and the plasma pressure, I calculated the distribution of the specific entropy for magnetic flux tubes passing through the equatorial plane. Using such maps, one can determine the region in the magnetotail that maps to the dayside magnetopause. Only from that region in the magnetotail can magnetic flux tubes convect adiabatically to replace magnetic flux that is eroded on the dayside magnetopause due to magnetic reconnection there. Using the *Tsyganenko* [1996] semi-empirical magnetic field model, I confirmed that the magnetopause maps to a region in the near-Earth magnetotail that coincides with the region in which current sheet thinning is indeed observed. I varied the input parameters of our model— that serve as input to the Tsyganenko-96 model on which our model is based—to study the effect of these variations on our mapping. I found, for a considerable range of the input parameters (the solar wind dynamic pressure P_{dyn}, IMF B_y and B_z, and the activity index D_{st}) considered (appropriate for a quiet magnetosphere), that the specific entropy at a given distance downtail varied by no more than about a factor of two and the variation in the input parameters does not significantly alter the location of the region in which I expect the magnetic flux depletion and the corresponding current sheet thinning.

I concluded the second chapter by considering the constraints on adiabatic convection. In particular, I considered the loss of particles out of the ionospheric end of magnetic flux tubes during adiabatic convection. I found that the resulting energy flux is inconsistent with auroral observations. Accordingly, the magnetic flux eroded from the dayside magnetopause cannot be replaced by magnetic flux from the middle and far magnetotail. It can only be replaced by magnetic flux from a limited region of the near-Earth magnetotail.

5.3 3D MHD Model—Properties

A model of the mechanism for current sheet thinning should take into account the evolution of the system as the 'magnetic flux reservoir' is depleted. I introduced such a time-dependent MHD model in Chapter 3, describing the simulation domain, the governing equations, their numerical discretization, and the boundary conditions of our simulation.

My model was formed through the combination of the 3D MHD code of *Otto* [1990] with the semi-empirical magnetic field model of *Tsyganenko* [1996]. Although this approach allows me to start with a realistic magnetic field, the resulting configuration is not an equilibrium configuration. I used the 'ballistic relaxation' technique of *Hesse and Birn* [1993] to obtain an equilibrium configuration from which I could start the model of our mechanism for current sheet thinning. This relaxation process resulted in the reduction of the force norm, an integral measure of the unbalanced forces in the system, of several orders of magnitude.

I concluded the chapter by examining the configuration of the initial equilibrium state to which I would apply a boundary condition to model the removal of magnetic flux from the near-Earth magnetotail. The resulting configuration does indeed exhibit the characteristics of a magnetosphere. In particular, the current layer structure is realistic, with a well-defined edge. Its intensity and thickness as functions of downtail distance look realistic. I can use the available tools to examine field-aligned currents. However, I found that the distribution of field-aligned currents depends sensitively on the pressure distribution.

5.4 3D MHD Model—Outflow Boundary Condition and Results

The fourth chapter began with a description of the outflow boundary condition applied at the Earthward boundary. This boundary condition resulted from the imposition of a divergent flow from the near-Earth magnetotail. I found it insufficient to just prescribe an arbitrary outflow profile at this boundary. Rather, the flow profile needed to be chosen carefully by taking into account how the magnetic field maps from the Earthward boundary into the equatorial plane. By implementing such a map assuming a rigid angular motion of magnetic field lines, I was able to prescribe the outflow in a much more stable way.

I then turned to consideration of the resulting evolution of the system. I chose to discuss in detail the features of a representative run. I found that the velocity profile near the equatorial plane was consistent with the outflow profile that I had hypothesized would be established in the equatorial plane, even though the boundary condition was only applied to the Earthward boundary. I found that this outflow resulted in the removal of a considerable amount of magnetic flux in the near-Earth magnetotail.

I observed a global increase of the current density to 111 to 113% of its maximum value at the start of the outflow. Although the global maximum of the current density reached its maximum at an intermediate time in the simulation and then began to decrease, I continued to observe the local increase of the current density in the region of the flux reservoir.

A more surprising development was the evolution of a structure, readily visible in the current density and velocity, that I interpreted as a slow shock. This feature resulted in a concentration of the current that, at times, was more intense than the increasing current near the equatorial plane. I interpret the slow shock as the mechanism through which the outflow boundary condition is communicated in the plasma. I argue that the current associated with this slow shock may explain observation of bifurcated current sheets during the growth phase, without requiring magnetic reconnection or other non-ideal MHD processes. Furthermore, it masked the continued local increase in the current density along the equatorial plane in the vicinity of the magnetic flux reservoir. This feature also complicates considerations of the thickness of the current sheet. For example, fitting a simple Harris sheet model to a current sheet with such complicated structure may prove to be misleading.

Consideration of the minima values of v_z as a function of z allows the estimate of a time scale of current sheet thinning, $t_c \simeq 82\ t_A \simeq 20$ minutes, that is comparable to growth phase time scales.

5.5 Discussion of Main Results

I have proposed a new mechanism for current sheet thinning during the late growth phase of magnetospheric substorms. By this mechanism, current sheet thinning occurs because of the evacuation of the near-Earth flux reservoir by convection to replace magnetic flux that is eroded on the dayside. In contrast to other mechanisms (*Schindler and Birn* [1993] and *Lee et al.* [1998]), this mechanism provides a causal explanation for the observed current sheet thinning and magnetic reconnection at the dayside magnetopause. The new mechanism provides predictions on the location, duration, and dynamical evolution of current sheet thinning.

I examined this new mechanism both conceptually and quantitatively. My conceptual considerations enabled the prediction of the location of current sheet thinning. This location is largely independent of the detailed state of the magnetosphere. I was able to predict the duration of the growth phase to within a factor of two simply by considering the amount of time needed to deplete the proposed 'magnetic flux reservoir' in the near-Earth magnetotail. I examined this mechanism quantitatively through the use of a three-dimensional ideal MHD simulation. I did not observe the drastic reduction in the thickness of the current sheet; numerical instabilities terminated my simulation too soon. But the results demonstrate the global increase of the current density in the magnetic flux reservoir, despite the removal of magnetic flux—which one would otherwise expect to lead to a decrease of current—as well as even greater local increases in current. The increase in current density and thinning are found to be consistent with the amount of flux that we removed from the system. Since I did not incorporate the observed increase in the magnetotail lobe flux in my simulation, I would expect that the results underestimate the increase in the current density by 20 to 30%. For that reason, the increase in the current that I see in my simulation is even more significant. I have also examined the detailed dynamics of current sheet thinning. In doing so, I have found a new explanation for the very thin bifurcated current sheets that have been reported in recent publications (*Nakamura et al.* [2002], *Runov et al.* [2003], *Sergeev et al.* [2003]). This sheds light on the evolution of the current sheet thinning.

There remain avenues along which this research can continue. I believe that I will be able to observe drastic current sheet thinning if I can extend the duration of the simulations run for another five to ten minutes—twenty to forty more Alfvén times. I hope that further work will soon yield this additional time. The detailed implementation of the outflow boundary condition on the Earthward boundary (for example, the frequency with which that boundary condition is updated) may yield better performance. In addition, the parameter space associated with this model lends itself to a more detailed study. Recent modifications featuring improved pressure distributions may also prove to be more successful. Another important extension of the current work would be the inclusion of Hall physics. This addition becomes particularly important for thin current sheets where gradients occur on the ion inertial scale, which is $\sim$100 km in the central plasma sheet.

In summary, while I was unable to demonstrate drastic thinning for the stated reasons, the observed results are fully consistent with the proposed physical mechanism. In addition, the detailed dynamics of current sheet splitting (or bifurcation) may prove to be highly relevant for the expansion phase onset. The great promise of this research suggests that it should be continued.

Appendix A

Local Conservation of Entropy

This appendix provides two derivations of the local conservation of entropy.

A.1 Derivation utilizing the first law of thermodynamics and the ideal gas law

Consider a plasma parcel. The first law of thermodynamics can be expressed in the form (*Marion and Hornyak* [1982])

$$dQ = dU + P\,dV, \tag{A.1}$$

where dQ is the differential heat added to the parcel, dU is the differential change in the internal energy of the parcel, and $P\,dV$ is the differential work done by the parcel. The thermal pressure is represented by P, as elsewhere in the text; but here V is the volume of the parcel.

Let us consider what happens if heat is added to the parcel while the volume of the parcel is held fixed. In that case the second term of Equation A.1 vanishes (since $dV = 0$), and the added heat is used solely to change the internal energy of the system. In that case I can write

$$dQ = nC_v\,dT = dU, \tag{A.2}$$

where

$$C_v = \left(\frac{1}{n}\right)\left(\frac{dQ}{dT}\right)\bigg|_V \tag{A.3}$$

is the molar specific heat at constant volume. The subscript V in the expression above indicates that the derivative $\frac{dQ}{dT}$ is evaluated at constant volume V. I can then use Equation A.2 to write Equation A.1 in the form

$$dQ = nC_v\,dT + P\,dV. \tag{A.4}$$

I next turn to the ideal gas law, which can be expressed in the form (*Marion and Hornyak* [1982])

$$PV = nRT, \tag{A.5}$$

where n is the number of moles in the parcel, R is the universal gas constant $[R = 8.3144\, J \cdot (mole \cdot K)^{-1}]$, and T is the temperature. (Note that n is serving in a role analogous to mass here.) Presuming that I can treat n as fixed, I can rewrite the ideal gas law in the differential form

$$n\, dT = \left(\frac{1}{R}\right)(P\, dV + V\, dP). \tag{A.6}$$

I can use Equation A.6 and much algebraic manipulation to recast Equation A.4 in the form

$$dQ = nC_v T \left[\frac{dP}{P} + \gamma\left(\frac{dV}{V}\right)\right]. \tag{A.7}$$

The quantity γ is defined as

$$\gamma = \frac{C_p}{C_v}, \tag{A.8}$$

where

$$C_p = \left(\frac{1}{n}\right)\left(\frac{dQ}{dT}\right)\bigg|_P \tag{A.9}$$

is the molar specific heat at constant pressure. The subscript P in the expression above indicates that the derivative $\frac{dQ}{dT}$ is evaluated at constant pressure P. Note that γ, the ratio of specific heats, is also called the adiabatic index or the polytropic index. I can write

$$dQ = nC_v T \left\{d\left[\ln(P)\right] + d\left[\ln\left(V^\gamma\right)\right]\right\} \tag{A.10}$$

or

$$dQ = nC_v T\, d\left[\ln\left(PV^\gamma\right)\right]. \tag{A.11}$$

The entropy is defined as

$$ds = \frac{dQ}{T}. \tag{A.12}$$

I have, then

$$ds = nC_v\, d\left[\ln\left(PV^{\gamma}\right)\right] \tag{A.13}$$

and

$$s = C_v\, \ln\left(PV^{\gamma}\right). \tag{A.14}$$

I will work in terms of the more convenient quantity

$$S' = \exp\left(\frac{S}{nC_v}\right) = PV^{\gamma}. \tag{A.15}$$

For adiabatic changes, $ds = 0$ and I can write

$$nC_v \left\{d\left[\ln\left(PV^{\gamma}\right)\right].\right\} = 0 \tag{A.16}$$

Since nC_v is generally non-zero, I find that PV^{γ} is constant. I can express the conservation of this quantity under adiabatic changes by writing

$$\frac{d}{dt}\left(PV^{\gamma}\right) = \frac{\partial}{\partial t}\left(PV^{\gamma}\right) + \mathbf{u}\cdot\nabla\left(PV^{\gamma}\right) = 0. \tag{A.17}$$

With the realization that the volume V is inversely proportional to the mass density ρ,

$$V \propto \frac{1}{\rho}, \tag{A.18}$$

I can express the local conservation of entropy in the following form:

$$\frac{d}{dt}\left(P\rho^{-\gamma}\right) = 0. \tag{A.19}$$

A.2 Derivation utilizing the continuity equation and the pressure equation

Let us begin by considering the quantity

$$S = P^{\alpha}\rho^{\beta}. \tag{A.20}$$

For what values of α and β is the full time derivative of this quantity equal to zero? That is, for what values of α and β does the following hold?

$$\frac{d}{dt}\left(P^{\alpha}\rho^{\beta}\right) = 0 \tag{A.21}$$

I can expand this full time derivative and write this condition as

$$\frac{\partial}{\partial t}\left(P^{\alpha}\rho^{\beta}\right) + \mathbf{v}\cdot\nabla\left(P^{\alpha}\rho^{\beta}\right) = 0. \tag{A.22}$$

I can use the chain rule to write

$$\frac{\partial}{\partial t}\left(P^{\alpha}\rho^{\beta}\right) = \beta P^{\alpha}\rho^{\beta-1}\left(\frac{\partial\rho}{\partial t}\right) + \alpha P^{\alpha-1}\rho^{\beta}\left(\frac{\partial P}{\partial t}\right). \tag{A.23}$$

Similarly,

$$\nabla\left(P^{\alpha}\rho^{\beta}\right) = \beta P^{\alpha}\rho^{\beta-1}\nabla\rho + \alpha P^{\alpha-1}\rho^{\beta}\nabla P. \tag{A.24}$$

Substituting these expressions into Equation A.22, I obtain

$$\beta P^{\alpha}\rho^{\gamma-1}\left(\frac{\partial\rho}{\partial t} + \mathbf{v}\cdot\nabla\rho\right) + \alpha P^{\alpha-1}\rho^{\beta}\left(\frac{\partial P}{\partial t} + \mathbf{v}\cdot\nabla P\right) = 0. \tag{A.25}$$

To proceed further, I shall make use of the mass continuity equation

$$\frac{\partial\rho}{\partial t} + \nabla\cdot(\rho\mathbf{v}) = 0 \tag{A.26}$$

and the pressure equation

$$\frac{\partial P}{\partial t} + \nabla\cdot(P\mathbf{v}) = (1-\gamma)\,P\,(\nabla\cdot\mathbf{v})\,. \tag{A.27}$$

(Equation A.26 is simply Equation 1.1 recast in a slightly different form, whereas Equation A.27 is Equation 1.4, recast in a slightly different form, with $\eta = 0$.) Expanding the second term on the left-hand side of Equation A.26, I rewrite it as

$$\frac{\partial\rho}{\partial t} + \mathbf{v}\cdot\nabla\rho = -\rho\,(\nabla\cdot\mathbf{v})\,. \tag{A.28}$$

Similarly, I can rewrite Equation A.27 in the form

$$\frac{\partial P}{\partial t} + \mathbf{v}\cdot\nabla P = -\gamma P\,(\nabla\cdot\mathbf{v})\,. \tag{A.29}$$

Substituting these expressions into Equation A.25, I obtain

$$(\beta + \alpha\gamma) P^{\alpha} \rho^{\beta} (\nabla \cdot \mathbf{v}) = 0. \tag{A.30}$$

Since $P^{\alpha} \rho^{\beta} (\nabla \cdot \mathbf{v})$ is generally non-zero, I must have

$$\beta + \alpha\gamma = 0. \tag{A.31}$$

Therefore

$$\beta = -\alpha\gamma. \tag{A.32}$$

This expression constrains the ratio of β and α, if not their actual values. However, I appeal to simplicity and chose to set $\alpha = 1$. In that case,

$$\beta = -\gamma. \tag{A.33}$$

In this case, then, I find that the conserved quantity is

$$S = P\rho^{-\gamma}. \tag{A.34}$$

Again, this quantity is conserved:

$$\frac{d}{dt} \left(P\rho^{-\gamma} \right) = 0. \tag{A.35}$$

Appendix B

The differential magnetic flux tube volume

Now let us consider the magnetic flux tube depicted in Figure B.1. I can calculate its volume $\widetilde{V}$ by evaluating the expression

$$\widetilde{V} = \int_{\ell_1}^{\ell_2} d\ell \int\int_{A_c} dA. \tag{B.1}$$

Here $d\ell$ is a differential element of length along the magnetic field; ℓ_1 and ℓ_2 denote the positions of the ionospheric footpoints of the flux tube. (This equation has practical utility only if one defines this volume for closed magnetic flux tubes.) A_c is the cross-sectional area of the flux tube, whereas dA is a differential element of that area. With this notation, one would write the magnetic flux corresponding to the flux tube as

$$\Phi_0 = \int\int_{A_c} \mathbf{B} \cdot \mathbf{e}_n \, dA, \tag{B.2}$$

where $\mathbf{B}$ is the magnetic induction and $\mathbf{e}_n$ is the unit normal to the cross-sectional area. If the flux tube is small enough that the magnetic field can be considered to be reasonably constant over the cross-sectional area of the flux tube, one can write

$$\Phi_0 \approx A_0 B_0, \tag{B.3}$$

where A_0 and B_0 are, respectively, the cross-sectional area of the flux tube and the magnitude of the magnetic field at some reference location—for these purposes, at one of the ionospheric footpoints.

Since the magnetic flux is constant along the magnetic flux tube, I can write

$$AB = A_0 B_0, \tag{B.4}$$

where A and B are, respectively, the cross-sectional area of the flux tube and the magnetic field magnitude in the flux tube in the equatorial plane. One can then write

$$A = \frac{A_0 B_0}{B} \tag{B.5}$$

or

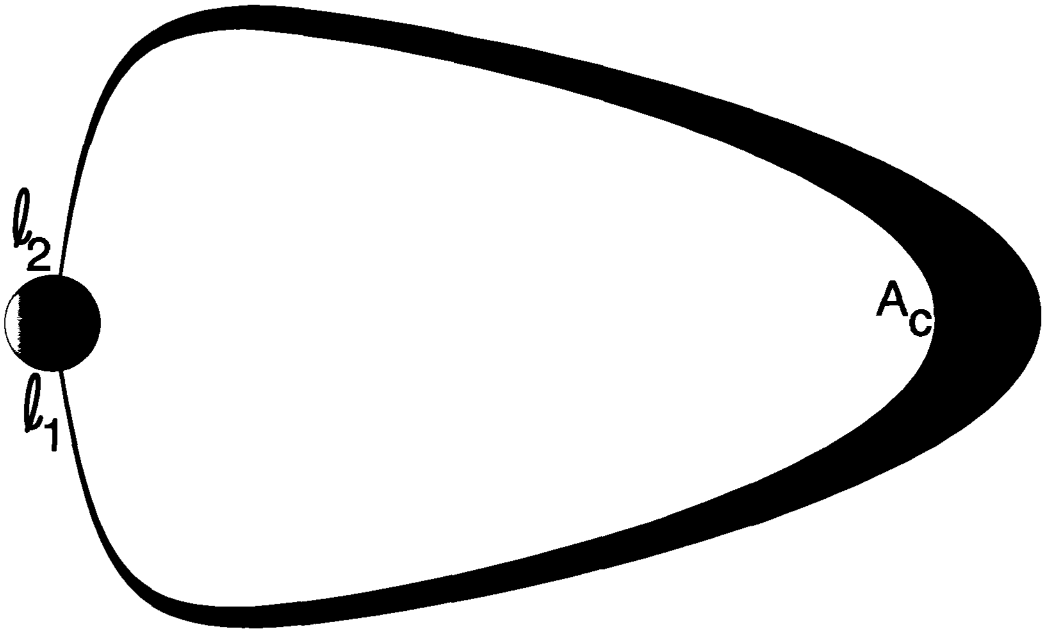

Figure B.1. Magnetotail flux tube. A closed magnetotail flux tube. The positions of the ionospheric ends of the flux tube are denoted by ℓ_1 and ℓ_2. The cross section of the flux tube in the equatorial plane is denoted by A_c.

$$A \propto \frac{1}{B}. \tag{B.6}$$

Now let us consider the limit as the cross-sectional area A_c of the flux tube becomes very small—essentially infinitesimal—so that the magnetic flux tube has essentially infinitesimal cross-sectional area. The flux tube now corresponds to a single magnetic field line. The area integral over A_c reduces to a quantity proportional to $\frac{1}{B}$. So one can write

$$\lim_{A_c \to 0} \int_{\ell_1}^{\ell_2} d\ell \int\int_{A_c} dA \propto \int_{\ell_1}^{\ell_2} \left(\frac{1}{B}\right) d\ell. \tag{B.7}$$

Now I can identify

$$V = \int_{\ell_1}^{\ell_2} \left(\frac{1}{B}\right) d\ell \tag{B.8}$$

as the volume of the flux tube per unit magnetic flux. As its name suggests, this quantity is simply related to the actual volume $\widetilde{V}$ of the flux tube:

$$V = \frac{\widetilde{V}}{\Phi_0}. \tag{B.9}$$

Since it depends only on the magnitude of the magnetic field along the flux tube, the volume per unit magnetic flux, V, is a very convenient quantity—sometimes more convenient than the actual volume $\widetilde{V}$ of the flux tube.

Appendix C

Derivation of the time rate of change of the particle number N on a magnetic flux tube

In considering the calculation of the ionospheric energy flux discussed in Chapter 2 and Appendix D, I find it useful to derive an expression for the time rate of change of the particle number N on magnetic flux tubes. This derivation results in an expression that can be applied to any quantity that is defined on a magnetic flux tube in the same manner as N. The number of particles N can be defined in terms of the number density n in the following manner:

$$N = \int_{\ell_1}^{\ell_2} d\ell \int\int_{A_c} n\, dA. \tag{C.1}$$

I have expressed N as an integral of its (volume) density n along the length of the flux tube (given by the coordinate ℓ, with the ends of the flux tube specified as ℓ_1 and ℓ_2) and over the cross-sectional area A_c of the flux tube.

This expression for N holds at any particular point in time. I now consider ΔN, the change in N from time t to time $t + \Delta t$. In doing so, I must consider

- changes in the positions of the endpoints ℓ_1 and ℓ_2 of the flux tube;
- changes in the cross-sectional area A_c of the flux tube; and
- changes in the integrand n.

I begin by writing

$$\Delta N = \Upsilon_1 + \Upsilon_2 + \Upsilon_3. \tag{C.2}$$

The three terms Υ_1, Υ_2, and Υ_3 correspond to the three contributions to ΔN described above.

The first contribution arises from changes in the position of the endpoints (and, therefore, of the length of the flux tube). It is given by

$$\Upsilon_1 = \int_{\ell_{1,t+\Delta t}}^{\ell_{2,t+\Delta t}} d\ell \int\int_{A_c} n\, dA - \int_{\ell_{1,t}}^{\ell_{2,t}} d\ell \int\int_{A_c} n\, dA. \tag{C.3}$$

Here $\ell_{1,t}$ and $\ell_{2,t}$ denote the positions of the ends of the flux tube at time t,whereas $\ell_{1,t+\Delta t}$ and $\ell_{2,t+\Delta t}$ denote the positions of the ends at time $t + \Delta t$. Since the area integral remains unchanged, I can write

$$\Upsilon_1 = \left(\int_{\ell_{1,t+\Delta t}}^{\ell_{2,t+\Delta t}} d\boldsymbol{\ell} - \int_{\ell_{1,t}}^{\ell_{2,t}} d\boldsymbol{\ell} \right) \int\int_{A_c} n \, dA. \tag{C.4}$$

The limits of the integrals over the length of the flux tube can be re-arranged to yield

$$\Upsilon_1 = \left(\int_{\ell_{2,t}}^{\ell_{2,t+\Delta t}} d\boldsymbol{\ell} - \int_{\ell_{1,t}}^{\ell_{1,t+\Delta t}} d\boldsymbol{\ell} \right) \int\int_{A_c} n \, dA. \tag{C.5}$$

The velocity $\mathbf{v}$ of one of the ends of the flux tube can be written as

$$\mathbf{v} = \frac{d\boldsymbol{\ell}}{dt}. \tag{C.6}$$

So

$$d\boldsymbol{\ell} = \mathbf{v} \, dt, \tag{C.7}$$

and I can write

$$\Upsilon_1 = \left(\mathbf{v}_2 \int_{t}^{t+\Delta t} dt' - \mathbf{v}_1 \int_{t}^{t+\Delta t} dt'' \right) \cdot \int\int_{A_c} n \, d\mathbf{A}, \tag{C.8}$$

where $\mathbf{v}_1$ and $\mathbf{v}_2$ are, respectively, the velocities of the endpoints denoted by ℓ_1 and ℓ_2, and the vector area element

$$d\mathbf{A} = \mathbf{e}_n \, dA \tag{C.9}$$

is defined in terms of its magnitude dA and the unit normal $\mathbf{e}_n$ to the flux tube surface. Since this contribution to ΔN occurs only at these endpoints, I can bring the area integral inside the parentheses (after evaluating the integrals in time) and write

$$\Upsilon_1 = \left(\int\int_{A_{\ell_1}} n\mathbf{v}_1 \cdot d\mathbf{A} \right) \Delta t + \left(\int\int_{A_{\ell_2}} n\mathbf{v}_2 \cdot d\mathbf{A} \right) \Delta t. \tag{C.10}$$

A_{ℓ_1} and A_{ℓ_2} are the areas at the ends of the flux tube located, respectively, at ℓ_1 and ℓ_2.

Now let turn our attention to Υ_2, the contribution to ΔN arising from the change in the cross-sectional area A_c of the flux tube from time t to time $t + \Delta t$. I can write

$$\Upsilon_2 = \int_{\ell_1}^{\ell_2} d\ell \int\int_{A_{c,t+\Delta t}} n\, dA - \int_{\ell_1}^{\ell_2} d\ell \int\int_{A_{c,t}} n\, dA, \tag{C.11}$$

where $A_{c,t}$ and $A_{c,t+\Delta t}$ denote the cross-sectional area of the flux tube at times t and $t+\Delta t$, respectively. I write

$$\Upsilon_2 = \int_{\ell_1}^{\ell_2} d\ell \left(\int\int_{A_{c,t+\Delta t}} n\, dA - \int\int_{A_{c,t}} n\, dA \right). \tag{C.12}$$

I shall restrict my attention, for a short while, to the area integrals. I define

$$\Lambda_1 = \int\int_{A_{c,t}} n\, dA \tag{C.13}$$

and

$$\Lambda_2 = \int\int_{A_{c,t+\Delta t}} n\, dA. \tag{C.14}$$

I also define their difference

$$\Delta\Lambda = \Lambda_2 - \Lambda_1 \tag{C.15}$$

$$\Delta\Lambda = \int\int_{A_{c,t+\Delta t}} n\, dA - \int\int_{A_{c,t}} n\, dA. \tag{C.16}$$

This difference is equal to the integral over the 'ribbon' R joining the surfaces $A_{c,t}$ and $A_{c,t+\Delta t}$. (Please refer to Figure C.1.) Accordingly, I could write

$$\Delta\Lambda = \int\int_{R} n\, dA. \tag{C.17}$$

Keeping in mind that the surface $A_{c,t+\Delta t}$ represents the evolution of the surface $A_{c,t}$ as the flux tube surface moves with velocity $\mathbf{v}$ over the time interval Δt, I define the vector differential area element over the surface R as

$$d\mathbf{A} = d\boldsymbol{\ell} \times d\mathbf{C}, \tag{C.18}$$

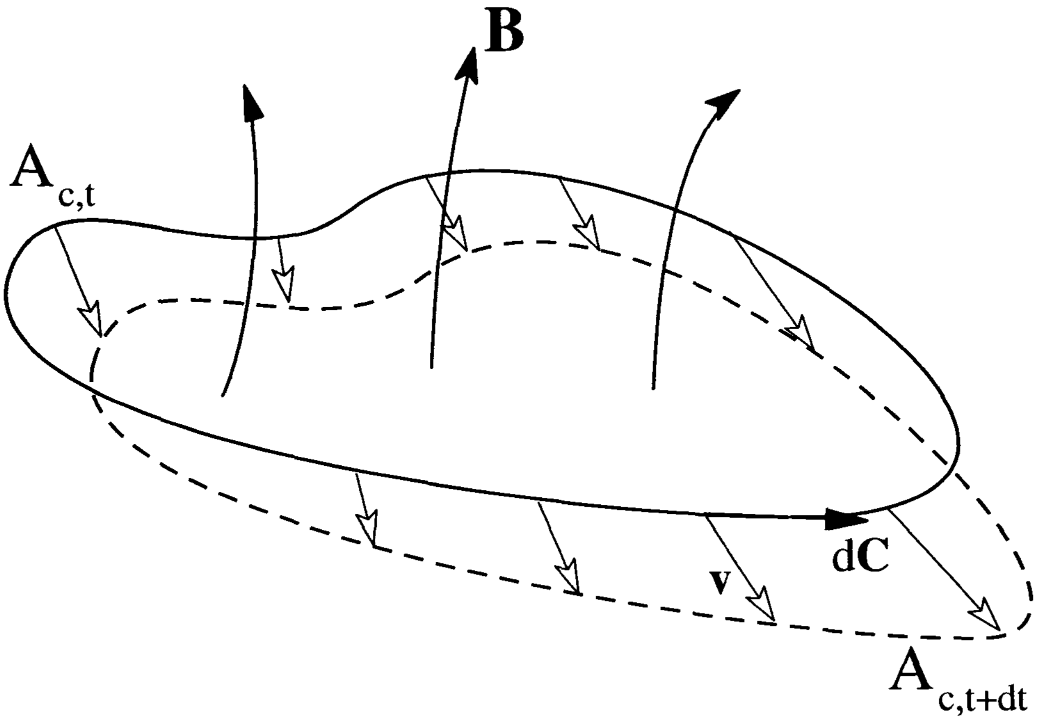

Figure C.1. The frozen-in flux condition. Depiction of the surfaces $A_{c,t}$ and $A_{c,t+\Delta t}$. The magnetic field **B**, velocity **v**, and vector length element dC are shown. The ribbon R joining the surfaces $A_{c,t}$ and $A_{c,t+\Delta t}$ is defined by Equation C.20.

where $d\boldsymbol{\ell}$ is the vector length element along the flux tube and $d\mathbf{C}$ is the vector length element along the edge of R. Using Equation C.7, I can write

$$d\mathbf{A} = \mathbf{v}\, dt \times d\mathbf{C} \tag{C.19}$$

$$d\mathbf{A} = (\mathbf{v} \times d\mathbf{C})\ dt. \tag{C.20}$$

I can write the magnitude of $d\mathbf{A}$ as

$$dA = v_n\, dC\, dt \tag{C.21}$$

if I define v_n as the component of $\mathbf{v}$ normal to the contour C bounding the surface R. I can now write

$$\Delta\Lambda = \oint_C dC \int_t^{t+\Delta t} n v_n dt'. \tag{C.22}$$

For a small enough time interval Δt, I can write

$$\Delta\Lambda = \left(\oint_C n v_n dC \right) \Delta t. \tag{C.23}$$

Now let us return to the expression for Υ_2. I have

$$\Upsilon_2 = \int_{\ell_1}^{\ell_2} (\Delta\Lambda)\ d\ell \tag{C.24}$$

$$\Upsilon_2 = \left(\int_{\ell_1}^{\ell_2} d\ell \oint_C n v_n dC \right) \Delta t. \tag{C.25}$$

Finally, let us consider Υ_3, the contribution to ΔN resulting in the change in the integrand n over the time interval Δt. It is given by

$$\Upsilon_3 = \int_{\ell_1}^{\ell_2} d\ell \int\int_{A_c} n_{t+\Delta t}\, dA - \int_{\ell_1}^{\ell_2} d\ell \int\int_{A_c} n_{t+\Delta t}\, dA. \tag{C.26}$$

Since both the integral along ℓ and the area integral over A_c remain unchanged in this term, I can write

$$\Upsilon_3 = \int_{\ell_1}^{\ell_2} d\ell \int\int_{A_c} (n_{t+\Delta t} - n_t)\, dA \tag{C.27}$$

or

$$\Upsilon_3 = \int_{\ell_1}^{\ell_2} d\ell \int\int_{A_c} (\Delta n)\, dA, \tag{C.28}$$

where I have defined

$$\Delta n = n_{t+\Delta t} - n_t. \tag{C.29}$$

The subscripts t and $t + \Delta t$ have again been used to denote the values of quantities at those times.

I am now ready to combine the expressions for Υ_1 (Equation C.10), Υ_2 (Equation C.25), and Υ_3 (Equation C.28). I obtain

$$\begin{aligned} \Delta N = \left(\int\int_{A_{\ell_1}} n\mathbf{v}_1\, dA\right) \Delta t + \left(\int\int_{A_{\ell_2}} n\mathbf{v}_2\, dA\right) \Delta t \\ + \left(\int_{\ell_1}^{\ell_2} d\ell \oint_C n v_n dC\right) \Delta t \\ + \int_{\ell_1}^{\ell_2} d\ell \int\int_{A_c} (\Delta n)\, dA. \end{aligned} \tag{C.30}$$

Dividing through by Δt yields the expression

$$\begin{aligned} \frac{\Delta N}{\Delta t} = \int\int_{A_{\ell_1}} n\mathbf{v}_1\, dA + \int\int_{A_{\ell_2}} n\mathbf{v}_2\, dA \\ + \int_{\ell_1}^{\ell_2} d\ell \oint_C n v_n dC \\ + \int_{\ell_1}^{\ell_2} d\ell \int\int_{A_c} \left(\frac{\Delta n}{\Delta t}\right) dA. \end{aligned} \tag{C.31}$$

Taking the limit as Δt approaches zero results in the expression

$$\begin{aligned}\frac{dN}{dt} = \int\!\!\int_{A_{\ell_1}} n\mathbf{v}_1\, dA + \int\!\!\int_{A_{\ell_2}} n\mathbf{v}_2\, dA \\ + \int_{\ell_1}^{\ell_2} d\ell \int\!\!\int_{A_c} \left(\frac{dn}{dt}\right) dA \\ + \int_{\ell_1}^{\ell_2} d\ell \oint_C n v_n dC.\end{aligned} \tag{C.32}$$

To proceed further, invoke local continuity of particle number and write the corresponding continuity equation

$$\frac{\partial n}{\partial t} + \nabla \cdot (n\mathbf{u}) = 0. \tag{C.33}$$

Note that $\mathbf{u}$ is the bulk velocity of the plasma. Solving for the partial time derivative of the number density, I obtain

$$\frac{\partial n}{\partial t} = -\nabla \cdot (n\mathbf{u}). \tag{C.34}$$

Consider the term in Equation C.32 resulting from the change in the integrand n over the time interval Δt. (This term results from manipulation of Equation C.28.) It is given by

$$F_3 = \int_{\ell_1}^{\ell_2} d\ell \int\!\!\int_{A_c} \left(\frac{\Delta n}{\Delta t}\right) dA. \tag{C.35}$$

If I can replace the full time derivative $\frac{dn}{dt}$ with the partial time derivative $\frac{\partial n}{\partial t}$, then I can use Equation C.34 to write

$$F_3 = -\int_{\ell_1}^{\ell_2} \int\!\!\int_{A_c} \left[\nabla \cdot (n\mathbf{u})\right] dA\, d\ell. \tag{C.36}$$

Since

$$d^3x = dA\, d\ell \tag{C.37}$$

is a volume element within the magnetic flux tube, I can write

$$F_3 = -\int_{V_{ft}} \left[\nabla \cdot (n\mathbf{u})\right] d^3x, \tag{C.38}$$

where V_{ft} indicates that the integral is to be evaluated throughout the entire volume of the flux tube. Invoking Gauss's theorem, I can write

$$F_3 = -\int\int_{A_e} n\mathbf{u}\cdot d\mathbf{A}. \tag{C.39}$$

Here A_e is the surface enclosing the entirety of the flux tube. It is defined as the union of the cylindrical open surface OFT of the flux tube with the end areas A_{ℓ_1} and A_{ℓ_2}. With these definitions, I can write

$$\int\int_{A_e} n\mathbf{u}\cdot d\mathbf{A} = \int\int_{A_{\ell_1}} n\mathbf{u}\cdot d\mathbf{A} + \int\int_{A_{\ell_2}} n\mathbf{u}\cdot d\mathbf{A} + \int\int_{OFT} n\mathbf{u}\cdot d\mathbf{A}. \tag{C.40}$$

Substituting Equation C.40 into Equation C.39, substituting the resulting expression into Equation C.32, and re-arranging terms, I obtain

$$\begin{aligned} \frac{dN}{dt} = \int\int_{A_{\ell_1}} & n\left(\mathbf{v}_1 - \mathbf{u}\right)\cdot d\mathbf{A} + \int\int_{A_{\ell_2}} n\left(\mathbf{v}_2 - \mathbf{u}\right)\cdot d\mathbf{A} \\ & + \int_{\ell_1}^{\ell_2} d\ell \oint_C n v_n dC \\ & - \int\int_{OFT} n\mathbf{u}\cdot d\mathbf{A}. \end{aligned} \tag{C.41}$$

Noting that v_n, the component of flux tube velocity normal to the flux tube surface, is given generally by

$$v_n = \mathbf{v}\cdot\mathbf{e}_n, \tag{C.42}$$

I write the third term in the above expression for $\frac{dN}{dt}$ as

$$\int_{\ell_1}^{\ell_2} d\ell \oint_C n v_{fn} dC = \int\int_{OFT} n\mathbf{v}\cdot d\mathbf{A}. \tag{C.43}$$

Accordingly, I can write

$$\begin{aligned} \frac{dN}{dt} = \int\int_{A_{\ell_1}} & n\left(\mathbf{v}_1 - \mathbf{u}\right)\cdot d\mathbf{A} + \int\int_{A_{\ell_2}} n\left(\mathbf{v}_2 - \mathbf{u}\right)\cdot d\mathbf{A} \\ & + \int\int_{OFT} n\left(\mathbf{v} - \mathbf{u}\right)\cdot d\mathbf{A}. \end{aligned} \tag{C.44}$$

If the ionospheric ends of the flux tube are fixed, then

$$\mathbf{v}_1 = 0 \tag{C.45}$$

$$\mathbf{v}_2 = 0. \tag{C.46}$$

The expression for the time rate of change of the particle number then reduces to

$$\frac{dN}{dt} = -\int\!\!\int_{A_{\ell_1}} n\mathbf{u} \cdot d\mathbf{A} - \int\!\!\int_{A_{\ell_2}} n\mathbf{u} \cdot d\mathbf{A} + \int\!\!\int_{OFT} n\,(\mathbf{v} - \mathbf{u}) \cdot d\mathbf{A}. \tag{C.47}$$

Since the magnetic field is frozen into the plasma, I must have

$$\mathbf{v}|_{OFT} = \mathbf{u}|_{OFT}\,. \tag{C.48}$$

Accordingly, the third term in the expression above must vanish:

$$\int\!\!\int_{OFT} n\,(\mathbf{v} - \mathbf{u}) \cdot d\mathbf{A} = 0. \tag{C.49}$$

I am left with the following expression for the time rate of change of the particle number on a flux tube:

$$\frac{dN}{dt} = -\int\!\!\int_{A_{\ell_1}} n\mathbf{u} \cdot d\mathbf{A} - \int\!\!\int_{A_{\ell_2}} n\mathbf{u} \cdot d\mathbf{A}. \tag{C.50}$$

If the plasma velocity $\mathbf{u}$ has no component across the ends of the flux tube, then

$$\mathbf{u} \cdot d\mathbf{A}|_{A_{\ell_1}} = 0 \tag{C.51}$$

$$\mathbf{u} \cdot d\mathbf{A}|_{A_{\ell_2}} = 0, \tag{C.52}$$

and

$$\frac{dN}{dt} = 0. \tag{C.53}$$

That is, the number of particles on a magnetic flux tube is constant.

Appendix D

Derivation of the ionospheric energy flux

The energy flux out of the ionospheric end of a magnetic flux tube is given by the product of the instantaneous plasma energy density e and the instantaneous plasma speed u:

$$f = eu. \tag{D.1}$$

If the energy density e is identified as that corresponding to the internal energy of this system, then I can write

$$e = \left(\frac{3}{2}\right) P, \tag{D.2}$$

where P is identified as the thermal pressure as before. Accordingly,

$$f = \left(\frac{3}{2}\right) uP. \tag{D.3}$$

My challenge lies in determining an expression for the plasma speed u in terms of readily-available quantities.

Although the derivation in Appendix C applies to the particle number N, it is possible to recast much of its formulation in terms of any other quantity defined in a form like Equation C.1—that is, in terms of the integration of a density-like function along a magnetic flux tube.

In order to obtain the speed u, I begin by considering the integration of the locally-conserved quantity $P^{\frac{1}{\gamma}}$ (where $\gamma = \frac{5}{3}$ is the ratio of specific heats) over the volume of the flux tube. Substituting $P^{\frac{1}{\gamma}}$ for N in Equation C.1, I obtain the following definition for the quantity H:

$$H = \int_{\ell_1}^{\ell_2} d\ell \iint_{A_c} P^{\frac{1}{\gamma}}\, dA. \tag{D.4}$$

It will be shown shortly that H is related to the specific entropy S. The local conservation of $P^{\frac{1}{\gamma}}$ is expressed by the following equation:

$$\frac{\partial}{\partial t}\left(P^{\frac{1}{\gamma}}\right) + \nabla \cdot \left(P^{\frac{1}{\gamma}}\mathbf{u}\right) = 0. \tag{D.5}$$

As shown above (starting with Equation C.33 and continuing through Equation C.44), this property allows me to write

$$\begin{aligned} \frac{dH}{dt} = \int\int_{A_{\ell_1}} P^{\frac{1}{\gamma}} (\mathbf{v}_1 - \mathbf{u}) \cdot d\mathbf{A} + \int\int_{A_{\ell_2}} P^{\frac{1}{\gamma}} (\mathbf{v}_2 - \mathbf{u}) \cdot d\mathbf{A} \\ + \int\int_{OFT} P^{\frac{1}{\gamma}} (\mathbf{v} - \mathbf{u}) \cdot d\mathbf{A}. \end{aligned} \tag{D.6}$$

If I maintain that the frozen-in condition

$$\mathbf{v}_f \cdot d\mathbf{A}|_{OFT} = \mathbf{u} \cdot d\mathbf{A}|_{OFT} \tag{D.7}$$

holds along the outer surface OFT of the flux tube, then I obtain

$$\frac{dH}{dt} = \int\int_{A_{\ell_1}} P^{\frac{1}{\gamma}} (\mathbf{v}_1 - \mathbf{u}) \cdot d\mathbf{A} + \int\int_{A_{\ell_2}} P^{\frac{1}{\gamma}} (\mathbf{v}_2 - \mathbf{u}) \cdot d\mathbf{A}. \tag{D.8}$$

Assuming that the ends of the flux tube remain fixed (so that $\mathbf{v}_1 = \mathbf{v}_2 = 0$), I can write

$$\frac{dH}{dt} = -\int\int_{A_{\ell_1}} P^{\frac{1}{\gamma}} \mathbf{u} \cdot d\mathbf{A} - \int\int_{A_{\ell_2}} P^{\frac{1}{\gamma}} \mathbf{u} \cdot d\mathbf{A}. \tag{D.9}$$

I shall take the limit that the cross-sectional area of the magnetic flux tube becomes infinitesimal and invoke the conservation of magnetic flux ($dA \sim \frac{1}{B}$, in the manner of Equation B.6). Then the flux tube essentially corresponds to a single magnetic field line and I can write

$$\lim_{A_c \to 0} \int\int_{A_\ell} P^{\frac{1}{\gamma}} \mathbf{u} \cdot d\mathbf{A} \sim P^{\frac{1}{\gamma}} u_{\|}\Big|_{A_\ell} \Delta A_c|_{A_\ell} \,. \tag{D.10}$$

Here A_ℓ can apply to either A_{ℓ_1} or A_{ℓ_2}. Note that $u_{\|}$ is the component of the velocity that is parallel to the magnetic field at A_ℓ. (The end caps A_{ℓ_1} and A_{ℓ_2} are, on the other hand, perpendicular to the magnetic field.) Invoking conservation of magnetic flux to relate the area $\Delta A_c|_{A_\ell}$ at the ionospheric end of the flux tube to the magnetic field B_{isp} there, I write

$$\lim_{A_c \to 0} \int\int_{A_\ell} P^{\frac{1}{\gamma}} \mathbf{u} \cdot d\mathbf{A} \propto P^{\frac{1}{\gamma}} u_{\|}\Big|_{A_\ell} \left(\frac{1}{B_{isp}}\right). \tag{D.11}$$

Now I can write

$$\frac{dH}{dt} = -\,P^{\frac{1}{\gamma}}u_{\|}\left(\frac{1}{B_{isp}}\right)\Bigg|_{A_{\ell_1}} - P^{\frac{1}{\gamma}}u_{\|}\left(\frac{1}{B_{isp}}\right)\Bigg|_{A_{\ell_2}} . \qquad \text{(D.12)}$$

I shall also assume that the contributions from the two ends of the flux tube are equal to one another. Simplifying the notation by dropping the parallel subscript on u, I write

$$\frac{dH}{dt} = -2P^{\frac{1}{\gamma}}u\left(\frac{1}{B_{isp}}\right), \qquad \text{(D.13)}$$

where, again, B_{isp} is the magnitude of the magnetic field at one of the ionospheric footpoints. All other quantities on the right-hand side of the equation are also to be evaluated at one of the ionospheric footpoints of the magnetic flux tube.

Invoke the chain rule to write

$$\frac{dH}{dt} = \left(\frac{dx}{dt}\right)\left(\frac{dH}{dx}\right) = v_c\left(\frac{dH}{dx}\right), \qquad \text{(D.14)}$$

where x is the standard GSM coordinate of the flux tube intersection with the equatorial plane and

$$v_c = \frac{E}{B_{msp}} \qquad \text{(D.15)}$$

is the **E** × **B** drift velocity. (E is the magnitude of the convection electric field, and B_{msp} is the magnitude of the magnetic field at the aforementioned intersection of the magnetic flux tube with the equatorial plane.) Solving for u, I obtain

$$u = -\left(\frac{1}{2}\right)\left(\frac{E}{B_{msp}}\right)B_{isp}\left(\frac{1}{P^{\frac{1}{\gamma}}}\right)\left(\frac{dH}{dx}\right). \qquad \text{(D.16)}$$

Substituting this expression into Equation D.3, I obtain

$$f = -\left(\frac{3}{4}\right)\left(\frac{E}{B_{msp}}\right)B_{isp}P^{1-\frac{1}{\gamma}}\left(\frac{dH}{dx}\right). \qquad \text{(D.17)}$$

This expression is the result that I have been seeking: an expression for the ionospheric energy flux in terms of quantities that are readily available from the specific entropy model described in Section 2.3.

As mentioned earlier, the quantity H is simply related to the specific entropy S. Refer again to the definition of H in Equation D.4. As I did in writing Equations D.10 and

D.11, I take the limit as the cross-sectional area A_c becomes infinitesimal and the flux tube shrinks to a single magnetic field line. Since the pressure P is constant along a magnetic field line, the factor $P^{\frac{1}{\gamma}}$ can be taken outside the integrals. Taking all these considerations into account, I write

$$\lim_{A_c \to 0} \int_{\ell_1}^{\ell_2} d\ell \int\int_{A_c} P^{\frac{1}{\gamma}}\, dA \propto P^{\frac{1}{\gamma}} \int_{\ell_1}^{\ell_2} (\Delta A_c)\, d\ell. \tag{D.18}$$

As before, I invoke conservation of magnetic flux to reduce the area integral to a quantity proportional to $\frac{1}{B}$. (Again refer to Equation B.6 and the discussion immediately preceding it.) So the above limit becomes

$$\lim_{A_c \to 0} \int_{\ell_1}^{\ell_2} d\ell \int\int_{A_c} P^{\frac{1}{\gamma}}\, dA \propto P^{\frac{1}{\gamma}} \int_{\ell_1}^{\ell_2} \left(\frac{1}{B}\right) d\ell, \tag{D.19}$$

a result similar to Equation B.7. Accordingly, I can write

$$H = P^{\frac{1}{\gamma}} V, \tag{D.20}$$

where

$$V = \int_{\ell_1}^{\ell_2} \left(\frac{1}{B}\right) d\ell \tag{D.21}$$

is the usual definition of the magnetic flux tube volume per unit magnetic flux (as given by Equation B.8 of Appendix B). Referring to the global definition of the specific entropy given by Equation 1.11 in Chapter 1, I see that

$$H = S^{\frac{1}{\gamma}}. \tag{D.22}$$

So the quantity H (defined in Equation D.4) is indeed simply related to the specific entropy S, as stated earlier.

Appendix E

Estimate of the time required to deplete the "magnetic flux reservoir"

I can estimate the time that is required to deplete a "magnetic flux reservoir" of magnetic flux. Figure E.1 depicts the magnetic flux reservoir and the corresponding flow channel as seen from above the equatorial plane.

Let us consider the magnetic flux in the "magnetic flux reservoir."

$$\Phi_B = \int_S \mathbf{B} \cdot d\mathbf{A} \tag{E.1}$$

This integral is evaluated over the surface S. The unit normal of the surface is $\mathbf{e}_n$, and

$$d\mathbf{A} = \mathbf{e}_n \, dA. \tag{E.2}$$

Now consider the (full) time derivative of this magnetic flux.

$$\frac{d\Phi_B}{dt} = \frac{d}{dt} \int_S \mathbf{B} \cdot d\mathbf{A} \tag{E.3}$$

I will take the time derivative inside the integral sign.

$$\frac{d\Phi_B}{dt} = \int_S \frac{d\mathbf{B}}{dt} \cdot d\mathbf{A} + \Upsilon_2 \tag{E.4}$$

The term Υ_2 takes into account any variation in the surface S with time. I will assure that this surface does not vary in time, so that

$$\Upsilon_2 = 0, \tag{E.5}$$

and I can write

$$\frac{d\Phi_B}{dt} = \int_S \frac{d\mathbf{B}}{dt} \cdot d\mathbf{A}. \tag{E.6}$$

If I presume that I can replace the full time derivative of **B** with its partial time derivative (as would be appropriate since the surface S is stationary), then I can use Faraday's law

$$\nabla \times \mathbf{E} = -\frac{\partial \mathbf{B}}{\partial t} \tag{E.7}$$

to write

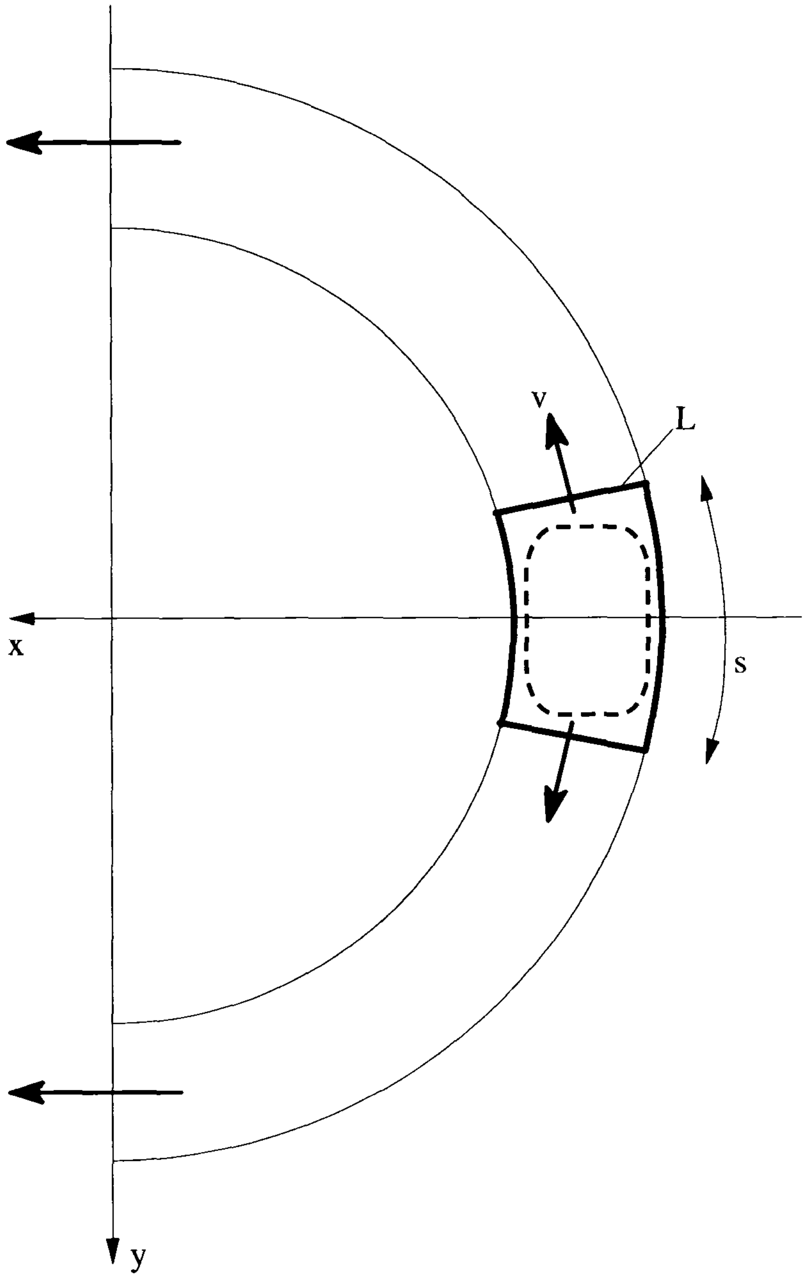

Figure E.1. Magnetic flux reservoir. A sketch of the magnetic flux reservoir, as seen from above the equatorial plane. The reservoir itself is the region within the dotted lines. The angular region (bounded by thick lines) surrounding the reservoir is the contour C discussed in this appendix. It has radial 'arms' of length L and (linear) azimuthal extent s. The (divergent) outflow velocity is denoted by v.

$$\frac{d\Phi_B}{dt} = -\int_S (\nabla \times \mathbf{E}) \cdot d\mathbf{A}. \tag{E.8}$$

Invoking Stokes' theorem, I write

$$\frac{d\Phi_B}{dt} = -\oint_C \mathbf{E} \cdot d\boldsymbol{\ell}. \tag{E.9}$$

I will use the frozen-in flux condition

$$\mathbf{E} + \mathbf{v} \times \mathbf{B} = 0 \tag{E.10}$$

$$\mathbf{E} = -\mathbf{v} \times \mathbf{B}. \tag{E.11}$$

Now I obtain

$$\frac{d\Phi_B}{dt} = \oint_C (\mathbf{v} \times \mathbf{B}) \cdot d\boldsymbol{\ell}. \tag{E.12}$$

The expression on the right-hand side of the equation is simply the cross-polar cap (electric) potential Φ_E:

$$\Phi_E = \oint_C (\mathbf{v} \times \mathbf{B}) \cdot d\boldsymbol{\ell}. \tag{E.13}$$

I can then write

$$\frac{d\Phi_B}{dt} = \Phi_E. \tag{E.14}$$

I will evaluate Equation E.13 around the contour C enclosing the flux reservoir. The contributions along the arms of length L are non-zero. I can argue that the contributions along the other two legs can be neglected, in part because $\mathbf{v} \times \mathbf{B}$ will be largely perpendicular to $d\boldsymbol{\ell}$. (This point can certainly be argued.) With this arguments, I can write

$$\Phi_E = -2v_0 B_0 L, \tag{E.15}$$

where v_0 is the characteristic speed of the plasma outflow, B_0 is the characteristic strength of the magnetic field in the flux reservoir region, and L is the width of the outflow region.

The negative sign in the expression above arises sinces $\mathbf{v} \times \mathbf{B}$ is pointed in the direction opposite to $d\boldsymbol{\ell}$, where the direction of $d\boldsymbol{\ell}$ is consistent with the normal $\mathbf{e}_n$ of the surface $\mathbf{S}$ and $\mathbf{e}_n$ is aligned in the direction of $\mathbf{B}$ in the equatorial plane.

Solving for v_0, I obtain

$$v_0 = \frac{|\Phi_E|}{2B_0L}. \tag{E.16}$$

If I use the value $L = 4\ R_E$ and a characteristic value of the cross polar cap potential of 50 kV, then I obtain $v_0 \simeq 19.6\ km/s$.

Combining Equation E.14 with Equation E.15, I obtain

$$\frac{d\Phi_B}{dt} = -2v_0B_0L. \tag{E.17}$$

Integrating this expression over the time interval Δt, I obtain

$$\Delta\Phi_B = -2v_0B_0Lv_0\,\Delta t \tag{E.18}$$

The magnetic flux originally in the 'flux reservoir' can be estimated to be

$$\Phi_0 \simeq B_0Ls, \tag{E.19}$$

where s is a characteristic azimuthal extent of the 'flux reservoir.'

The magnetic flux in the reservoir after the elapse of the time Δt is given by

$$\Phi_1 = \Phi_0 + \Delta\Phi_B \tag{E.20}$$

$$\Phi_1 = B_0Ls - 2B_0Lv_0\,\Delta t \tag{E.21}$$

$$\Phi_1 = B_0L\,(s - 2v_0\,\Delta t)\,. \tag{E.22}$$

The corresponding characteristic magnetic field (in the flux reservoir after the time Δt has elapsed) is given by

$$B_1 \simeq \frac{\Phi_1}{Ls} \tag{E.23}$$

$$B_1 \simeq B_0 \left(1 - \frac{2v_0\,\Delta t}{s}\right). \tag{E.24}$$

The flux reservoir will be depleted when $B_1 = 0$. That happens once

$$1 - \frac{2v_0\,\Delta t}{s} = 0. \tag{E.25}$$

Solving for Δt, I find

$$\Delta t = \frac{s}{2v_0}. \tag{E.26}$$

Again, s corresponds to the azimuthal extent of the reservoir. It is comparable to the radial distance to the reservoir. Using the value $s \simeq 10\ R_E$ and the earlier value of v_0, I obtain

$$\Delta t = 1627\ s \simeq 27\ min. \tag{E.27}$$

Since times in the simulation are normalized to the Alfvén time $t_A = 14.6\ s$, I find that

$$\Delta t \simeq 111\ t_A. \tag{E.28}$$

Bibliography

Baker, D. N., and T. I. Pulkkinen (1991), The Earthward edge of the plasma sheet in magnetospheric substorms, in *Magnetospheric Substorms*, edited by J. R. Kan, T. A. Potemra, S. Kokubun, and T. Iijima, pp. 147–160, AGU, Washington, D. C.

Baumjohann, W. B., and R. A. Treumann (1997), *Basic Space Plasma Physics*, Imperial College Press, London.

Beard, D. B. (1979), The magnetotail magnetic field, *J. Geophys. Res.*, *84*, 495.

Chodura, R., and A. Schlüter (1981), A 3-D code for MHD equilibrium and stability, *J. Comput. Phys.*, *41*, 68.

Crooker, N. U., R. A. Greenwald, M. Hesse, M. K. Hudson, W. J. Hughes, L. R. Lyons, N. C. Maynard, C. T. Russell, and G. L. Siscoe (1999), Report from the First Geospace Environment Modeling (GEM) Campaigns: 1991–1997, *Tech. rep.*, Space Science Center, IGPS, UCLA.

Erickson, G. M. (1984), On the cause of X-line formation in the near-earth plasma sheet: Results of adiabatic convection in the plasma-sheet plasma, in *Magnetic Reconnection, Geophys. Monogr. Ser., Vol. 30*, edited by E. W. Hones, pp. 296–302, AGU, Washington, D. C.

Erickson, G. M., and R. A. Wolf (1980), Is steady convection possible in the Earth's magnetotail?, *Geophys. Res. Lett.*, *7*, 897–900.

Fletcher, C. A. J. (1991), *Computational Techniques for Fluid Dynamics*, Springer-Verlag, Berlin.

Harris, E. G. (1965), On a plasma sheet separating regions of oppositely directed magnetic field, *Nuovo Cimento*, *23*, 115.

Hesse, M., and J. Birn (1993), Three-dimensional magnetotail equilibria by numerical relaxation techniques, *J. Geophys. Res.*, *98*, 3973–3982.

Kivelson, M. G., and C. T. Russell (1995), *Introduction to Space Physics*, Cambridge University Press.

Lanchester, B. S., M. H. Rees, D. Lummerzheim, A. Otto, and H. U. Frey (1997), Large fluxes of auroral electrons in filaments of 100 m width, *J. Geophys. Res.*, *102*, 9741.

Lee, L. C., L. Zhang, G. S. Choe, and H. J. Cai (1995), Formation of a very thin current sheeet in the near-earth magnetotail and the explosive growth phase of substorms, *Geophys. Res. Lett.*, *22*, 1137.

Lee, L. C., L. Zhang, A. Otto, G. S. Choe, and H. J. Cai (1998), Entropy antidiffusion instability and formation of a thin current sheet during geomagnetic substorms, *J. Geophys. Res.*, *103*, 29,419.

Lemon, C., F. Toffoletto, M. Hesse, and J. Birn (2003), Computing magnetospheric force equilibria, *J. Geophys. Res.*, *108*, SMP 10–1.

Lummerzheim, D., M. Brittnacher, D. Evans, G. A. Germany, G. K. Parks, M. H. Rees, and J. F. Spann (1997), High time resolution study of the hemispheric power carried by energetic electrons into the ionosphere during the May 19/20, 1996 auroral activity, *Geophys. Res. Lett.*, *24*, 987.

Lyon, J., S. H. Brecht, J. D. Huba, J. A. Fedder, and P. J. Palmadesso (1981), Computer simulation of a geomagnetic substorm, *Phys. Rev. Lett.*, *46*, 1038.

Marion, J. B., and W. F. Hornyak (1982), *Physics for Science and Engineering, Parts 1 & 2 Combined,* Saunders College Publishing, Philadelphia.

McComas, D. J., C. T. Russell, R. C. Elphic, and S. J. Bame (1986), The near-earth cross-tail current sheet: Detailed ISEE 1 and 2 case studies, *J. Geophys. Res.*, *91*, 4287.

McPherron, R. L. (1972), Substorm related changes in the geomagnetic tail: The growth phase, *Planet. Space Sci.*, *20*, 1521.

McPherron, R. L., A. Nishida, and C. T. Russell (1987), Is near-Earth current sheet thinning the cause of auroral substorm onset?, in *Quantitative Modeling of the Magnetosphere-Ionosphere Coupling Processes*, edited by Y. Kamide and R. A. Wolf, p. 252, Kyoto Sangyo Univ., Kyoto, Japan.

Mead, G. D., and D. H. Fairfield (1975), A quantitative magnetospheric model derived from spacecraft magnetometer data, *J. Geophys. Res.*, *80*, 523.

Nakamura, R., et al. (2002), Fast flow during current sheet thinning, *Geophys. Res. Lett.*, *29*, 2140.

Ness, N. F. (1965), The earth's magnetic tail, *J. Geophys. Res.*, *70*, 2989.

Ogino, T., R. J. Walker, M. Ashour-Abdalla, and J. M. Dawson (1986), An MHD simulation of the effects of the interplanetary magnetic field B_y component on the interaction of the solar wind with the Earth's magnetosphere during southward interplanetary field, *J. Geophys. Res.*, *91*, 10,029.

Olson, W. P., and K. Pfitzer (1974), A quantitative model of the magnetospheric magnetic field, *J. Geophys. Res.*, *79*, 3739.

Otto, A. (1990), 3D resistive MHD computations of magnetospheric physics, *Comput. Phys. Commun.*, *59*, 185.

Potter, D. (1973), *Computational Physics*, John Wiley & Sons, New York.

Pulkkinen, T. I., and M. Wiltberger (2000), Thin current sheet evolution as seen in observations, empirical models and MHD simulations, *Geophys. Res. Lett.*, *27*, 1363.

Pulkkinen, T. I., D. N. Baker, D. G. Mitchell, R. L. McPherron, C. Y. Huang, and L. A. Frank (1992), Global and local current sheet thickness estimates during the late growth phase, in *Proceedings of the International Conference on Substorms*, pp. 131–135.

Pulkkinen, T. I., D. N. Baker, D. G. Michell, R. L. McPherron, C. Y. Huang, and L. A. Frank (1994a), Thin current sheets in the magnetotail during substorms: CDAW 6 revisited, *J. Geophys. Res.*, *99*, 1994.

Pulkkinen, T. I., D. N. Baker, P. K. Toivanen, R. J. Pellinen, R. H. W. Friedel, and A. Korth (1994b), Magnetospheric field and current distributions during the substorm recovery phase, *J. Geophys. Res.*, *99*, 10,955.

Pulkkinen, T. I., et al. (1991), Modeling the growth phase of a substorm using the Tsyganenko model and multi-spacecraft observations: CDAW-9, *Geophys. Res. Lett.*, *18*, 1963.

Runov, A., R. Nakamura, W. Baumjohann, T. L. Zhang, M. Volwerk, H.-U. Eichelberger, and A. Balogh (2003), Cluster observation of a bifurcated current sheet, *Geophys. Res. Lett.*, *30(2)*, 1036.

Sanny, J., R. L. McPherron, C. T. Russell, D. N. Baker, T. I. Pulkkinen, and A. Nishida (1994), Growth-phase thinning of the near-Earth current sheet during the CDAW 6 substorm, *J. Geophys. Res.*, *99*, 5805.

Schindler, K., and J. Birn (1982), Self-consistent theory of time-dependent convection in the earth's magnetotail, *J. Geophys. Res.*, *87*, 2263.

Schindler, K., and J. Birn (1993), On the cause of thin current sheets in the near-Earth magnetotail and their possible significance for magnetospheric substorms, *J. Geophys. Res.*, *98*, 15,477.

Sergeev, V., et al. (2003), Current sheet flapping motion and structure observed by Cluster, *Geophys. Res. Lett.*, *30*, 60–1.

Sergeev, V. A., P. Tanskanen, K. Mursula, A. Korth, and R. C. Elphic (1988), Current sheet thickness in the near-Earth plasma sheet during substorm growth phase as inferred from simultaneous magnetotail and ground-based observations, *Adv. Space Res.*, *8*, 125.

Sergeev, V. A., P. Tanskanen, A. Korth, and R. C. Elphic (1990), Current sheet thickness in the near-Earth plasma sheet during substorm growth phase, *J. Geophys. Res.*, *95*, 3819.

Sergeev, V. A., D. G. Mitchell, C. T. Russell, and D. J. Williams (1993), Structure of the tail plasma/current sheet at $\approx 11R_e$ and its changes in the course of a substorm, *J. Geophys. Res.*, *98*, 17,345.

Thompson, S. M., M. G. Kivelson, K. K. Khurana, R. L. McPherron, J. M. Weygand, A. Balogh, H. Réme, and L. M. Kistler (2005), Dynamic Harris current sheet thickness from Cluster current density and plasma measurements, *J. Geophys. Res.*, *110*, A02,212, doi:10.1029/2004JA01,714.

Tsyganenko, N. A. (1989), A magnetospheric magnetic field model with a warped tail current sheet, *Planet. Space Sci.*, *37*, 5–20.

Tsyganenko, N. A. (1996), Effects of the solar wind conditions on the global magnetospheric configuration as deduced from data-based models, in *Proc.of 3rd International Conference on Substorms (ICS-3)*, pp. 181–185, ESA-SP-389, Versailles, France.

Voigt, G.-H. (1981), A mathematical magnetospheric field model with independent physical parameters, *Planet. Space Sci.*, *29*, 1–20.

Voigt, G.-H. (1996), Magnetospheric equilibrium configurations and slow adiabatic convection, in *Solar Wind-Magnetosphere Coupling*, edited by Y. Kamide and J. A. Slavin, pp. 233–273, Terra Scientific, Tokyo.

Voigt, G.-H., and R. A. Wolf (1988), Quasi-static magnetospheric MHD processes and the "ground state" of the magnetosphere, *Rev. Geophys.*, *26*, 823–843.

Wu, C. C. (1983), Shape of the magnetopause, *Geophys. Res. Lett.*, *10*, 545.

Zhou, X.-Y., C. T. Russell, J. T. Gosling, and D. G. Mitchell (1997), Three spacecraft observations of the geomagnetic tail during moderately disturbed conditions: Structure and evolution of the current sheet, *J. Geophys. Res.*, *102*, 14,415.